UNIVERSITY OF NAPLES FEDERICO II

PHD PROGRAM

IN

EARTH, ENVIRONMENTAL AND RESOURCES SCIENCES

XXXVI CYCLE

URBAN GEOLOGY AND GEOHAZARDS:

AN INTEGRATED ANALYSIS

FOR A RESILIENT URBAN PLANNING

ADVISOR:

PROF. DOMENICO CALCATERRA

CO-ADVISOR:

PROF. DIEGO DI MARTIRE

PHD CANDIDATE:

GIUSEPPE BAUSILIO

PHD COORDINATOR:

PROF. ROSA DI MAIO

ACADEMIC YEAR: 2022/2023

LIST OF FIGURES

LIST OF TABLES

LIST OF ACRONYMS

AUC – Area Under the Curve

CARG – CARtografia Geologica (Geological CARtography)

EM – Ensemble Modeling

ER – Elements at Risk

HETD – Hydraulic Erosion, Transport and Deposition

IFFI – Inventario dei Fenomeni Franosi in Italia (Italian Landslide Inventory)

ISTAT – Istituto nazionale di STATistica (National STATistic Institute)

LaICa – Landslide Inventory of the Campania region

MaxEnt – Maximum Entropy

ML – Machine Learning

MR – Multi Risk

PAb – Pseudo Absence

RES – Rock Engineering System

RF – Random Forest

ROC – Receiver Operating Characteristic

UNESCO – United Nations Educational, Scientific and Cultural Organization

VIF – Variance Inflation Factor

CONTENTS

ABSTRACT

This PhD project's objectives were the characterization and modelling of different geohazards, their effect on the urban fabric, and the study of the impact that a single geohazard can exert on other geohazards through a multirisk approach.

The entire process was divided into three phases. During the first one, the preprocessing phase, the Geohazards (sinkhole, landslide and flood) inventories, Predisposing factors and Elements at Risk map were prepared. In particular, sinkhole and landslide inventories for the city of Naples underwent an updating phase starting from pre-existing data. The sinkhole inventory update was performed starting from the Guarino and Nisio (2012) published inventory and using national and local news, city council reports, and field work. The landslide inventory used in this project was extracted from the Landslide Inventory of the Campania region (hereafter LaICa), published by Fusco et al. in 2023. LaICa was obtained by gathering and uniforming the inventories of the former Campania Units of Management, the IFFI project, and literature data. The research group of the Department of Earth, Environmental and Resources Science of the University of Naples Federico II contributed and provided support during the update phase. As for the flood inventory, a sampling operation was carried out, extracting random points from the flood hazard polygons of the former Unit of Management "*Campania Centrale*". This process was necessary due to the lack of an available flood inventory for the city of Naples. The last step in the preprocessing phase was the production of the Damage map used for the Risk Assessment. The first element of Damage, Elements at Risk, was evaluated using the following layers as base data:

- Population density (spatially distributed according to the Census Sections and divided into five classes from Very Low to Very High);
- Rail transport (considered as a strategic infrastructure);

- Road system (divided into non-strategic and strategic networks, the latter mainly consisting of motorways and main arteries);
- Natural Reserves (*Parco Regionale dei Campi Flegrei* and *Parco Regionale Metropolitano delle Colline di Napoli*);
- Buildings divided into strategic structures (hospitals, barracks, schools, railway stations, administrative and government buildings, etc.) and non-strategic ones.

Due to the difficulty in defining the Vulnerability for such a heterogeneous and complex territory as the City of Naples, a precautionary measure has been adopted by attributing the maximum Vulnerability value (1) to the entire area.

The objective of the second phase of the approach was the production of the Landslide, Sinkhole, and Flood Risk maps, combining Damage and Relative Hazard using Risk Matrix. The Relative Hazard assessment was carried out using an Ensemble Modeling approach, deploying two Machine Learning methods, the Maximum Entropy (MaxEnt) and the Random Forest (RF) algorithms. Two approaches were used to increase the performance obtained from the geohazard susceptibility assessment:

- the K-Fold Crossvalidation approach was used on the presence data, allowing the iteration of the modelization process and obtaining a mean value of the performance score;
- The Variance Inflation Factor (VIF) was deployed to detect any collinearity problems between the predisposing factors.

The Susceptibility map obtained using the Ensemble Modeling approach reached excellent ROC/AUC performance scores (Flood & Hydraulic Erosion, Transport and Deposition susceptibility 0.94; Landslide susceptibility 0.94; Sinkhole susceptibility 0.89). These performance were evaluated using, as test data, 30% of the original inventories that have

been kept outside of the susceptibility assessment process, which was carried out on the remaining 70% of the original data. Due to the incomplete temporal information in two of the three inventories used, it was not possible to perform a return period analysis. For this reason, the Susceptibility (Relative Hazard) was used to evaluate the Risk. Damage and Relative Hazard were combined, using a Risk matrix, to obtain the Risk maps.

During the third and last step, the mutual influence between geohazards was evaluated through a multi-hazard approach using the Rock Engineering Systems (Hudson, 1992) method. The Interaction Matrix was compiled using the Relative Hazard maps obtained in the previous phase as parameters of the Multirisk system. Through the Matrix, two scores are attributed by the user to every single parameter (the geohazard): (i) a cause score, which is the impact of the parameter over the other parameters and (ii) the effect score, the impact of the other geohazards against the parameter in analysis. The score ranges from 0 (no influence) to 3 (maximum influence). In the following step, all the sums of cause and effect scores for every parameter are evaluated (C+E). The percentage value of C+E for a geohazard against the total sum of the C+E of all the parameters is the interactivity [%]. Three interactivity maps were produced, one for every geohazard, by attributing the interactivity percentage value to the areas where the geohazard was present. The final Multirisk map was obtained by combining the Interactivity Map and the Damage Map using a risk matrix. From the analysis of the final products, the weight of the flood geohazard on the other parameters is evident. Out of the three parameters, the flood-related one is the only dominant one (Causes score > Effects score), while the remaining two are subordinate parameters (Causes score < Effects score). The historic city centre falls within the Medium Multirisk class area despite the lower local interactivity when compared to other places. This is due to the influence of the Damage map, as a high density of strategic structures and infrastructures is located within the city centre. The Natural Reserves' influence is also evident along the western and northern slopes, where the High and Very High

Multirisk classes are abundant. As for the eastern sector of the city, the strategic infrastructures (main roads, highways and railways) are heavily influential, as the High and Very High classes are located along these elements. The results obtained are adequate to expectations and, in the future, the integration of further geohazards which have a recognized influence on other parameters (fires-landslides, for example) would allow a more detailed definition of the Multirisk system in an urban context.

1. INTRODUCTION

Cities and mega-cities are the greatest and ever-growing trace of human presence on Earth, often depicted as the "*leftovers*" of humanity after extinction and becoming a trope in literature and movies. A classic example of this trope is the Statue of Liberty in the Planets of the Apes movie (Schaffner, 1968) representing the last trace of New York City. Cities are, as defined by Scott and Storper (2015), "*dense agglomerations of people and economic activities*". The aforementioned authors also identify the food surplus as the historical reason behind city development in ancient times. Some recent events have negatively influenced city growth all over the world (Aassve et al., 2021), but this seems like a common phenomenon in human history, especially during pandemic events like the Black Plague, the Spanish Flue or the more recent pandemic caused by the SARS-CoV-2 virus (Florida et al., 2021). However, cities are still expected to either grow or renovate their infrastructure (Genske and Ruff, 2006) which can cause concerns about the safety of the newly built and renovated areas. This urban growth requires close cooperation between urban planning and geology (Hofmann, 1976; McCall, 1998; Rimal et al., 2018). The aforementioned concerns regarding the safety of the social and urban fabric are related to geohazards. In geology, geohazards are natural sources of damage to people and the socioeconomic fabric due to geological processes and features (Lacasse et al., 2009). Earthquakes, volcanic eruptions, landslides, and floods are only a few (Rosenbaum and Culshaw, 2003) of the most recurrent geohazards that come to mind.

The city of Naples is an example of an urban area impacted by geohazards. The city is located in South Italy and it is one of the largest Italian cities with 2.969.571 inhabitants (total amount for the entire metropolitan city, ISTAT, January 2023, https://demo.istat.it/). It is also the most important city centre in South Italy due to its history and culture (Mazzeo, 2009). The integration in its municipality of the near settlements during the twenties of the last century and the economic boom of the sixties allowed the city to grow and expand its urban fabric. Starting

from the first years of the third millennium, the city population has started to decline (https://demo.istat.it/) and the urban planning kept renovating the infrastructure of the city. The western sector of the city is part of the active Phlegrean volcanic field while the eastern sector is part of the southern Campanian plain and borders the Somma-Vesuvius volcanic complex. Eruptive products from the two active volcanoes characterize the geology of the city (Scarpati et al., 2015). These volcanic materials are involved in landslides. Due to the abovementioned high urbanization, landslides have been a constant risk for the city (Di Martire et al., 2012) and the landslide inventory contains over 1500 entries inside the municipality of Naples (Fusco et al., 2023) since the mid 19th century. Rock falls and topples in tuffs characterize the city cliffs and quarries, while slides and flows affect mainly the shallower pyroclastic layers that cover the main hills of the city (Parise et al., 2004; Calcaterra et al., 2007). One of the oldest documented cases is related to the 1868 rock fall in the city center, at the foot of Mt. Echia. The landslide caused the death of tens of people and huge economic loss (Calcaterra and de Luca Tupputi Schinosa, 2006). The aforementioned tuffs, mainly Neapolitan Yellow Tuff and Campanian Ignimbrite (Scarpati et al., 2015), were excavated to use as a building material since ancient times (Colella et al., 2017) and are largely used in the city as both building and decorative material (Calcaterra et al., 2000; Morra et al., 2010). In some cases, the building materials were excavated from underground cavities located close to or right under the construction site. These cavities, having exhausted their utility, were closed or converted for hydraulic usage or as worship places (Scotto di Santolo et al., 2015; 2022; Langella et al., 2022). The presence of this cavity network, combined with other factors like pipeline leaks, makes Naples extremely susceptible to sinkholes (Guarino and Nisio, 2012; Rispoli et al., 2020), as evidenced by the more than 450 entries of the published Sinkhole inventory (Tufano et al., 2022). These sinkholes are a threat to both population and cultural heritage of the city (Rispoli et al., 2020). In January 1996, in the neighbourhood of *Secondigliano*, northern Naples, a cave

collapse in an underground working site triggered a sinkhole that subsequently severed a gas pipeline, causing an explosion that killed 11 persons (Evangelista and Viggiani, 2013). The same year, in December, another cavity collapse triggered a sinkhole that killed a father and his son (Faenza, 1996) while they were resting in their smithy. These abovementioned landslide and sinkhole events showcase why risk and susceptibility assessment are a necessity in a world with an increasing population and growing cities.

By definition, susceptibility is an assessment of the spatial distribution and classification of a hazard that can potentially trigger in a specific area (Fell et al., 2008). Depending on how much the geohazard and the area are known, this assessment can be qualitative or quantitative and can include other information like the magnitude of the event or its velocity. By definition (Fell et al., 2008) time, considered as the return period of a triggered event, is not considered in susceptibility assessment. This return period is, in other words, the average time that passes between an event and the following one (Salvadori et al., 2011). Many studies analyzed the return period of landslides and its relationship with rainfalls (e.g. Iida, 2004; Sepe et al., 2023). This information is extremely important in the definition of risk, which is defined as the probability of loss (of human lives or property) taking into account elements at risk, degree of loss and temporal-spatial probability of the event (Fell et al., 2008). As this thesis focuses on the development of a method replicable in other urban areas, a semi-quantitative risk analysis (Andrejev et al., 2017) will be performed using the inventories as presence data for the machine learning algorithms.

Machine Learning (hereafter ML) algorithms are "*logical or binary operations, that learn a task from a series of examples*" (Michie et al., 1994). In other words, ML algorithms are nothing more than codes that, to reach their objective (classification or regression), need to evaluate the relationship between the input data provided by the operator by itself. This is, of course, not a random process. ML algorithms utilize the training input data to weigh the

importance of the environmental factors and produce a model. Subsequently, this model is validated using the testing data. ML has been used in different disciplines, from medicine (Kononenko, 2001; Rajula et al., 2020), to ecology (Recknagel, 2001; Ramesh et al., 2018), to finance (Krollner et al., 2010; Beutel et al., 2019). In geology, ML algorithms have been used (Dramsch, 2020) in different fields like geo-resources prospecting (Newendorp, 1976; Reddy and Bonham-Carter, 1991; Shirmard et al., 2022) or susceptibility assessment of geohazards like landslides (Yao et al., 2008; Di Napoli et al., 2020), groundwater flooding (Allocca et al., 2021; Coda et al., 2023), sinkholes (Gao and Alexander, 2008; Bausilio et al., 2022; Bianchini et al., 2022) and flooding (Janizadeh et al., 2019; Prasad et al., 2022). The susceptibility maps obtained with the ML algorithms will be used to perform an Ensemble Modeling (hereafter EM) approach. During an EM susceptibility assessment, different algorithms and training data sets are used to produce multiple different susceptibility maps. The latters are then combined using different strategies to obtain a final susceptibility map (Kotu and Deshpande, 2015). In literature this approach has been proven to be effective showing better accuracy (Kadavi et al., 2018; Di Napoli et al., 2020). In this PhD project both susceptibility assessments and the EM will be performed using the biomod2 package (Thuiller et al., 2024) in R (R Core Team, 2023) and R Studio (Posit Team, 2024).

In this thesis, susceptibility maps for different geohazards (landslide, sinkhole, and flooding) will be produced. Using a semi-quantitative (Andrejev et al., 2017) approach, we will assess the relative risk for the city of Naples using population data from the Census Sections. Modelling the geohazard risk will partly accomplish the objective of this thesis. Geohazards can sometimes influence each other, affecting the same space at the same time, and generating a domino effect. The term "*cascade*" is used for these interactions (Helbing et al., 2006; Pescaroli and Alexander, 2015). To evaluate this domino effect with a multirisk approach, the Rock Engineering System (RES) from Hudson (1992) will be applied and adjusted for this

thesis. This method requires the production of an interaction matrix to classify and provide a score for all the parameters involved, quantifying the mutual influence. This method has been used in landslide susceptibility assessment (Mazzoccola, 1992) but, in this study, it will be used to evaluate the mutual influence of the environmental parameters and the geohazards to evaluate the multirisk in the urban area of the city of Naples.

1.1. Structure of the thesis

This thesis is structured in seven sections. The first section provides an introduction to the objective of the study, the geohazards, the study area and the state-of-the-art regarding susceptibility and risk assessment. In the second section, an in-depth explanation of the geohazards analyzed through the multirisk approach used in this thesis is granted. Whenever available, a description of the geohazard inventory, the classification used, the main features and main causes are also provided. Afterwards, in the third section, a description concerning risk assessment is granted, considering both the state-of-the-art and the methodology used for this study. The fourth section describes the study area, providing a historical, geographical and geological context regarding the city of Naples. In the fifth section, the results obtained from the methodology shown in this thesis are applied to the study area. A description of the methodology used will be provided in this section before describing the Susceptibility, Risk and Multirisk Maps. The maps themselves will be provided to the reader with data about the performance of the applied method. In the sixth chapter, the results will be discussed, showcasing pros and cons of the methodology used to obtain the Multirisk map for the city of Naples and, in the seventh and last section of this thesis, conclusions will be drawn and future developments of this research will be discussed.

1.2. Objectives

The aim of this study is the characterization of the different geohazards that can affect urban areas of modern cities. This characterization will be performed through different steps:

- Production of an inventory to be used as presence data for model training and testing for those geohazards that lack statistic data;
- Assessment of every geohazard susceptibility for the study area using ML methods;
- Production of risk maps using official data available for the entire Italian territory (Census Sections – *Sezioni Censuarie*). Using such data allows replicability of the method in other urban areas;
- Production of a Multirisk map through the modelization of the interaction between geohazards and their impact on the urban fabric.

The last step is extremely important, the creation of a tool that can be used by public administrations and stakeholders to mitigate risk and to help reach resilient urban planning.

2. GEOHAZARD

Risks are strictly related to human life. There is technically no risk if there is absence of humans and their socioeconomic fabric (McCall, 2012). When hazard is "*characterized by geological, hydrogeological or geomorphological nature*" (Doornkamp, 1989) the term geohazard is used. McCall separates geohazards in intensive (rapid-onset) and pervasive (slow-onset) ones (McCall, 1998). Earthquakes, eruptions, slope movements, rapid subsidence, flooding, wildfires and meteorological hazards such as cyclones and tornados are intensive geohazards. Pervasive geohazards include relatively slower phenomena like depletion and pollution of groundwater resources, rising sea level, soil loss and geomorphologic changes due to urban development, slow subsidence, compressibility of soils and many others (McCall, 1998). In the following paragraphs, a brief description of the main geohazards that will be considered in this work is presented.

2.1. Landslides

Landslides contribute significantly to multiple-hazard disasters (Schuster, 1996) although, sometimes, their impact can be undervalued against other geohazards, like earthquakes (Turner and Schuster, 1996; Schuster and Highland, 2001). Landslides are widespread all over the world and often lead to loss of human life (Aleotti and Chowdhury, 1999; Guzzetti, 2000; Petley, 2012; Pollock and Wartman, 2020). Various factors concur to slope instability and are divided into two fundamental categories: predisposing factors and triggering factors (Crozier, 1986; Wieczorek, 1996). All these factors contribute to slope instability by either increasing the shear stress or decreasing the shear strength (Terzaghi, 1950). When the ratio between acting forces and resisting forces becomes greater than one (acting forces > resisting forces) slope instability and the formation of a surface of rupture can occur.

Of the various predisposing factors, we can remember slope angle (Dai et al., 2002; Guzzetti et al., 2006), lithology (Pachauri and Pant, 1992; Guzzetti et al., 1996), aspect (Lee, 2005; Galli et al., 2008), land use and type of vegetation (Glade, 2003; Reichenbach et al., 2014), distance from the hydrological network (Liu et al., 2004; Meten et al., 2015) and distance from slope cuts represented by paths and trails (Sidle et al., 2006; McAdoo et al., 2018). As for the triggering factors, there are countless examples in the literature of landslides caused by prolonged rainfall, earthquakes or human activities (Glade, 1998; Iverson, 2000; Corominas et al., 2014).

There have been, during the years, different definitions of landslide and most of them highlighted the gravity-driven nature of the phenomenon and the materials involved (natural or artificial). The definition from Varnes (1958) describes a landslide as a "*downward and outward movement of slope-forming materials*" and assumes that the involved materials can be made of rock, soil, or artificial fill. This definition has evolved during the years. For example, in 1978, Varnes' classification (Varnes 1978) was expanded, especially by using a more precise terminology developed over the years between the two works. "Landslides", for example, became "slope movements" to comprehend all kinds of slope movements and not only the slides. For example, while the classification from 1958 includes falls, slides, flows and complex as types of movement, in the 1978 one topples and lateral spreads were added. Varnes' classification was updated again in 1996 (Cruden and Varnes, 1996). This update also included other parameters like the rate of movement (Table 2.1), state of activity (Table 2.2), distribution (Table 2.3), and style (Table 2.4), which were introduced years before by the UNESCO Working Party on World Landslide Inventory (WP/WLI, 1993). The Velocity scale is, quite self-explanatory, the rate of movement of the materials involved. It varies from the Extremely Rapid class 7 (velocity above 5 m/sec) to the Extremely Slow class 1 (slower than 16 mm/year). In Table 2.1, the Typical Velocity data represents the limit between two classes.

Table 2.1: Velocity scale proposed by Cruden and Varnes (1996).

Velocity class	Description	Velocity (mm/sec)	Typical Velocity
7	Extremely Rapid	5×10^{3}	5 m/sec
6	Very Rapid	5×10^{1}	3 m/min
5	Rapid	5×10^{-1}	1.8 m/hr
4	Moderate	5×10^{-3}	13 m/month
3	Slow	5×10^{-5}	1.6 m/year
2	Very Slow	5×10^{-7}	16 mm/year
1	Extremely Slow		

The State of activity (Table 2.2) is the description of the evolution of the landslide through time. It goes from Active (the landslide is moving at that exact moment) to Inactive (no movement in the last seasonal cycle).

Table 2.2: State of activity proposed by Cruden and Varnes (1996).

State of activity		Description
Active		In motion during the classification
Reactivated		Active again after being Inactive
Suspended		Not active right now, but active during the last seasonal cycle
Inactive	Dormant	Inactive landslide. In this case the causes of the movement are still apparent.
	Abandoned	In this case the causes of the movement are still apparent but they are not acting on the slope
	Stabilized	Landslide movement has been stopped by natural phenomenon or artificial remedial measures
	Relict	Inactive landslides developed under different climatic or geomorphic condition

The distribution of activity (Table 2.3) considers the spatial evolution of the surface of rupture, which is "*the lower boundary of the displaced material… below the original ground surface*" (WP/WLI, 1993).

Table 2.3: Distribution of activity by Cruden and Varnes (1996).

Distribution of activity	Description
Advancing	Surface of rupture expanding towards the direction of movement
Retrogressive	Expansion in the opposite direction of the direction of movement
Widening	Surface of rupture extending towards one or both lateral margins
Enlarging	The expansion is towards two or more direction
Confined	The landslide scarp is visible but no surface of rupture is visible in the foot of the displaced materials
Diminishing	The volume of displaced materials diminishes with time
Moving	The displaced materials are moving but the surface of rupture shows no changes

The style of activity (Table 2.4) describes the interaction between different types of movements of a landslide. This characteristic takes into consideration both spatial and temporal interactions between two types of movements.

Table 2.4: Style of activity by Cruden and Varnes (1996).

Style of activity	Description
Complex	Landslide characterized by at least two type of movements
Composite	Different type of movements in different areas of the displaced materials. Can happen simultaneously
Multiple	Repetition of a type of movement, usually subsequently an enlargment of the surface of rupture.
Successive	Same type of movement as a previous one but witouth sharing the surface of rupture or displaced materials
Single	Single type of movement for the entire displaced materials

Also landslide features have been defined to better characterize the events and describe the observable elements (Cruden and Varnes, 1996). The features (Figure 2.1a) and dimensions (Figure 2.1b) shown in this chapter in Figure 2.1 are the ones proposed in Cruden (1978), and the ones added in WP/WLI (1993) and in Cruden and Varnes (1996).

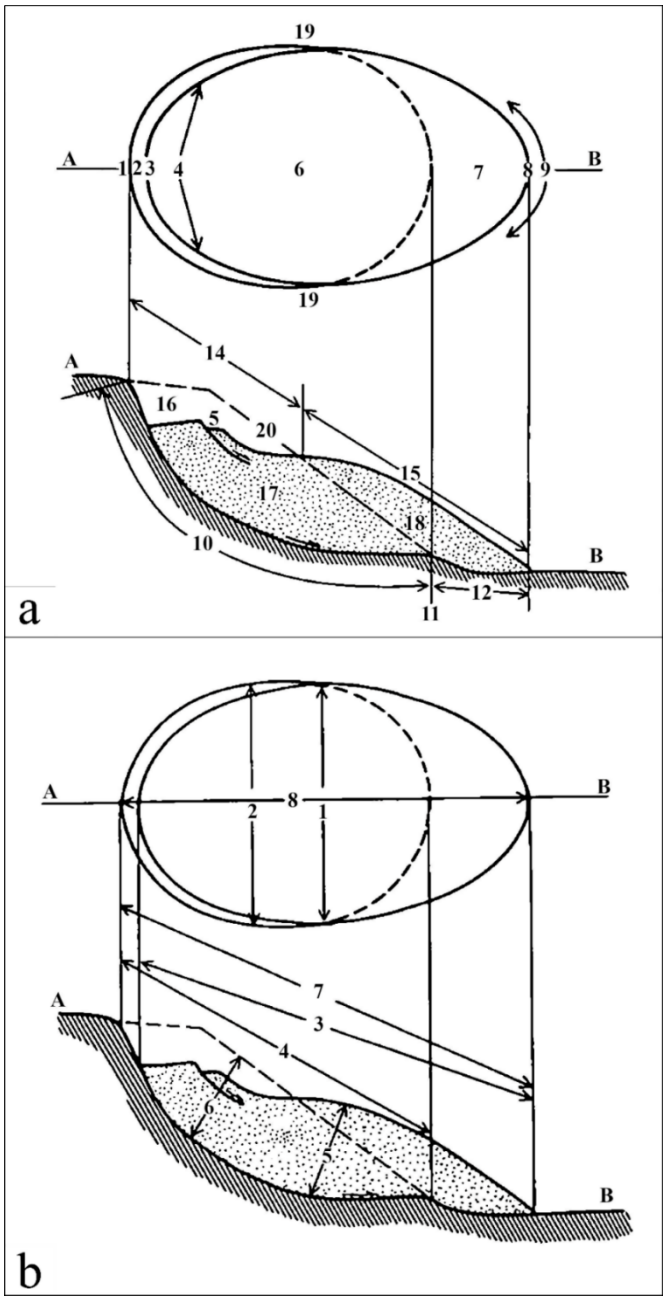

Figure 2.1: Landslide a) features and b) dimensions (modified from Cruden and Varnes, 1996). The dotted material is the displaced slope material and the dashed line is the surface level before the landslide. In a): 1) Crown; 2) Main Scarp; 3) Top; 4) Head; 5) Minor scarp; 6) Main body; 7) Foot; 8) Tip; 9) Toe; 10) Surface of rupture; 11) Toe of surface of rupture; 12) Surface of separation; 13) Displaced material; 14) Zone of depletion; 15) Zone of accumulation; 16) Depletion; 17) Depleted mass; 18) Accumulation; 19) Flank; 20) Original ground surface. In b): 1)Width of the displaced mass; 2) Width of the surface of rupture; 3) Length of the displace mass; 4) Length of the surface of rupture; 5) Depth of the displaced mass; 6) Depth of the surface of rupture; 7) Total length; 8) Length of the center line.

The type of movements are described as follows:

- Falls are detachments that descend through air by free fall. Subsequential leaps and rolls are included as part of the movement as well (Varnes, 1978). They fall within the Very Rapid and Extremely Rapid Velocity classes (Table 2.1).

- Topples are characterized by a forward rotation of the materials out of the slope due to gravity. The rotation center is located below or in the lower section of the toppling unit of materials (Varnes, 1978) and their velocity class can vary between Extremely Slow and Extremely Rapid (Table 2.1).
- Rotational and Translational slides occur by shear strain zones or along surfaces of rupture (which can be one or several) and in both cases the initial surface of rupture can be smaller than the final one as the moment does not occur at the same time over the entire surface of rupture (Varnes 1978). Rotational slides are characterized by an upward curved surface of rupture and a rotational slide movement in which the axis is located outside the slope (Varnes 1958) while Translational slides follow a more or less planar surface of rupture (Varnes 1978). In the Rotational slide backward tilting and vertical movement of the material can be found while in the Translational slide trenches can be found at the head of the landslide. Movement speed can vary from Extremely Slow to Extremely Rapid (Table 2.1) (Hungr et al., 2014).
- Spreads are usually related to very gentle slopes or flat areas. They are characterized by overall extension that can happen to either bedrock without a clearly visible surface of rupture often on the crests of ridges or when a stronger upper layer rests on extremely plastic or liquefied materials (Varnes 1978).
- Flows embrace a vast amount of cases sometimes easier to categorize (unconsolidated materials) than others (bedrock) (Varnes 1978). They can vary in velocity from Extremely Slow (Rock flow) to Extremely Rapid (Debris flow) (Table 2.1) and water content can also be extremely variable, to the point that in subsequent updates there is a more in-depth division between the different types of flows like *debris dry flow*, *debris flow* and *debris flood* (Hungr et al., 2014).
- Complex landslides are characterized by multiple, subsequential, type of movements.

Some years later, other authors updated the classification, adding new descriptors for the type of materials involved in the slope movement. It is the case of the classification by Hungr et al. (2014) (Table 2.5) that adds laboratory indices (if available) and corresponding unified soil classes to characterize the materials involved in the slope movements.

Table 2.5: Update of the Varnes' landslide type of movement classification, from Hungr et al. (2014).

Type of movement	Rock	Soil
Fall	*Rock* /*ice* fall	*Boulder* /*debris* /*silt* fall
Topple	Rock block topple	*Gravel* /*sand* /*silt* topple
	Rock flexural topple	
Slide	Rock rotational slide	*Clay* /*silt* rotational slide
	Rock planar slide	*Clay* /*silt* planar slide
	Rock wedge slide	*Gravel* /*sand* /*debris* slide
	Rock compound slide	*Clay* /*silt* compound slide
	Rock irregular slide	
Spread	Rock slope spread	*Sand* /*silt* liquefaction spread
		Sensitive clay spread
Flow	*Rock* /*ice* avalanche	*Sand* /*silt* /*debris* dry flow
		Sand /*silt* /*debris* flowslide
		Debris flow
		Mud flow
		Debris flood
		Debris avalanche
		Earthflow
		Peat flow
Slope deformation	Mountain slope deformation	Soil slope deformation
	Rock slope deformation	Soil creep
		Solifluction

These modifications allow to distinguish, for example, between clay or silt rotational slides or debris flows and debris floods. It also adds materials like ice or organic-rich materials like peat. As for the type of movements, Hungr et al. (2014) also added a new type: slope deformation. This type describes the large-scale gravitational deformation along mountain or hill slopes. Both Mountain and Rock slope deformation are characterized by the presence of trenches, tension cracks, lack of a fully defined rupture surface and an extremely slow movement rate (Hungr et al., 2014).

2.2. Sinkholes

Sinkholes are characterized by an enclosed depression, regardless of the presence of an internal drainage (Waltham and Fookes, 2003), with a predominantly subcircular shape in plan view, and a varying three-dimensional shape (cylindrical, conical, bowl-like, etc…) (Gutiérrez, 2016). Sinkholes are widespread all over the world from the Americas (Beck, 1986; Ford, 1997; Silva et al., 2017), to Africa (De Bruyn and Bell, 2001; Mouici et al., 2017; Muzirafuti et al., 2020), Asia (Gongyu and Wanfang, 1999; Taheri et al., 2015; Zhou et al., 2016), Europe (Nisio et al., 2007; Galve et al., 2008; Hofierka et al., 2018) and Oceania (Twidale 1987; Martins, 2019; Burke et al., 2020). The name perfectly showcases the actual process: firstly water enters an enclosed depression and infiltrates underground; subsequently, there can be local ground erosion due to water that washes away the surface material followed by subsidence due to the dissolution of soluble rock underground. This dissolution can form underground cavities that can, eventually, collapse (Waltham et al., 2005).

There are several sinkhole classifications, mostly focused on the process that caused the sinkhole. Williams (2003) separates sinkholes into four general categories based on the processes that initiate them:

- Dissolution in carbonate and evaporite rocks;
- Collapse of the roof of the underground cavity; in this case Williams recognizes three sub-categories based on the materials involved (same or different materials for the roof of the cavity and the cavity itself);
- Suffosion dolines in unconsolidated sediments trough solution pipes;
- Regional subsidence over large areas due to dissolution of deep layers.

Gutiérrez et al. (2008) proposed another sinkhole classification (Table 2.6), including elements from previous classifications (Beck, 2004; Waltham et al., 2005) that considered the type of material involved in the collapse. This classification, updated in 2014 (Gutiérrez et al.,

2014), divides sinkholes into two groups: solution sinkholes and subsidence sinkholes. Multiple authors (Williams, 2003; Waltham et al., 2005; Gutiérrez et al., 2008;2014) define the three materials as: (i) Cover: soils or unconsolidated deposits; (ii) Bedrock: karst rocks; (iii) Caprock: non karst rocks.

Table 2.6: Sinkhole classification, modified from Gutiérrez et al. (2008; 2014).

	Subsidence sinkholes		
	Collapse	Sagging	Suffosion
Cover	Cover collapse sinkhole	Cover sagging sinkhole	Cover suffosion sinkhole
Bedrock	Bedrock collapse sinkhole	Bedrock sagging sinkhole	
Caprock	Caprock collapse sinkhole	Caprock sagging sinkhole	

Solution sinkholes
Solution sinkhole

After the first descriptor (the material), the second word describes the type of process related to the sinkhole initiation.

- Collapse: refers to the brittle deformation of the overlaying material;
- Sagging: is the ductile deformation;
- Suffosion: it happens when the unconsolidated deposits or soils are washed downward due to presence of a cavity. The settling of the material is part of the process.

The sinkholes described are related to natural processes and the formation of natural underground cavities. However, sinkholes can also be related to artificial cavities, either excavated by humans or directly caused by them. These sinkholes are called in the literature "anthropogenic sinkholes" (Caramanna et al., 2008; Guarino and Nisio, 2012; Parise, 2015). These sinkholes are often triggered by aqueduct or sewage network leaks (Guarino et al., 2018) that can remove underground soil, producing small cavities, or by the collapse of an underground void (caves, mines, etc…). Another important triggering factor is rainfall (Parise et al., 2018).

2.3. Floods

Floods are defined as a "*natural process that occurs when the level of a body of water rises until it overflows its natural banks or artificial levees and submerges areas usually dry*" (Luino, 2016). It is a geohazard widespread all over the world (Reichenbach et al., 1998; Coates, 1999; Douben, 2006; Modarres et al., 2016; Hodgkins et al., 2017) mostly caused by prolonged or short but extreme hydrometeorological events (Bracken et al., 2008; Sangati and Borga, 2009; Wei et al., 2018) and snow or rain-on-snow melting (Marks et al., 1998; Yang et al., 2009; Parajka et al., 2010).

The hydrographic network of the city of Naples is characterized by the presence of some hills and by an alluvial plain to the east. The Sebeto River flowed in the eastern sector of the city but, from the beginning of the 20th century (Ducci and Sellerino, 2015), the area was heavily urbanized and the river has been anthropized and covered. As shown by the available data from the Southern Apennines River Basin District Authority (Figure 2.2), the city sector where the Sebeto River flowed is now a Low Flood Hazard class, (same for the *Agnano* Plain, in the western sector). A dense hydrographic network, which has been partially incorporated into the urban fabric, is present in the hilly sectors of the city, where the outer rim of the Phlegrean Fields caldera is located (Ascione et al., 2022). As forementioned, due to the incorporation of the most downstream sectors of the channels into the urban fabric, these areas are sometimes unable to manage the local discharge from the streams (Ascione et al., 2022) and are part of the High Flood Hazard class. This is the case of the "*Lava dei Vergini*" (Lava of the Virgins): this is the name attributed to the periodic floods that recurringly impacted the *Sanità* neighbourhood during the first six decades of the last century (Rapalo, 2018). The Sanità neighbourhood is located at the foot of the *Capodimonte* and *Colli Aminei* hills, underwent strong anthropization, and was characterized by an inadequate and clogged sewer system. Whenever the city was hit by severe rainfalls, floods and debris flows would impact the area, sometimes causing victims

and extensive damage. During the sixties and seventies, the local administration performed extensive maintenance and improvement of the sewer network, which led to the "*Lava dei Vergini*" becoming a phenomenon that lives only in the historical memory of older generations. Despite the improvement of the sewer system, floods continued to hit the city of Naples. In September 1969, a flood caused, in addition to direct flooding damage, the formation of a 15-meter deep sinkhole in Via Aniello Falcone (*Vomero* hill).

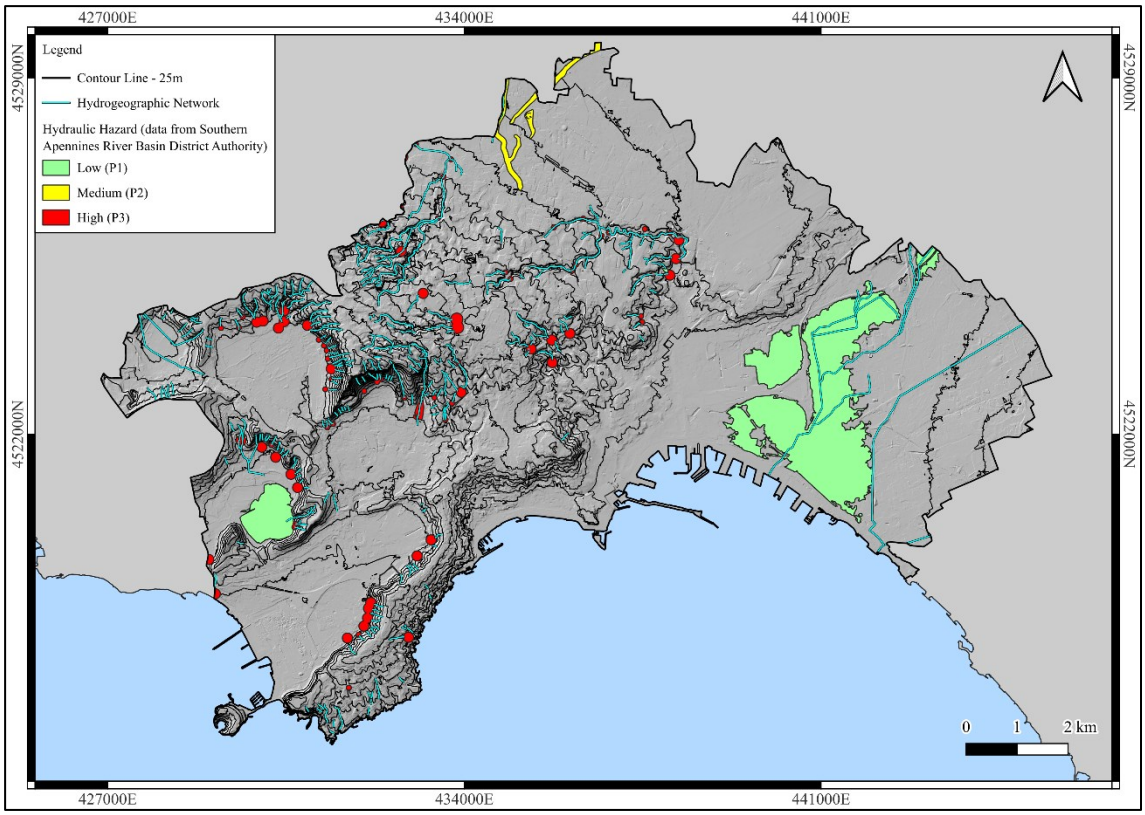

Figure 2.2: Hydrographic Network of the city of Naples and Hydraulic Hazard map provided by the Southern Apennines River Basin District Authority.

3. RISK ASSESSMENT

The objective of this research project is the modelization of different geohazards, the evaluation of the influence they can exert on each other and their impact on the urban fabric. The multi-geohazard risk evaluation is one of the steps toward a more resilient city. The concept of resilience is widely used in various fields, from medical to urban development (Holling, 1973; Folke et al., 2010; Meerow et al., 2016). The focus of this research project is the production of a useful tool that stakeholders can utilize to manage geohazard risk in the context of urban resilience related to the still-expanding present day cities. Urban resilience *"refers to the ability of an urban system all its constituent socio-ecological and socio-technical networks across temporal and spatial scales to maintain or rapidly return to desired functions in the face of a disturbance, to adapt to change, and to quickly transform systems that limit current or future adaptation capacity*" (Meerow et al., 2016). Therefore, considering the previous definition, the geohazards considered in this PhD project are going to be modelled in relation to their impact on the urban and social fabric. Risk, by definition, represents the measure of probability and severity of the occurrence of a phenomenon that can potentially cause damage to things or people (Fell et al., 2008). One of the formulas used to evaluate the Risk is the following one, proposed by UNESCO (Varnes and IAEG, 1984):

$$R = H \times V \times E$$

In this formula R represents the Risk, H is Hazard and represents the probability that a given event will happen in a certain area, with a certain intensity, within a certain time interval. Considering the definition of landslide susceptibility provided by Fell et al. (2008), we can consider it as "*A quantitative or qualitative assessment of the classification, volume (or area) and spatial distribution of...*" a phenomenon "*...which exist or potentially may occur in an area.*" Therefore, susceptibility does not consider the temporal distribution of the phenomenon and the consequent return period. Not all inventories, however, contain information on the date

of occurrence of the event. This is because the occurrence temporal information falls within the "intermediate" activities related to inventory production (Fell et al., 2008). This is especially true for landslides as they can trigger in uninhabited areas, making it difficult to evaluate the precise date of occurrence. In this case, since approximately 57% of the landslide inventory and 100% of the flood inventory do not contain temporal information, it was decided to use the susceptibility instead of the hazard to evaluate the risk. About 99% of the entries in the sinkhole inventory contain, at minimum, information about the year of occurrence. To uniform the risk assessment process, we also decided to use susceptibility instead of the hazard for the sinkholes.. The parameter V of the previously shown Risk formula is Vulnerability, the degree of loss of a specific element due to the event, which can vary from 0 to 1 (damage compared to the total cost of the good for an object or an economic activity and probability of death of an individual in the case of people). As the geohazard inventories information on the damage caused by the events is often unavailable or incomplete, Vulnerability is a complicated parameter to define especially in highly urbanized areas with an high population density. Given the extension of the area analyzed and the incompleteness of the damage data (the sinkhole inventory, for example, does not contain complete data while the flood inventory is obtained by sampling the original data from the Basin Authority) it was decided to employ a precautionary approach and evaluate the Vulnerability for the entire area by assigning it the value of 1. Lastly, the parameter E represents Elements at Risk (people, private property, infrastructure, public services, economic activities, etc...).

3.1. Relative hazard assessment: methodological approach

There are three different approach to evaluate Susceptibility, from now on called Relative Hazard, after Parise (2001):

- Deterministic approach, which involves the use of well-defined formulas or algorithms for determining slope stability in terms of Safety Factor. These methods are usually used on small areas (slopes or little basins).
- Heuristic approach. The sensitivity and experience of the operator is the main factor that leads to the choice of the type of predisposing factors considered relevant.
- Statistical approach. This approach appears to be the most objective and reproducible given the presence of a strong algorithmic component which clearly outlines the steps that must be followed to produce the susceptibility maps. The statistical approach itself can be divided into bivariate and multivariate methodologies. In the first case, the contribution of each predisposing factor is evaluated individually in regard to the other ones and divided into different classes, while the multivariate approach analyzes more than two parameters at the same time to evaluate their relationships.

Among statistical methods, Machine Learning (ML) has found widespread use. Mitchell (1997) defines ML with the following description: "*A computer program is said to learn from experience E with respect to some class of tasks T and performance measure P, if its performance at tasks in T, as measured by P, improves with experience E.*" In the context of engineering geology, task T represents the susceptibility evaluation of a geohazards and P, the performance, refers to the model validation. The experience E is related to the training phase of a ML algorithm. All ML algorithms share a common need for presence data to perform their tasks. This is because, as a statistical method, ML is based on the concept that if a phenomenon occurs within a certain range of values for a set of predisposing factors, or predictor variables, then the same conditions can trigger the same phenomenon in the future. ML carries out this training phase semi-autonomously, determining any correlations between presence and absence

points with the predisposing factors and determining the influence of these last on the phenomenon.

As already stated, ML algorithms consist of a program that tries to find the best model that describes the interaction between a phenomenon and the predisposing factors that the user provides. An ML in itself is not able to distinguish when two predictor variables are closely related to each other. This is one of the problems that can affect ML algorithms, called collinearity. James et al. (2021) define collinearity as "*...the situation in which two or more predictor variables are closely related to one another*". These two parameters tend to have a similar influence on the model, making it difficult to evaluate the impact of a single predisposing factor. In this study, an additional step has been added to the Relative Hazard assessment: the evaluation of the Variance Inflation Factor (hereafter VIF). This is a useful tool used to find out if there are collinearity problems. The VIF is calculated with the following formula (modified from James et al., 2021):

$$VIF_j = \frac{1}{1 - R^2_{x_j|x_{-j}}}$$

In this formula, $R^2_{xj!x\text{-}j}$ is the R^2 value of the regression between the predisposing factor *j* to the other factors. It is, in other words, a coefficient that defines how well a model describes the outcome. In this case, two predisposing factors that can well-define each other using a linear model are going to be characterized by a high R^2 value. The closer the R^2 is to 1, the higher is the value of VIF. On the other hand, if the R^2 value is extremely low, the VIF value is lower. The minimum value that can be assumed is 1, which indicates the total absence of collinearity. James et al. (2021) suggest, as a general rule, to be careful with parameters whose VIF value exceeds 5. In this study, any predisposing factor whose VIF score is higher than 5 is going to be excluded from the Relative Hazard assessment.

Other techniques employed to increase the performance of the Relative Hazard maps and to avoid overfitting are the selection of a separate set that will not be involved in the production of the models (a test set) and the employment of validation sets through the use of the K-Fold Cross-validation technique. The test sets were randomly selected from the three inventories, keeping a 70/30 ratio between training and test sets. Employing a test set limits the number of presence points that will be used to train the models but, on the other hand, the test set is an unbiased method to evaluate the actual performance of the model. As for the validation sets, they still uses data that has been used to produce the models which makes them, therefore, characterized by a positive bias (Abu-Mostafa et al., 2012). The test set will be used only to evaluate the performance of the final Relative Hazard assessment products (the ones obtained through EM), while the K-Fold Cross-validation technique will be employed on the remaining training data that will be used as presence points by the ML algorithms. With this approach, the entire training dataset is divided into *k* sets (also called folds) containing approximately the same number of elements. The modelling process is then performed *k* times and, at each iteration, a different set *k* is used for the validation phase, while the remaining *k*-1 sets are used for model training (James et al., 2021). At the end of the modelization phase, the final result obtained is an average of the performance of *k* iterations. The performance score of the models, a mean obtained using the K-Fold Cross-validation approach, has been used to evaluate the best models (those that overcome a certain threshold) to be used in the following EM phase.

To produce the relative hazard maps, an Ensemble Modeling (EM) approach was employed using the "*biomod2*" (Thuiller et al., 2024) package in R (R Core Team, 2023) and R Studio (Posit Team, 2024). Other packages used are the "*sf*" (Pebesma, 2018; Pebesma and Bivand, 2023) and "*terra*" (Hijmans, 2024a) packages for spatial data analysis, "*usdm*" (Naimi et al., 2014) for the VIF investigation, "*tidyterra*" (Hernangómez, 2023), "*ggplot2*" (Wickham, 2016), "*ggtext*", "*raster*" (Hijmans, 2024b) for the elaboration phase and plot creation, and

"*modEvA*" (Barbosa et al., 2013) for the Ensemble Model performance evaluation. The EM approach is a technique that aims at reducing the error of the model and keeping it as general as possible by combining multiple products of different models and different input data (Kotu and Deshpande, 2015). This approach has been applied to systems that show chaotic behaviour and lots of uncertainty like atmospheric modeling (Parker, 2013). As previously stated, EM combines multiple models and, in this case, the two models employed are the Maximum Entropy (Phillips and Dudìk, 2008) and the Random Forest (Breiman, 2001) algorithms.

The first one was developed as a tool for species distribution (Phillips et al., 2004). During the years, it has also been largely used in other fields, such as susceptibility assessment (Convertino et al., 2013; Allocca et al., 2021). The MaxEnt algorithm relies on the assumption that the best model that describes the spatial distribution of a species or a geohazard is obtained by maximizing the entropy. The latter is the degree of resolution of the system and it is also used to measure how important the choice of a parameter or environmental variable is within a model (Phillips et al., 2004). In practice, the algorithm uses the presence dataset and the background data to evaluate which landscape factors (the predisposing factors) support an higher density of presence points. In other words, MaxEnt compares the predisposing factors data obtained in correspondence of the background points (randomly chosen points within the study area) and compare them to the ones collected within the Presence Points and recognizes the areas that are more likely to fall within an hypothetical collection of cells with an high indices of habitat suitability (Merow et al., 2013). When the algorithm starts its computational phase, the predisposing factors weights in the model are assessed through an iterated process, varying the weights at every cycle and evaluating the log loss (a value that determines how well the model fit the training data). When the log loss value obtained is smaller than a threshold value (standard value is 1×10^{-4}, called convergence) the iteration process stops. As this process could, potentially, have no end, a maximum number of iterations is provided by the user. The

process is stopped whenever the convergence or the maximum number of iterations are reached. In this study, a precautionary high value of maximum iterations has been provided (2000) to allow the algorithm to converge its model (Phillips et al., 2006). The model obtained at the end of this process is the aforementioned best model. It corresponds to the model without initial hypotheses, which can lead to the phenomena occurrence (or, as stated in the previous sentence, can individuate the areas with the best habitat) with any combination of predictive variables since it has the maximum uncertainty on occurrence probability (Phillips and Dudik, 2008). To evaluate the performance among the produced models, MaxEnt uses the validation data related to the K-Fold Cross-validation approach. As for the predisposing factors importance, on the other hand, MaxEnt utilizes the data permutation approach. The permutation process involves modifying the data contained in a specific predisposing factor, and replacing its values with totally random ones: if the new random values of the predisposing factor lead to a strong reduction of the model performance, then the analyzed parameter is important for geohazard modelling. On the other hand, if the permutation does not influence the final performance, then the analyzed predisposing factor was not important for modelling purposes. Any loss of performance is measured and the difference between the performance before and after the permutation allows the evaluation of the predisposing factor importance for the model.

The Random Forest algorithm (Breiman, 2001), on the other hand, is an ML algorithm that is sometimes also classified as an Ensemble Model, as it uses a "forest" of decision trees to perform classification or regression operations. After building this "forest" of decision trees, the products are combined into a singular, final, model, integrating the information obtained from this training phase. Decision trees are often easier to understand, as they work similarly to the human's decision process. An example could be the application of a decision tree to the problem "Should I go out for a walk?" (Figure 3.1).

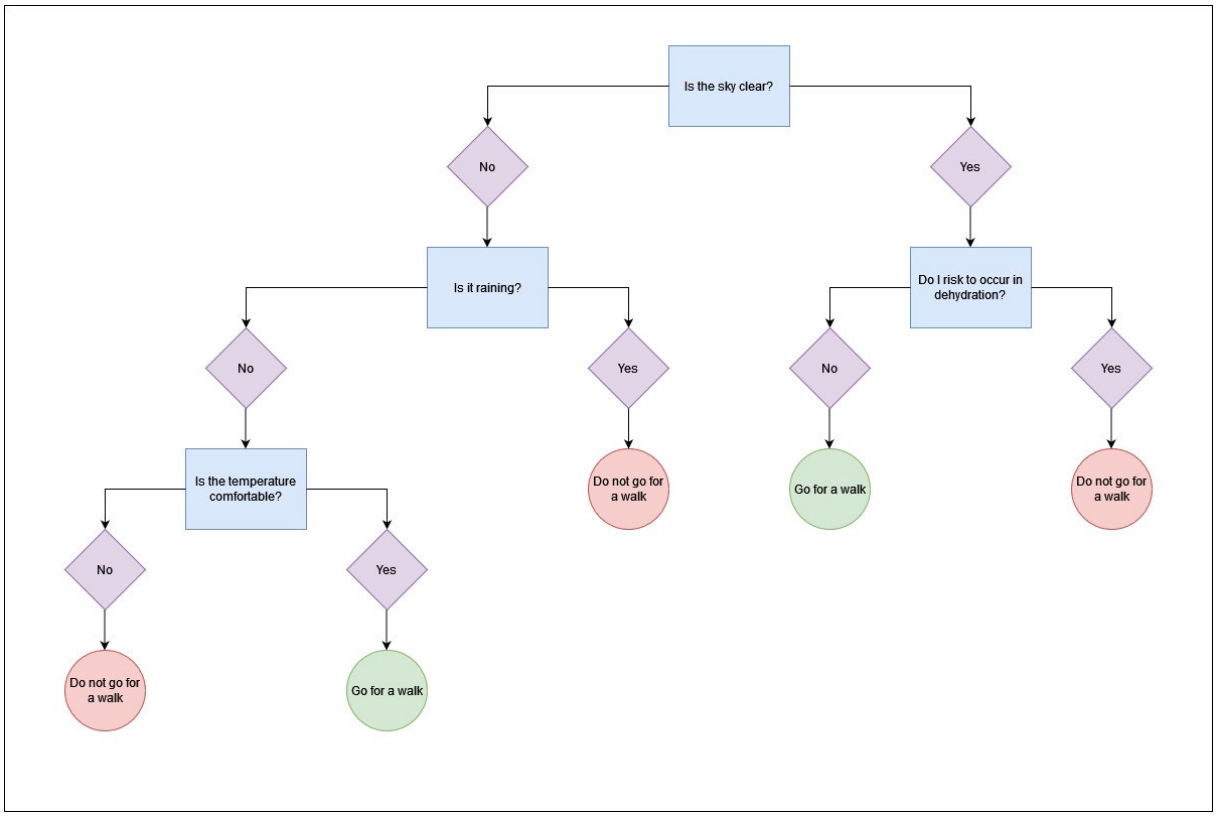

Figure 3.1: Example of a simple decision tree.

There are multiple variables to consider when we have to make such a decision. For example, the first node (or choice, in our example) would be "Is the sky clear today?" This first step produces the first two branches of the tree, as the answer could be either "Yes" or "No". This could already be the end of our (short) tree, but its length depends on the amount of information we are feeding it. For example, we could still decide to go for a walk, even if the sky is not clear, depending on other information such as "Is it overcast or is it raining?". At the end of the branches we find the "leaves", the end nodes, in this case "Go for a walk" or "Do not go for a walk". The provided example is more closely related to a classification tree ("to go" or "not to go", "1" or "0"), rather than a regression, but the concept is exactly the same: the difference is that for every node there are one or more predisposing factors that are being analyzed and used for our model. The simplicity of use due to the few parameters to be set makes the RF algorithm widely used in the susceptibility assessment for different types of geohazards (Lee et al., 2017; Taalab et al., 2018; Bustillo Sánchez et al., 2021). As already

stated, the "forest" is built on multiple decision trees. Multiple authors (Biau and Scornet, 2016; Probst et al., 2019) suggest that the higher is the number of trees, the better is the performance of the final product. This is partially true as the performance gain is asymptotic and, for this reason, the performance gain obtained using 10000 trees instead of 9500 trees is smaller than using 600 trees instead of 100. Other important parameters that must be set by the user are:

- *mtry* which is the number of splitting directions at every node of the decision tree. In the simplified decision tree in Figure 3.1 *mtry* is equal to 2 but, usually, this value is equal to $\sqrt{p}$ for classification and $^{p}/_{3}$ for regression trees, with p representing the number of predisposing factors. As the VIF analysis was employed in this study, it is not possible to know beforehand the *mtry* value, although the $^{p}/_{3}$ formula has been used.
- *nodesize* is the maximum amount of observations in the "leaves" of the trees. Standard values for this parameter are 1 for classification and 5 for regression decision trees. This value usually influences also the depth of the tree as a node with 4 observations can still be a node for a classification tree (or any tree with *nodesize* > 4) or a leaf for a regression tree (or any tree with *nodesize* ≤ 4).

Both models need background Points (or Pseudo-Absence points) to perform their algorithms. The amount of Pseudo-Absence (hereafter PAb) points has been chosen after evaluating literature data. The MaxEnt algorithm, like the Generalized Lineal Models and the Generalized Addictive Models ones, performs well with a high number of PAb points (1 set of 10000 points) while RF performs better with 10 sets of less than 1000 PAb points or as much points as the Presence Points (Barbet-Massin et al., 2012). In the end, a total of 10 different set of *n* number of PAb points (with *n* equal to the number of training presence points) have been used for the Relative Hazard assessment with the RF algorithm, while 5 set of 10000 PAb points

have been used for MaxEnt. Combining the different sets with the K-Fold Cross-validation technique (with $k = 3$) a total of 45 models (15 obtained with the MaxEnt algorithm and the remaining 30 with Random Forest) were produced for every geohazard. As already stated, the models obtained with these algorithms are combined in a Relative Hazard Map. Every models' contribution are weighted depending on their ROC score obtained through the cross-validation process: an higher ROC score corresponds to an higher weight. After the weight attribution, the models are combined as a weighted mean of the prediction. The Relative Hazard maps performance were measured via ROC/AUC analysis. This method calculates the Receiver Operating Characteristics (ROC) curve and, subsequently, the relative Area Under the Curve (AUC). The ROC is a binary graph (Table 3.1) built using the true positive (areas influenced by a geohazard and detected as a criticality), true negative (areas not affected by a geohazard and not recognized as a criticality), false positive (areas not influenced by a geohazard recognized as a criticality) and false negatives (areas impacted by a geohazard but not recognized as a criticality) values.

Table 3.1: Relationship between Geohazard and Prediction. Positive for the Geohazard indicates the presence of an event, while negative indicates that nothing happened.

		Geohazard	
		Positive	Negative
Prediction	Positive	True Positive	False Positive
	Negative	False Negative	True Negative

On the abscissas of the graph the Specificity (as 1 – Specificity) is located which represents the ratio between true negatives and total negatives detected:

$$Specificity = \frac{true\ negative}{true\ negative + false\ positive}$$

On the ordinates, instead, the Sensitivity is located which represents the relationship between true positives and the total positives detected:

$$Sensitivity = \frac{true\ positive}{true\ positive + false\ negative}$$

The EM performance evaluation is carried out using the 30% of presence data that has been kept outside of the first modeling phase. Using these totally independent data, the AUC of the ensembles is evaluated: the closer this value is to 1 (100% of the available area), the more reliable the model is and, on the contrary, the lower the value, the worse the model performance. With an AUC score of 0.5 the prediction is considered random, while an AUC score greater than 0.9 indicates an excellent prediction (Swets, 1988).

3.2. Census Areas and Exposed Value

The Census Areas is a tool introduced by the italian government after World War II, in 1948, to manage the production and disclosure of statistical data (Alleva, 2018). In fact, it was only after the abovementioned war that the Italian territory was divided in Regions, Provinces and Municipalities. The Census Areas data is freely available on the ISTAT website (https://www.istat.it/notizia/dati-per-sezioni-di-censimento/ - in Italian) and the last update is related to the 31/12/2021 census data. Historical data are available starting from 1861 up to 2001, updated every 10 years (except for 1891 and, for obvious reasons, 1941). Since 2001, the census data has been updated yearly (last data available at the time of writing, 1st of January 2024, not available for the Census Areas). In this study, the Census Areas (Figure 3.2) are going to be the first step for the evaluation of the Elements at Risk. From the Census Areas the number of inhabitants for every section has been obtained from the ISTAT data. Starting from the shapefile of the Census Areas and the number of inhabitants, the population density has been evaluated. As this data is not enough to describe the complexity of the city area, other four layers have been used to determine the Exposed Value:

- Road network: which was divided into two categories i) strategic network (highways and primary arteries) and ii) secondary network;

- Railway network: that was treated as a strategic element in its entirety;

- Buildings layer: divided into strategic buildings (hospitals, schools, museums, airports, ports, train stations, government and civil buildings) and non-strategic ones.

- Regional Parks layer: represented by the Hills of Naples Metropolitan Regional Park (*Parco Regionale Metropolitano delle Colline di Napoli*) and by the Phlegrean Fields Regional Park (*Parco Regionale dei Campi Flegrei*).

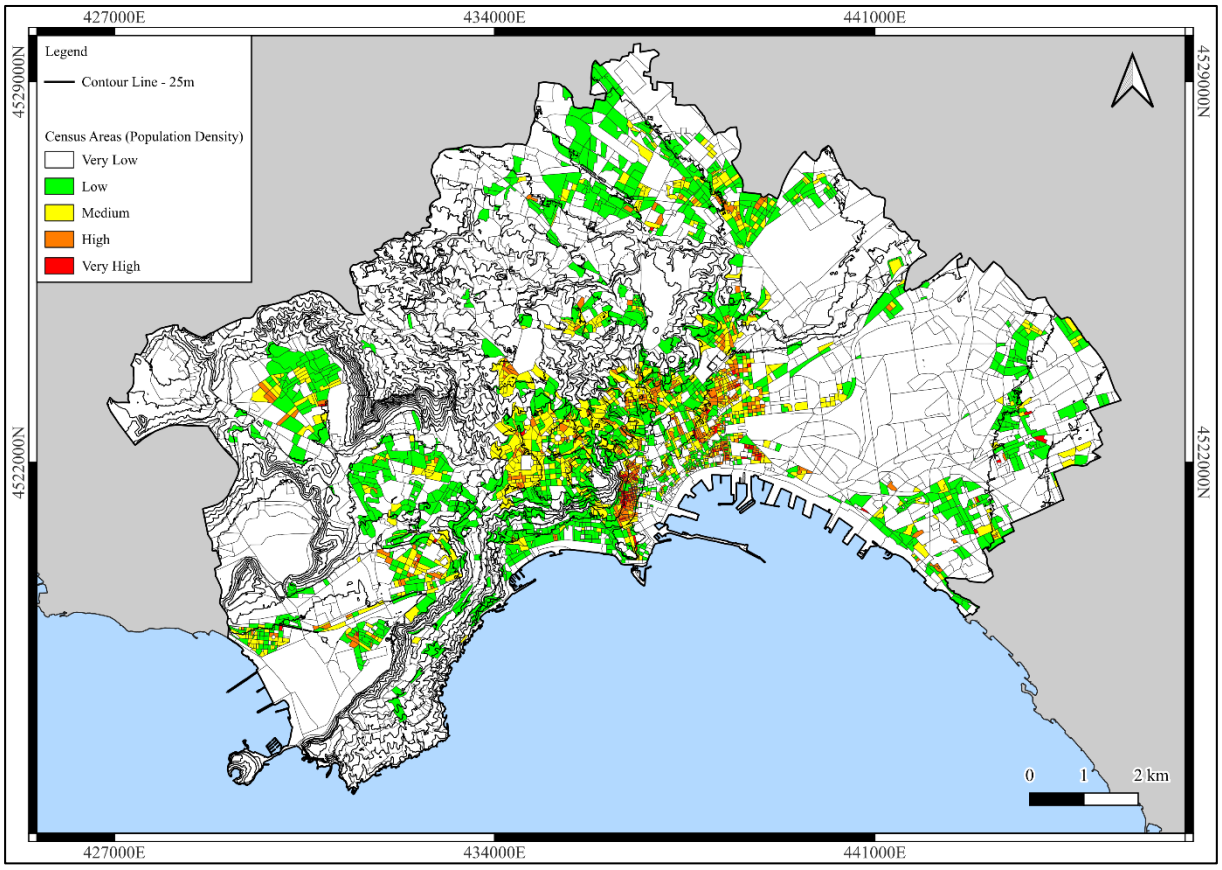

Figure 3.2: Census areas of the city of Naples classified by Population density.

These layers have been downloaded as shapefiles from the Municipality of Naples website (*https://www.comune.napoli.it/opendata*).

3.3. Risk and Multirisk assessment

The Risk will be obtained using the conventional formula from UNESCO (Varnes and IAEG, 1984):

$$R = H \times V \times E$$

As stated before, E represents Elements at risk (people, private property, infrastructure, public services, economic activities, etc...) while V is Vulnerability, i.e. the degree of loss of a specific element following the event, which can vary from 0 to 1. H is Hazard, which is described by Fell et al. (2008) as "*A condition with the potential for causing an undesirable consequence. The description of ... hazard should include the location, volume (or area), classification ... and the probability of their occurrence within a given period of time.*" As stated in previous paragraphs, the Return Period information is not available for all the inventories. For this reason, in this study, Hazard will be substituted by Relative Hazard. As V has been set as 1 for the entire study area, the aforementioned formula becomes:

$$R = RH \times D$$

Where RH is Relative Hazard and D is Damage (Elements at Risk × Vulnerability, which is equal to 1 as a precautionary measure). To combine the two elements of the equation, the following Risk Matrix (Table 3.2) was used:

Table 3.2: Matrix for the Risk evaluation. H is the Relative Hazard and D is the Damage.

Risk Matrix	P0	H1	H2	H3	H4
D0	R0	R0	R0	R0	R0
D1	R0	R1	R2	R2	R3
D2	R0	R2	R2	R3	R3
D3	R0	R2	R3	R3	R4
D4	R0	R3	R3	R4	R4

To evaluate the geohazards' impact on each other, the Rock Engineering Systems (Hudson, 1992) was employed. It is an incredibly flexible method that can be applied to a vast

number of fields, from landslide susceptibility (Rozos et al., 2011; Tavoularis et al., 2021) to rock mass classification (Huang et al., 2013; Andriani and Parise, 2017). The RES' principal tool is the interaction matrix (Table 3.3). The parameters that describe the examined system are located in the diagonal cells of the interaction matrix. According to Hudson, the parameters along the diagonal can also represent concepts, making this method extremely flexible. In this study, the parameters of the "Multirisk" system along the diagonal will be the Relative Hazard maps. Nothing prevents the operator from changing the scale of analysis and, instead, using the Landslide Relative Hazard as the system and transforming the predisposing factors into the parameters of the interaction matrix. In this matrix, the effects are indicated along the columns, i.e. the impacts that other parameters have on the parameter under examination (green cells in Table 3.3). Along the columns, however, the causes are represented, i.e. how the parameter in question influences the other parameters (orange cells in Table 3.3). In the last row and the last cell, the sum of the causes and effects of each parameter is calculated and projected in the Causes-Effects diagram.

Table 3.3: Simplified example of the Interaction Matrix.

					Causes
	Parameter 1	Effect of the Parameter 1 on the Parameter 2			
	Impact of the Parameter 2 on the Parameter 1	Parameter 2	Impact of the Parameter 2 on the Parameter …	Impact of the Parameter 2 on the Parameter n	Sum of the impacts of the Parameter 2 on the other Parameters
		Effect of the Parameter ... on the Parameter 2	Parameter …		
		Effect of the Parameter n on the Parameter 2		Parameter n	
Effects		Sum of the other Parameters Effects on the Parameter 2			

This tool can also be used for multi-level analysis. For example, a Multirisk system can use different geohazard susceptibilities as parameters. This type of matrix would be called a first-level matrix. On the other hand, each "susceptibility" parameter could, in turn, become a system for another interaction matrix that uses the predisposing factors as parameters, resulting in a second-level matrix. The resolution of the matrix is governed by which type of system is going to be analyzed and the degree of definition of the parameters. A finer resolution matrix (more parameters) analyses the most basic relationships between several simple parameters. On the other hand, a coarse matrix aggregates several elementary parameters into one, more complex, parameter. For an effective use of the RES, the first step must be the ascertainment of the primal objective. Only then it is possible to move on to the analysis of the system interactions to identify the matrix parameters. At this point, the next step is the study of the parameters' interactions. These must be evaluated based on the context, allowing the operator to exclude any parameter that would prove to be irrelevant. Finally, after the user has reached an in-depth knowledge of the system, the interaction matrix can be codified. This operation occurs via a semi-quantitative process. It means that the operator, based on his experiences and knowledge, will attribute a numerical value to all the interactions (Causes and Effects) between the parameters. At this point, the operator has fully studied the system and can obtain a product that will satisfy the initial objective.

In this study, the objective set for the RES analysis is the production of the Multirisk Interactivity map obtained from the geohazards (the system parameters). Starting from the values of Causes (C) and Effects (E) obtained from the interaction matrix, it is possible to plot the parameters in the Causes-Effects diagram (Figure 3.3).

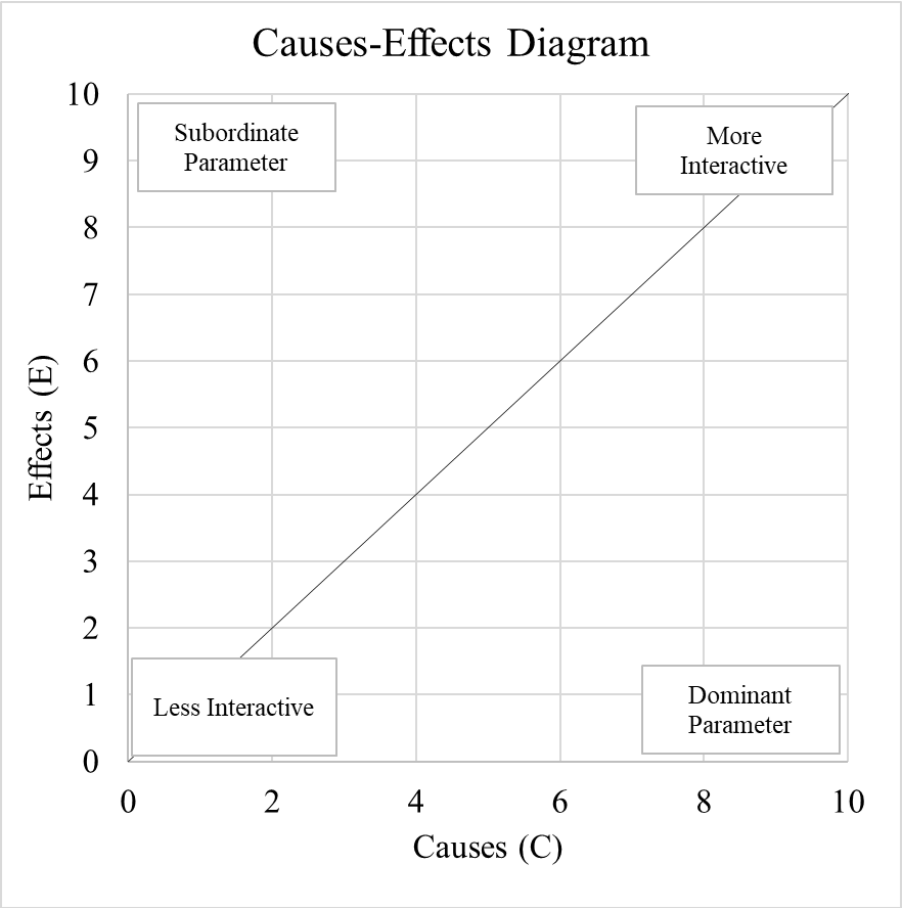

Figure 3.3 Causes-Effects diagram.

The diagram allows the operator to define two characteristics of the parameters. The first one is the degree of interactivity. When a parameter is characterized by high values of both Causes and Effects, the parameter is more interactive. On the contrary, with low values of Causes and Effects, the parameter is less interactive. The other characteristic is the dominance of the parameter within the system. Parameters with values of Causes > Effects are defined as dominant and the greater the gap between the two, the more dominant the parameter is. Otherwise, the parameter will be subordinate. The interactivity of the parameters, i.e. their propensity to interact with other parameters, is calculated according to the following formula:

$$Interactivity\ [\%] = I_i[\%] = \frac{C + E}{\sum_{i=1}^{n}(C_i + E_i)} \times 100$$

Where I_i is the Interactivity value, in percentage, of the i-th parameter, C + E is the sum of Causes and Effects of the same parameter and $\sum_{i=1}^{n}(C_i + E_i)$ is the sum of all the Causes and Effects of all parameters. To obtain the Interactivity value of a parameter the operator must sum the Causes and Effects values of a parameter and then compare it to the sum of all the Causes and Effects of the parameters, as shown in the formula above. This value, which gives a quantitative measure of the influence of a parameter within the Multirisk system, will be used as the basis for the final Multirisk assessment.

4. STUDY AREA

The coastal city of Naples, which has been chosen as the study area, is located in Italy, south of the Campanian Plain and bordering the Somma-Vesuvius volcanic complex at east (Figure 4.1) and the Phleagrean Fields at west. The municipality of Naples falls within the following coordinates: 426865.92E and 445528.72E, and 4515900.73N and 4529696.92N, EPSG (European Petroleum Survey Group) Code 32633 (WGS84 / UTM zone 33N).

Figure 4.1: Arenella and Vomero Hills as seen from the Camaldoli Hill, the highest hill of the city. On the background, the Somma-Vesuvius volcanic complex.

Due to its strategic location in the middle of the Mediterranean Sea, during the centuries Naples was an important commercial hub and a cultural and political center. The city was the capital of the pre-unity State of the Kingdom of Two Sicilies and, before that, the Kingdom of Naples, which political control was disputed between foreign world powers like France, Aragon and Spain. Nowadays it is one of the main cities of Italy (913.462 inhabitants in the historical urban centre, data from the *Istituto Nazionale di Statistica* ISTAT, National Institute of Statistics, 1st of January 2023, https://demo.istat.it/) and the capitol city of the *Campania*

Region. Since the 1st of January 2015, the entire Province of Naples was merged into the Metropolitan City of Naples (Law n. 56, 7th of April 2014) which made it the third most populous city in Italy after Rome and Milan (2.969.571 inhabitants, ISTAT, January 2023, https://demo.istat.it/).

The oldest traces of the city are found close to the *Pizzofalcone* hill (also called God's Mount – *Monte di Dio*), where the Cumaen colonizers established the City of Parthènope, during the VIII century B.C. The city became a commercial hub situated between the Mediterranean trade routes that went from Greece to the west side of the Mediterranean Sea. The name of the City, Naples, comes from the second foundation carried out, again, by Cumaen colonists, around 470 B.C. This new city took the name of Neapolis (New City) (Lombardo et al., 2012). In 326 B.C. the city was conquered by the Romans and, during the III and IV century A.D., the Christian religion became popular with its inhabitants. With the diffusion of Christianity, the construction of the most important and well-maintained catacombs, built by digging the Neapolitan Yellow Tuff, started. During its Roman phase, the city developed near the sea, to gain easier access to the port, at west toward *Miseno* and at east where the city of *Ercolano* is located. With the fall of the western Roman Empire, South Italy became part of the Byzantine Empire, although, during the VII century A.D., the area of the city and its immediate vicinity was referred to as the Duchy of Naples, gradually incrementing its autonomy and population starting from the IX century onward. The statute of Duchy was kept until the XII century when it became part of the Angevine Kingdom of Sicily until the XIII century, when a Sicilian revolt (War of the Sicilian Vespers) divided the Kingdom of Sicily in Kingdom of Naples and Kingdom of Sicily proper. Decades of independent government and foreign rule (mostly French and Spanish, but also Austrian) followed one another until the XIX century when the Kingdom of Two Sicilies was formed. The city kept growing until the development of new buildings outside the walls was stopped around the middle of the XVI century A.D. (De

Seta, 1999) and started again during the XVIII century (Figure 4.2). Even after the Italian Unification (1861), when the city lost its status as a European capital, its population and density kept growing (Mazzeo, 2009) well beyond the limits of the medieval walls not only during the post-unification period but also during the fascist regime and the second post-war period (Pacione, 1987). In 1995, part of the historical city was added to the list of UNESCO World Heritage sites due to being able to keep and preserve its history and culture through the centuries (https://whc.unesco.org/en/list/726/).

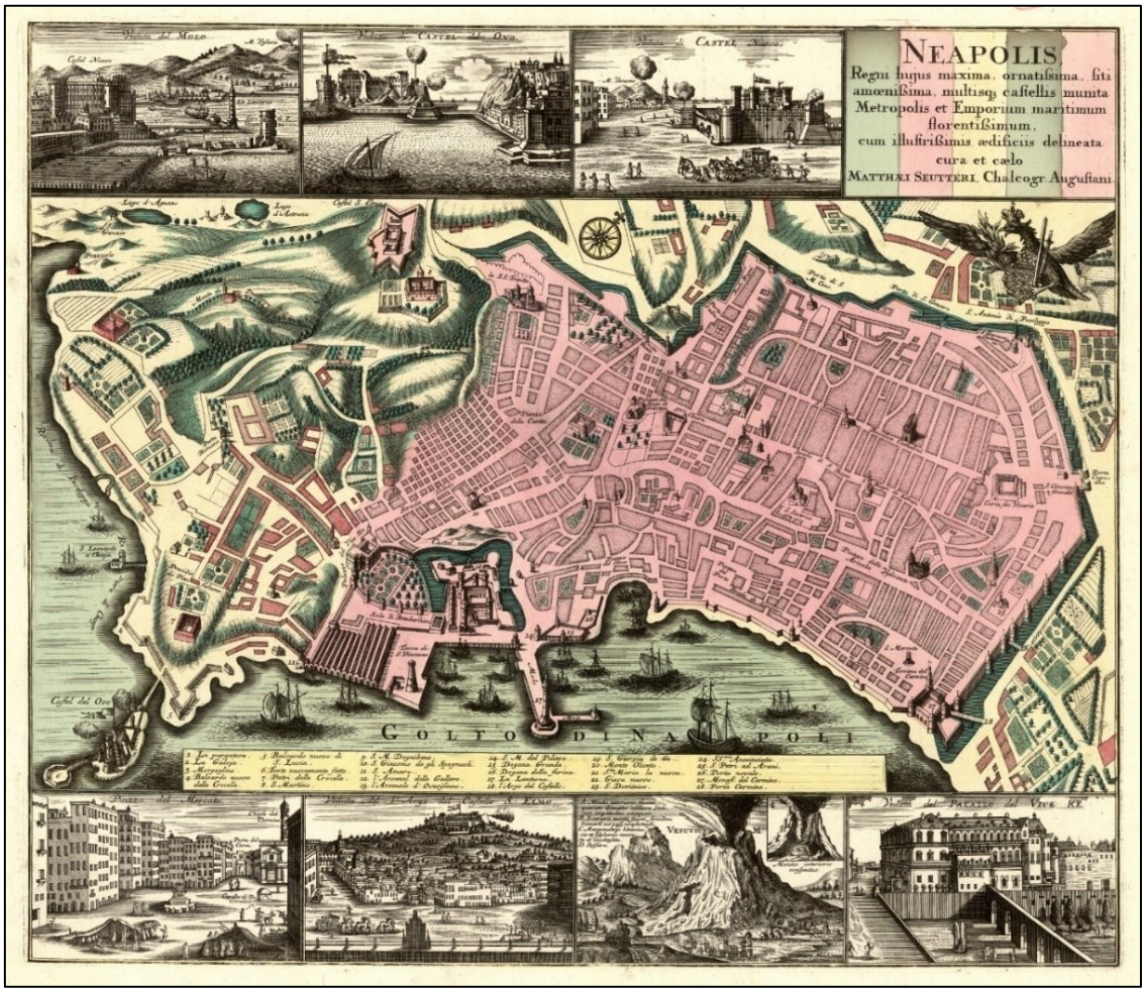

Figure 4.2: Map of the City of Naples by Seutter Matthäus (between 1730 and 1760), (Bernard Pavel Moll's Collection, Moravian Museum).

4.1. Geomorphology and hydrogeology

The Neapolitan landscape is characterized by the presence of alluvial plains, hills around the city centre (Figure 4.3), and the Phlegrean Fields (Figure 4.4). The two alluvial-coastal plains are located in the eastern sector of the city and the western one (*Bagnoli – Fuorigrotta*) (Ascione et al., 2021). The eastern alluvial plain is related to the Sebeto River which flowed until the 20th century (Ducci and Sellerino, 2015). The alluvial plain deposits also contain distal and mid-distal products from the Somma-Vesuvius volcanic complex (Isaia et al., 2018). As for the local hydrology, the Sebeto River is not visible anymore due to the heavy urbanization of the region that reduced the river discharge until it disappeared in the twentieth century (Brandolini et al., 2020). Overexploitation due to increased population and industrialization severely lowered the water table and caused a deterioration in water quality, forcing the population to abandon some of the wells in the *Ponticelli* neighbourhood (Allocca et al., 2022). At the beginning of the 1990s, when the exploitation became less severe, the water table rose again and structures built during the previous decades suffered from groundwater flooding (Ducci and Sellerino, 2015; Allocca et al., 2022).

On the other side of the city, the *Bagnoli – Fuorigrotta* plain development was strictly related to the Phlegrean Fields. On the continent, the volcanic field is centred on the area of *Pozzuoli* city (Figure 4.4) and include the western sector of the city of Naples, in particular, the entirety of the neighbourhoods of *Pianura*, *Soccavo*, *Bagnoli* and *Fuorigrotta*. After the Campanian Ignimbrite eruption that caused the collapse of the caldera (Rosi et al., 1983; Sbrana et al., 2021), the plain settled undersea and it emerged during the Late Pleistocene (Santangelo et al., 2017). There are traces of a paleo-cliff, 2-m high at most, between the Fuorigrotta neighbourhood and the coastal section of the plain (Calderoni and Russo, 1998; Russo et al., 1998).

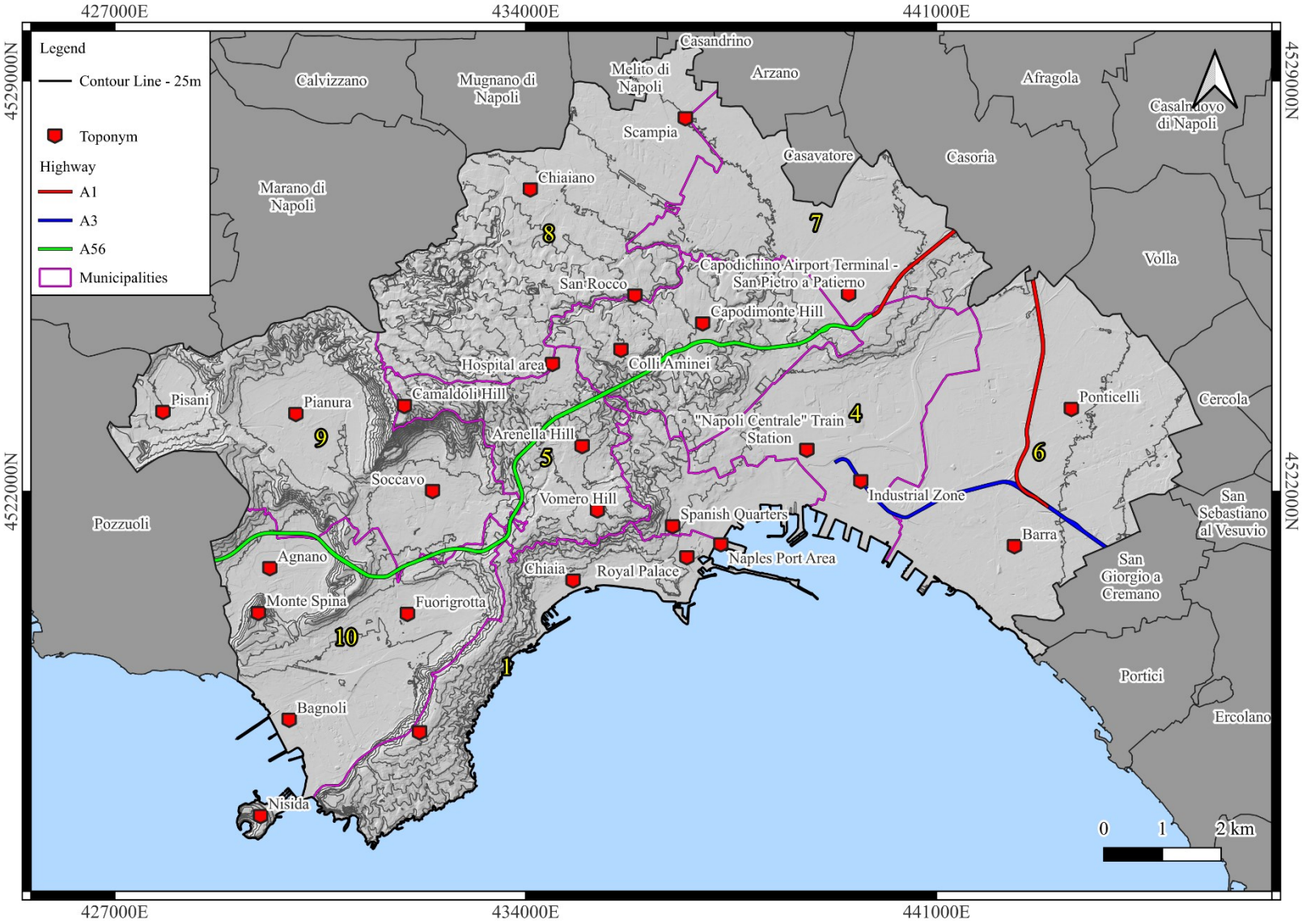

Figure 4.3: City of Naples map with main toponyms, highways and municipalities boundaries. The municipalities are numbered from 1 to 10.

The only stream in the area was the *Arena S. Antonio* which reached the sea directly through the *Bagnoli* neighbourhood. Nowadays, it is a buried stream, flowing underneath the road network (Russo et al., 1998). The *Pozzuoli*, *Camaldoli*, *Vomero*, and *Arenella* hills are the limits of the caldera within the city of Naples. These hills usually have gentle slopes outside of the caldera, with well-developed hydrographical networks and deeply incised valleys (Ascione et al., 2021). The inner slopes of the caldera boundaries are steeper and prone to landslides (Calcaterra et al., 2007). Hydrography is characterized by a radial-centrifugal pattern and the beds of the streams are, often, buried by roads or urban fabric which represents a huge risk in case of exceptional meteorological events (Ascione et al., 2021). Inside the caldera, there are traces of older volcanic edifices and crater rims like *Monte Nuovo*, *Agnano*, and the *Averno* Lake to name a few. Groundwater flow is characterized by overlapping aquifers that are denoted by independent recharge from the adjoining aquifers due to the varying stratigraphy caused by the complex eruption history. In the portion belonging to the Neapolitan city area, the groundwater flows prefer a direct path towards the coastline (Celico, 1983).

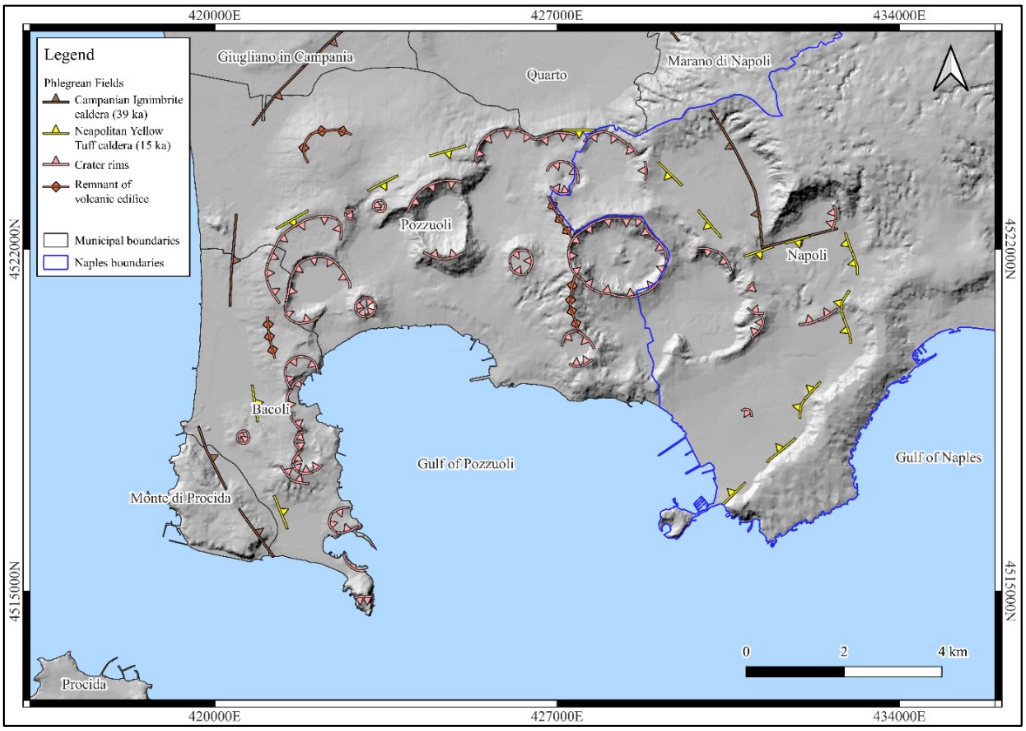

Figure 4.4: Borders of the two caldera of the Phlegrean Fields and volcanic edifices (modified from Wohletz et al., 1999; Costa et al., 2022).

4.2. Geological setting

The city of Naples is located in the southern area of the Campanian Plain. Its western sector is part of the Phlegrean Fields, an active volcanic field, while the eastern sector is part of the alluvial plain where the Sebeto River flowed. It borders, to the north, with the remaining part of the Campania plain, to the west with the aforementioned Phlegrean Fields, to the east with the Somma-Vesuvius volcanic complex and it is bathed, to the south, by the sea (Gulf of Naples). The Campanian Plain is the result of an extensional tectonic phase that involved the Apennines fold and thrust belt during the Pleistocene (Cinque et al., 2000; Santangelo et al., 2017; Vitale and Ciarcia, 2013; 2018). The Apennines themselves are the product of the subduction of the African plate under the European one with an eastward migration of the front that involved the Adria plate (Dewey et al., 1989; Vitale and Ciarcia, 2013; 2018). Different models have been proposed during the years (Ippolito et al., 1975; Merlini and Mostardini, 1986; Cello and Mazzoli, 1998) but, in general, the orogenic process involved Mesozoic platforms and basins (from West to East: Ligurian Basin; Apennine Platform; Lagonegro-Molise Basin and the Apulian Platform) (Figure 4.5). As shown in Figure 4.6, the area of the city of Naples is mainly characterised by volcanic products from the Quaternary alluvial and volcanic deposits that filled the Campanian Plain depression (Aprile et al., 2004; Santangelo et al., 2010). These deposits are part of the Ischian-Phlegrean supersynthem which is made up of all the deposits that fill the graben of the Campanian Plain. The supersynthem lower boundaries are the sin-graben deposits, while the erosional surface (outside of the Phlegrean caldera) and the tectonic limits (inside the caldera) related to the Campanian Ignimbrite are the upper boundaries. The description of the following lithologies is based on the official national geology CARG map (*Carta Geologica d'Italia* – Italian Geological Map) from ISPRA (*Istituto Italiano di per la Protezione e Ricerca Ambientale* – Italian National Institute for Environmental

Protection and Research) (*Servizio Geologico d'Italia*, 2015; Isaia et al., 2018). The CARG map has also been used as one of the predisposing factor in the following analysis.

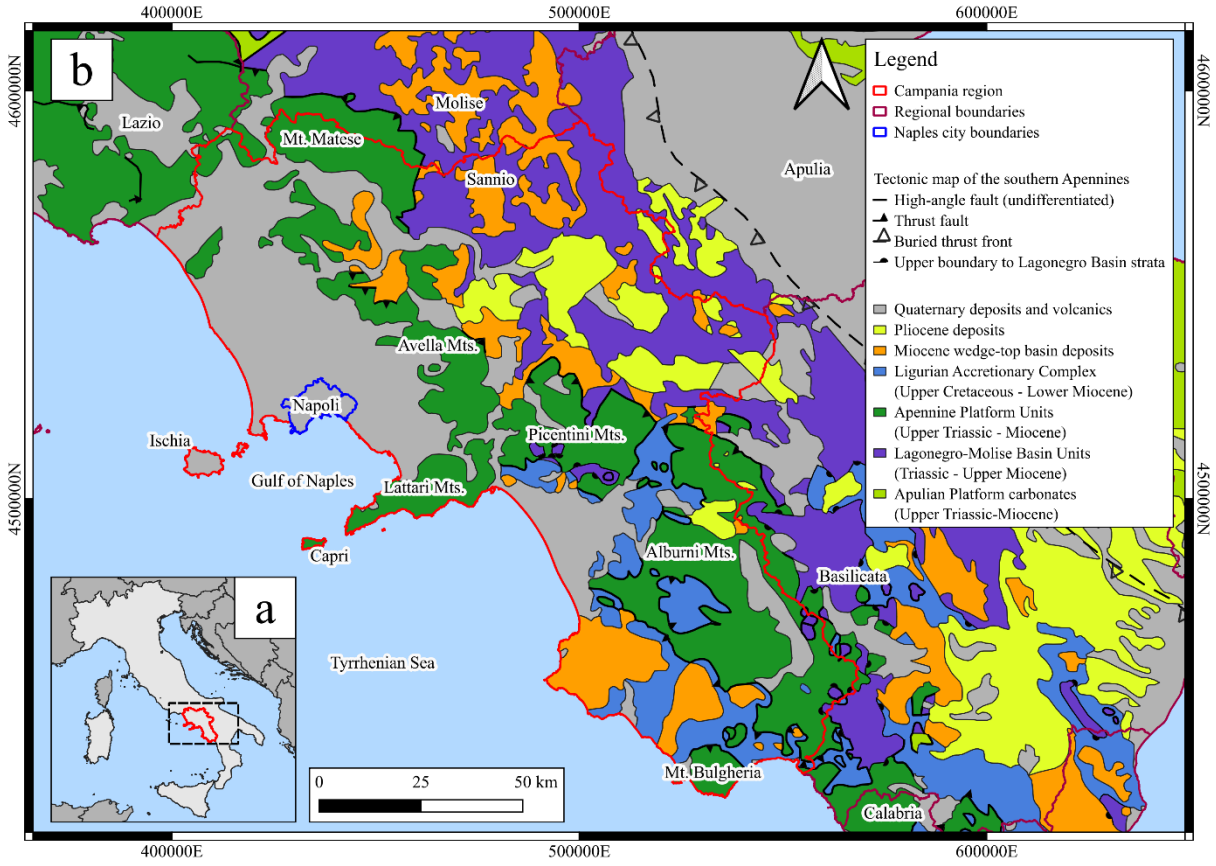

Figure 4.5: a) Location of the Campania region and b) tectonic map of the Southern Apennines (modified from Vitale and Ciarcia, 2013).

As already stated, the Ischian-Phlegrean supersynthem is made up of the deposits that fill the Campanian Plain graben. These are mainly volcanic and sedimentary deposits. The *Tufi di Castel dell'Ovo – Castel dell'Ovo* tuffs (OVO) (Upper Pleistocene) (Figure 4.6), which are one of these volcanic deposits, are also part of the *Quarto* synthem (within the Ischian-Phlegrean supersynthem) which includes the products of the volcanoes of the Phlegrean Fields area before the Campanian Ignimbrite eruption (older than ~39 ka BP). OVO is made of yellow to brown tuffs characterized by fine grain and a dense stratification with black scoriae and lithic fragments. The Explanatory Notes of the map (Isaia et al., 2018) refer to one of the lower units of the succession when citing the age of the OVO tuffs as ~78.3 ka PB (Scarpati et al., 2013).

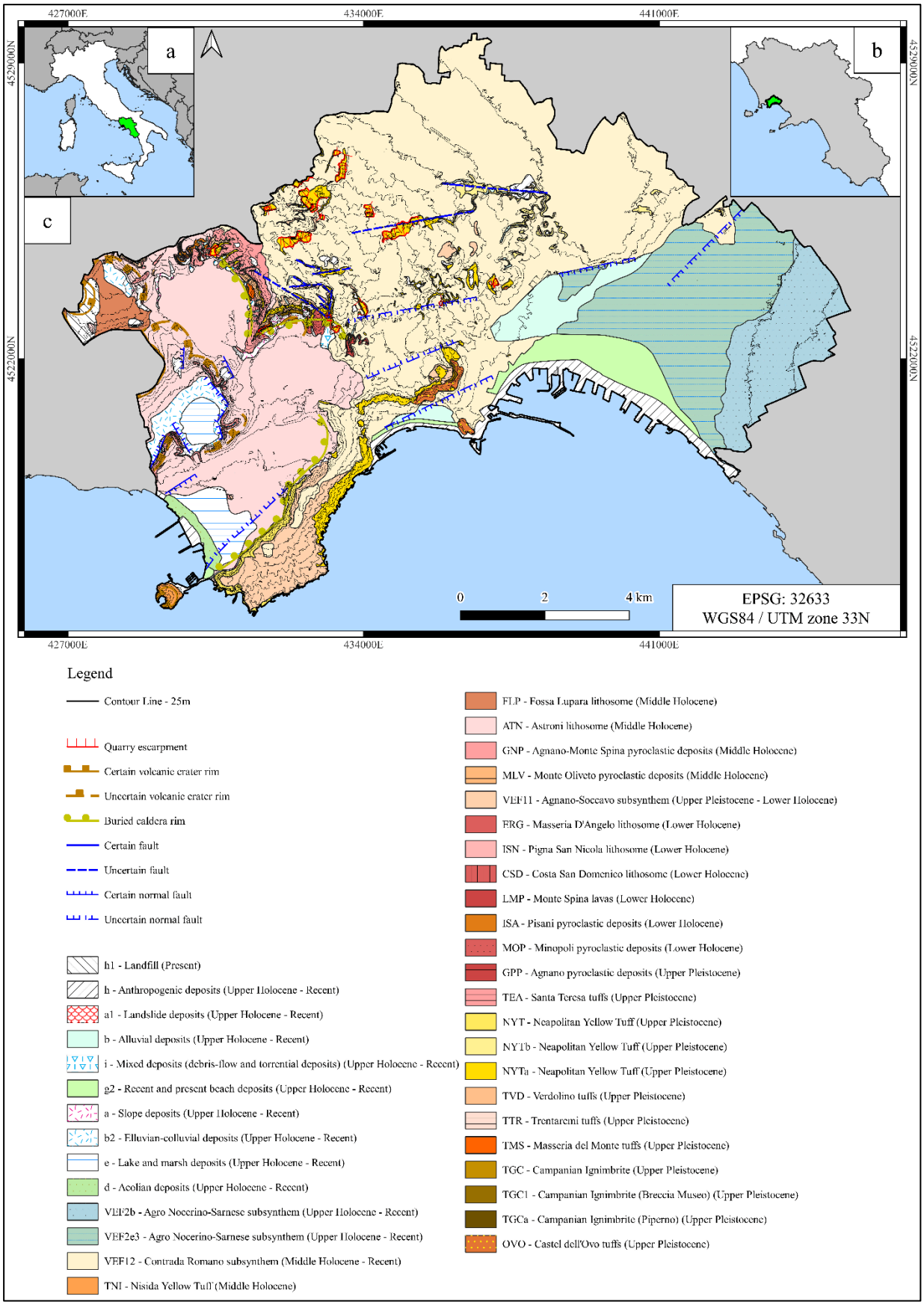

Figure 4.6: Location of the Campania region (a) and the city of Naples (b) related to, respectively, Italy and Campania; c) Geological map of the city of Naples (modified from project CARG, Servizio Geologico d'Italia, *2015).*

The *Tufo Grigio Campano* (Campanian Grey Tuff), also called *Ignimbrite Campana* (Campanian Ignimbrite), (TGC) (Upper Pleistocene) is the product of the most important volcanic event of the Phlegrean Fields, dated ~39 ka BP (De Vivo et al., 2001) and its top represent the upper limits of the Ischian-Phlegrean supersynthem. The TGC is a welded to loosely welded tuff from a trachytic magma erupted from a phreatomagmatic explosion that produced a volume of over 310 km^3 of Campanian Ignimbrite (Rolandi et al., 2003). Perrotta et al. (2006) recognize five separate units in the TGC: i) the lowermost unit is a pink to brown, to grey stratified and incoherent ash deposit with grey pumice lapilli; ii) the second unit is known as the Piperno (TGC_a) characterized by a lithified grey ashy matrix with dispersed flattened juvenile fiamme. The height-to-width ratio of these fiamme can vary from 1:3 to 1:7 (Perrotta et al., 2006); iii) above the *Piperno*, separated by erosive surfaces, the Breccia Museo (TGC_1), can be found. It is a coarse clast-supported breccia deposit full of heterogenous lithic clasts varying from trachytic lavas to volcanic glass and tuff fragments; iv) a laterally discontinuous deposit characterized by spatter clasts and a fine matrix; v) a reddish fine to coarse ash deposit with grey scoriae clasts, obsidians and pumices. The *Piperno* unit too, just like the Neapolitan Yellow Tuff, has been largely used in Neapolitan architecture as a decorative stone (Calcaterra et al., 2000; 2005; Cennamo et al., 2016).

Above the Campanian Ignimbrite starts the Pianura subsynthem (VEF9) (Figure 4.6). The *Tufi di Masseria del Monte* – Masseria del Monte Tuffs (TMS) (Upper Pleistocene), *Tufi di Trentaremi* – Trentaremi Tuffs (TTR) (Upper Pleistocene) and the *Tufi del Verdolino* – Verdolino Tuffs (TVD) (Upper Pleistocene) are part of this subsynthem. The TMS is characterized by laminar flow whitish ash deposits alternated with white to grey pumiceous layers. This is a flow and, subsequently, falls slightly to medium lithified deposits. The TTR succession includes products from different eruptions, separated by erosion surfaces and paleosoils. The succession is made of interbedded layers of cinerites and white pumiceous

layers. TVD is characterized by a yellow to white densely stratified tuff and loose to slightly lithified ash deposits interbedded to grey, discontinuous, grey pumices.

The Neapolitan Yellow Tuff (NYT) (Upper Pleistocene) (Figure 4.7) is included in the *Napoli* subsynthem (VEF_{10}). It is the only unit of the aforementioned subsynthem present in the Naples municipality. There is a vast literature regarding the NYT (Orsi et al., 1992;1995; Cole and Scarpati, 1993; Scarpati et al., 1993; Wohletz et al., 1995; Deino et al., 2004) and it is the product of an eruption dated ~15 ka (Deino et al., 2004; Fedele et al., 2011).

This eruption featured a caldera spanning 90 km^2, with a central portion that subsided by 600 m (Deino et al., 2004). This caldera is located within a previously formed caldera associated with the eruption of the Campanian Ignimbrite. The NYT is made up of two members, a lower (A) and an upper one (B) (Orsi et al., 1992; Cole and Scarpati, 1993; Scarpati et al, 1993). The lower member is composed of six fall deposits and various ash layers. The fall deposits are made of, from base to top, two ash layers (the first one stratified, the second one rich in accretionary lapilli) and four grey pumice lapilli deposits (Scarpati et al., 1993). The upper member is made of proximal pyroclastic flow deposits and distal surge deposits (Orsi et al., 1992) characterized by thicker ash layers with dispersed pumices and localized abundance of lithic fragments, interbedded with stratified and reversely graded layers (Cole and Scarpati; 1993). The subdivision in NYT_a and NYT_b in the official geology map from the *Servizio Geologico d'Italia* is not based on the aforementioned units. The NYT_a are the Neapolitan Yellow Tuff proximal deposits made of yellow, generally lithified, pyroclastic deposits, while the NYT_b represents the distal products that appear greyish and loose (Isaia et al., 2018). The NYT_b is the vertical and lateral variation of the NYT_a. The importance of this deposit as a building stone in the city of Naples is well documented (Colella et al., 2001; 2017; Di Benedetto et al., 2015; Heap et al., 2018) and the underground extraction of the NYT has led to the creation of a significant underground cavity system beneath the city.

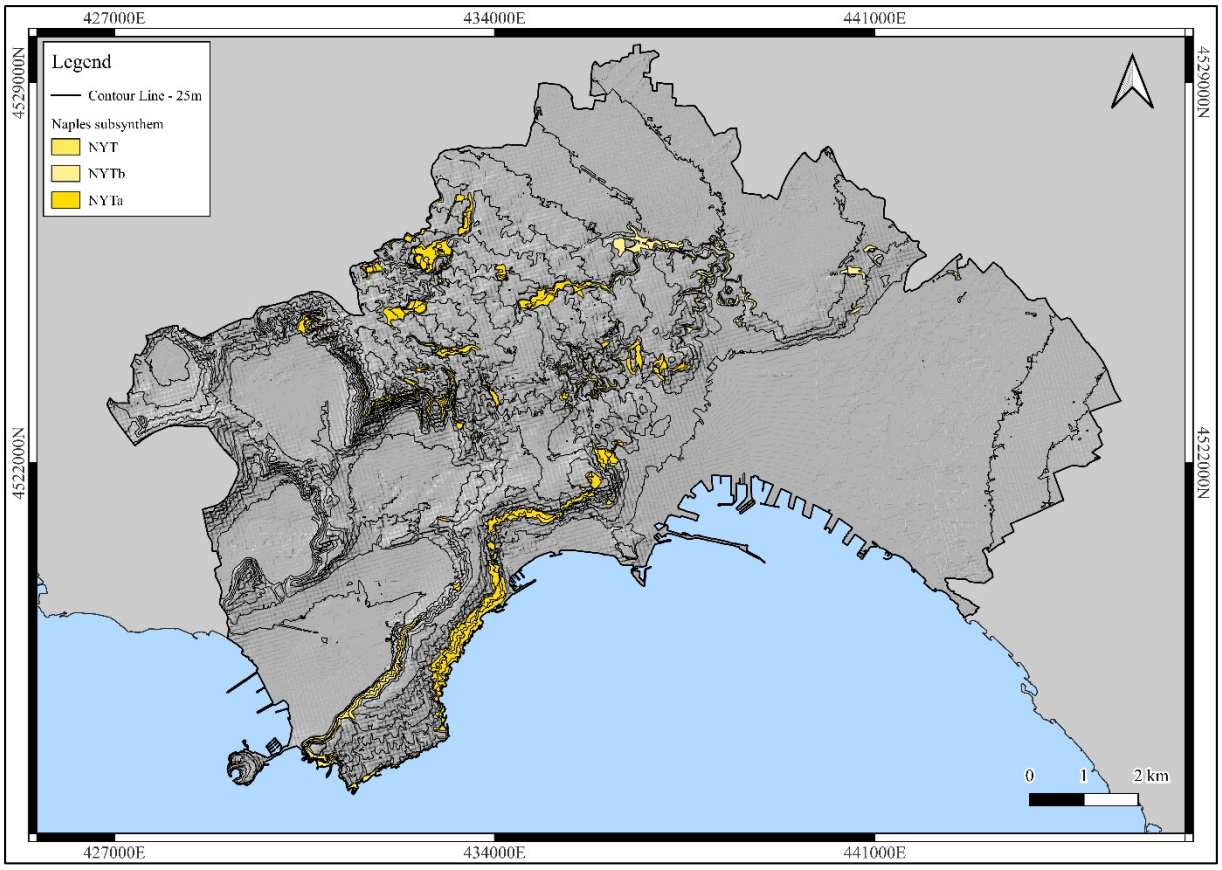

Figure 4.7: Napoli *subsynthem (modified from project CARG,* Servizio Geologico d'Italia*, 2015).*

The *Agnano-Soccavo* (VEF_{11}) subsynthem (Figure 4.8) (Upper Pleistocene – Lower Holocene) is made of volcanic products younger than the NYT and is, stratigraphically, separated from the overlying *Contrada Romano* subsynthem by a thick paleosoil. These deposits are mainly constituted by fine to coarse ashes with pumiceous lapilli and black scoriae. The units are separated by paleosoils, continental non-volcanic deposits and erosion surfaces (Isaia et al., 2018). The older unit related to the *Agnano-Soccavo* (VEF_{11}) (Figure 4.7) subsynthem in the study area is the *Santa Teresa* Tuff (TEA) (Upper Pleistocene), a completely zeolitized sequence of pyroclastic deposits. The TEA is characterized by coarse to fine ash layers with black scoriaes, brown pumices and volcanic glass.

The following *Agnano* (GPP) (Lower Holocene) *Minopoli* (MOP) (Lower Holocene) and *Pisani* (ISA) (Figure 4.8) (Upper Pleistocene) pyroclastic deposits are dated from 9.5 ka (ISA) to 10.3 ka (GPP) (Di Vito et al., 1999).

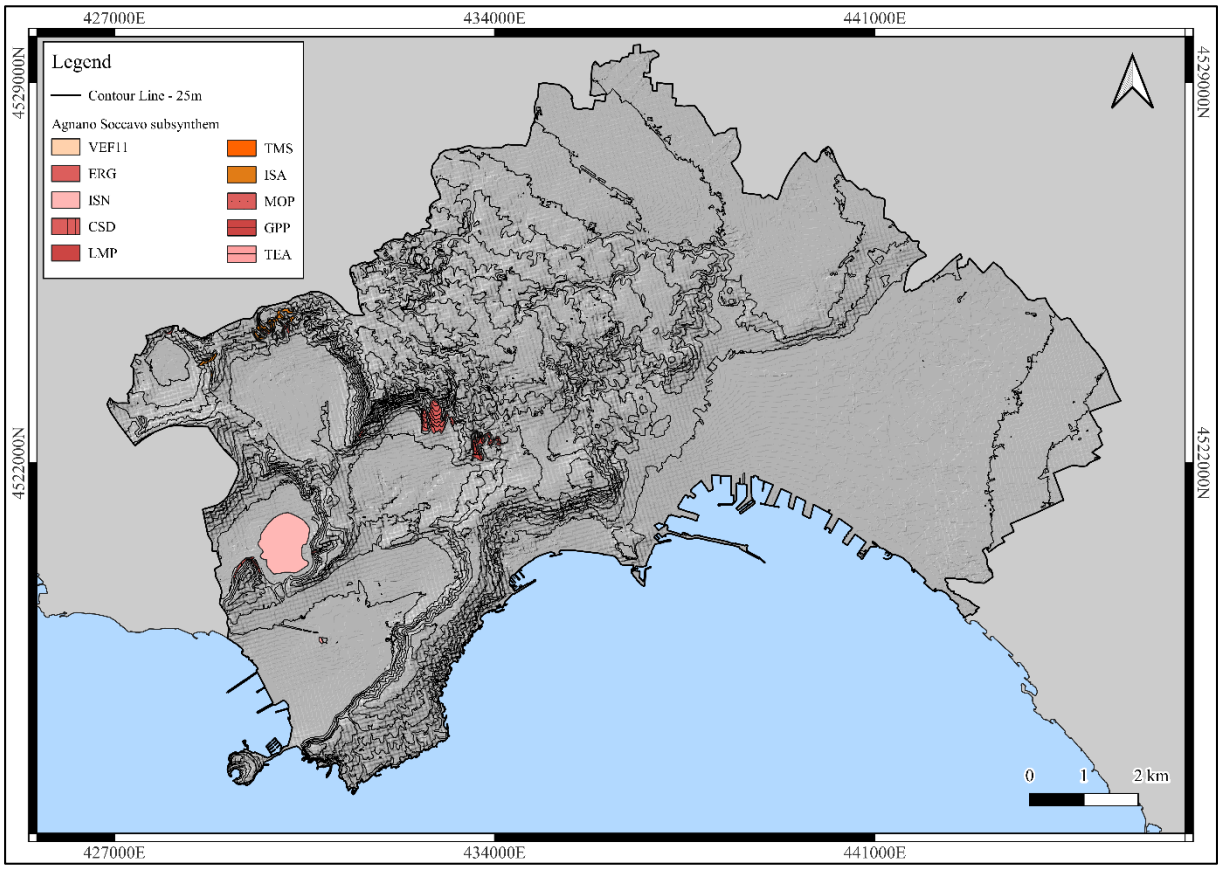

Figure 4.8: Agnano-Soccavo subsynthem (modified from project CARG, Servizio Geologico d'Italia*, 2015).*

All three are complex pyroclastic deposits separated by erosional surfaces or paleosoils. These three deposits include other less extensive pyroclastic deposits, as described in the Explanatory Notes of the Geological Sheet n°446-447 *Napoli* (Isaia et al., 2018). The *Agnano* pyroclastic deposit is made up of an alternation of grey-pinkish pumiceous and lithic clasts layers and cinerites layers with accretionary lapilli, pumices and lithic clasts. GPP deposits also include a distinctive violet sand layer. The *Minopoli* pyroclastic deposits are characterized by thick scoriae layers and thin grey-yellow cinerite layers with accretionary lapilli, scoriaes and lithic clasts. The *Pisani* pyroclastic deposits are characterized by interbedded coarse to fine

layers. The coarse layers are more frequent towards the base and are made of dark grey to black scoria, pumice and volcanic glass. Towards the top, the finer layers are made of compacted ashes.

In the area of *Monte Spina* outcrops a dark grey, very altered, lathitic-trachytic lava fractured and locally brecciated called *Monte Spina* lava (LMP) (Lower Holocene). It represents the remains of a relict dome. The *Costa San Domenico* lithosome (CSD) (Lower Holocene) is, instead, characterized by grey-green to yellow cinerites with varying granulometry from fine to coarse and accretionary lapilli and dark grey to pink pumiceous layers. There is presence of grey tuffs and lavas clasts and red to orange igneous clasts that underwent hydrothermal processes. The age, obtained with carbon dating analysis, is ~8.6 ka (Scandone et al., 1991) and is separated from the Pigna San Nicola lithosome (ISN) (Lower Holocene), ~8.2 ka (Scandone et al., 1991), by a thick paleosoil. ISN is a surge and, subsequentially, fall deposit made of cinerites with varying granulometry from fine to coarse alternated to pumiceous lapillus layers. The *Masseria D'Angelo* (ERG) lithosome is characterized by fall cinerite layers with accretionary lapilli and coarse pumices layers. Lava or tuff lithic fragments are present. Carbon age analysis date ERG at ~8.2 ka (Di Vito et al., 1999) (Lower Holocene).

The *Contrada Romano* subsynthem (VEF_{12}) (Middle Holocene – Recent) (Figure 4.9) comprehends mostly stratified cinerite deposits from the Phlegrean Fields (from 5.5 ka BP to the last one of Monte Nuovo in 1538). Paleosoils or erosion surfaces are often found between the pyroclastic deposits while lavas outcrops are less widespread (Isaia et al., 2018). The *Monte Oliveto* (MLV) lithosome and the *Agnano-Monte Spina* (GNP) lithosome are both surge and fall pyroclastic deposits with varying granulometry from fine to coarse. In the MLV the ash layers characterized by finer granulometry show a yellow to violet colour and contain accretionary lapilli. The alternating coarse pumice layers can also contain lithic clasts that underwent hydrothermal processes. The pyroclastic deposits are separated by thin paleosoil

layers. This is because, as specified in the *Note Illustrative* (Isaia et al., 2018), this is a complex deposit made of different products of different eruptions gathered under together under the *Monte Oliveto* pyroclastic deposits. The carbon dating analysis ages vary from ~4.8 to ~4.1 ka BP (Fedele et al., 2011) (Upper Pleistocene – Lower Holocene). In the GNP the ashes' colour varies from grey to red-purple and there is the presence of accretionary lapilli and pumices, scoriaes, obsidians and tuffaceous and igneous clasts that underwent hydrothermal processes in coarser layers. $^{40}Ar/^{39}Ar$ age analysis (Fedele et al., 2011) and radiocarbon age analysis (De Vita et al., 1999) date the GNP at circa 4.1 ka BP.

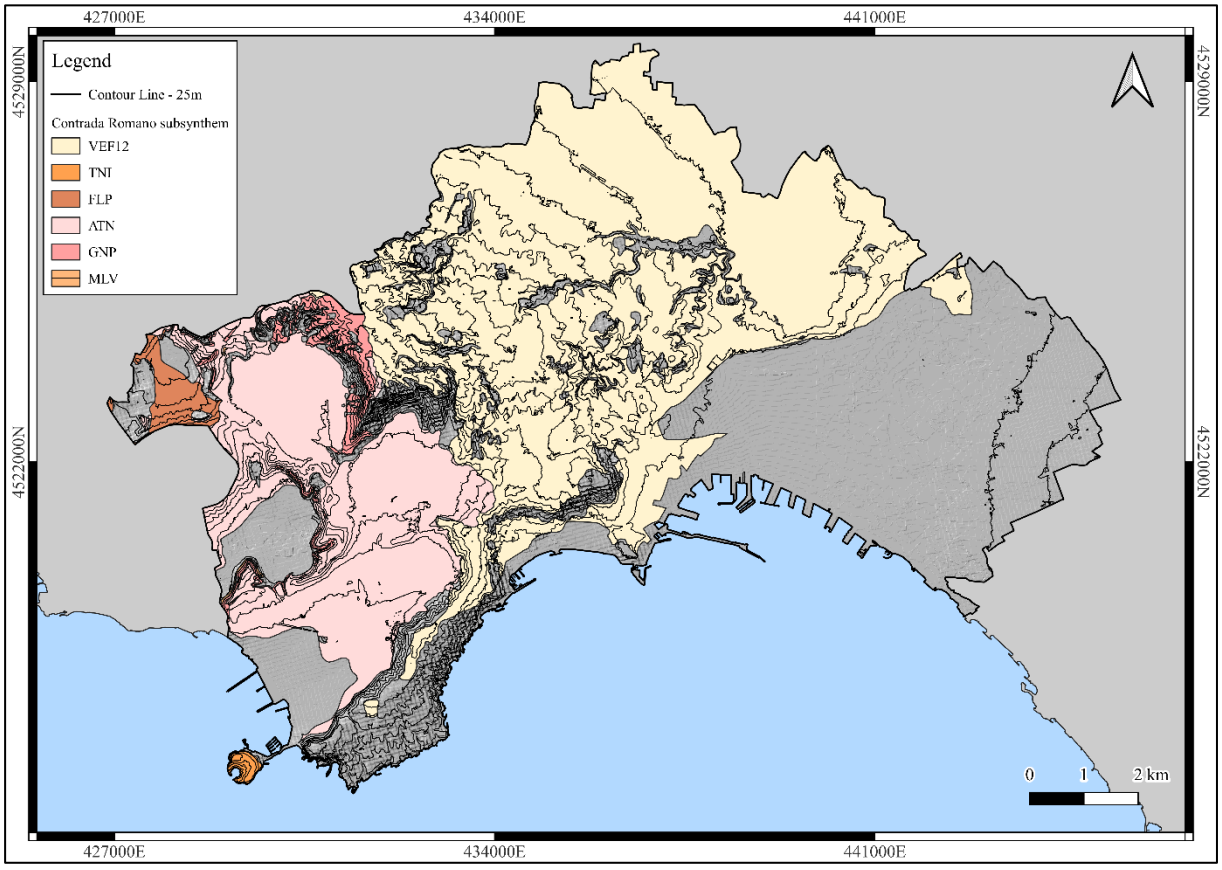

Figure 4.9: Contrada Romano subsynthem (modified from project CARG, Servizio Geologico d'Italia*, 2015).*

The *Astroni* lithosome (ATN) and the *Fossa Lupara* lithosome (FLP) are both dated 3.8 ka BP (radiocarbon age analysis) (Isaia et al., 2009; Fedele et al., 2011). The first one(ATN) is characterized by an alternation of pyroclastic deposits (grey ashes with a varying granulometry

from fine to coarse) and paleosoils, while the latter (FLP) is made of grey to purple ashes layers with a varying granulometry from fine to coarse deposited after the pyroclastic flow. The Nisida Tuffs (TNI), radiocarbon age ~ 3.9 ka BP (Fedele et al., 2011; Scarpati et al., 2013), are made of two lithotypes with the first one being characterized by yellow tuffs with pumices and igneous lapillus in a cinerite matrix and the second one is a stratified, grey, pozzolana.

In the eastern section of the city is located the *Agro Nocerino-Sarnese* subsynthem (Upper Holocene - Recent) (Figure 4.10). It is made up of distal and mid-distal products of the Somma-Vesuvius volcanic complex and fluvial floodplain deposits (VEF_{2b}) or distal and mid-distal pyroclastic deposits and sandy silt interbedded to peaty swamp deposits and clayey silt deposits with sand marine sediments intercalation (VEF_{2e3}) (Isaia et al., 2018).

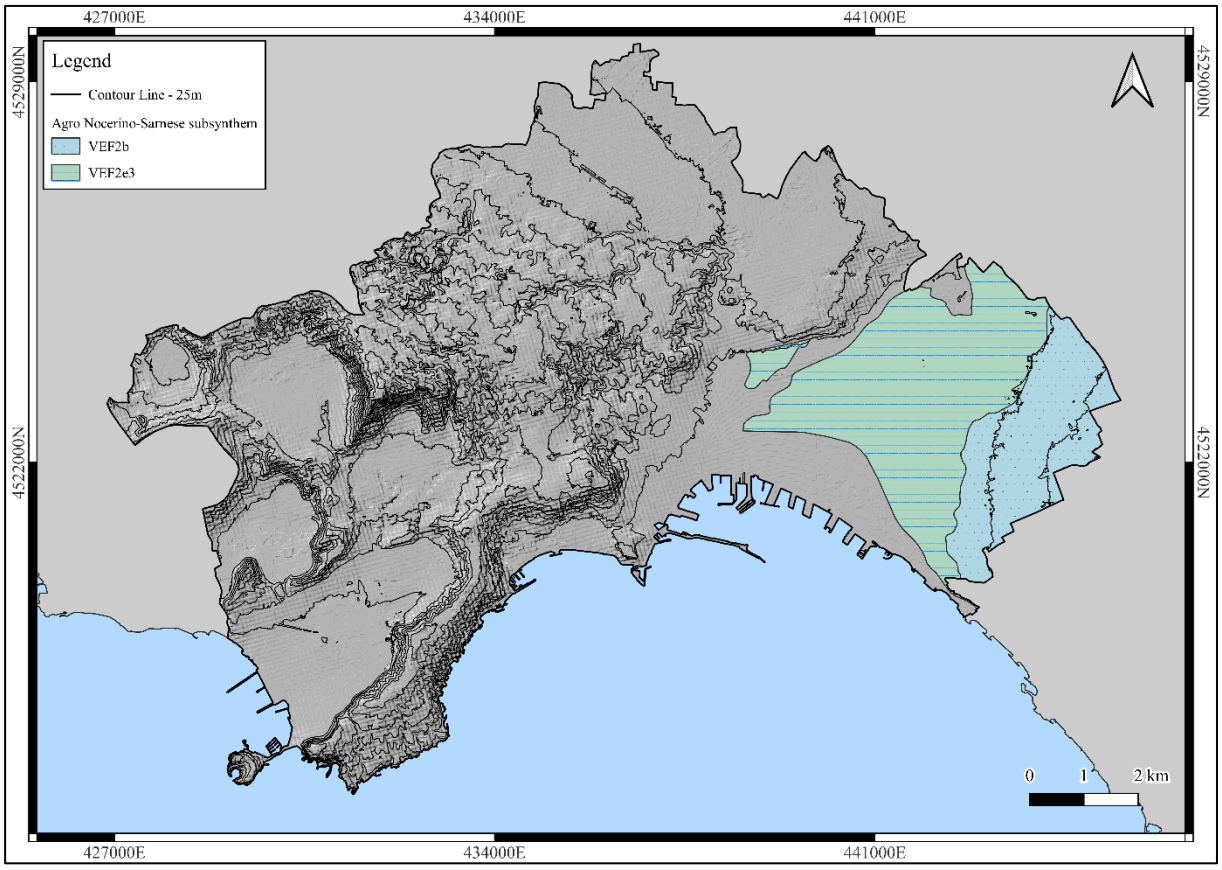

Figure 4.10: Agro Nocerino-Sarnese subsynthem (modified from project CARG, Servizio Geologico d'Italia*, 2015).*

At last, the following deposits are the most recent one and consist of "Recent" and "Upper Holocene – Recent" deposits both of anthropic or natural origin. The anthropic deposits are made up of coastal erosion structures or industrial and extractive activities deposits (h) and landfills and inert construction waste (h_1) (Isaia et al., 2018). The natural deposits are related to (a) heterometric slope deposits characterized by a fine to coarse granulometry with a silty-clay or sand matrix and, occasionally, lava or tuffs boulders, (a_1) landslide deposits made up of clast-supported and/or matrix-supported heterogenic slope materials (tuffs, pyroclastic deposits), (b) alluvial deposits composed of clasts (mainly tuffs) in a torrential deposits matrix, (b_2) elluvian-colluvial deposits from tuffs and pyroclastic deposits alteration, (d) aeolian deposits related to lake and lagoon dune system, (e) sandy silt alternated to peaty swamp deposits and clayey silt lagoon or lake deposits with sand marine sediments intercalation, (g_2) beach deposits with varying granulometry from sand up to sandy gravel, and (i) debris-flow and torrential deposits that vary from sandy and silty matrix uniform deposits to laminar deposits made up of a sandy or silty sandy matrix and tuffaceous clasts.

The landslide frequency in the varying geological units and subsynthems is shown in the following figure (Figure 4.11).

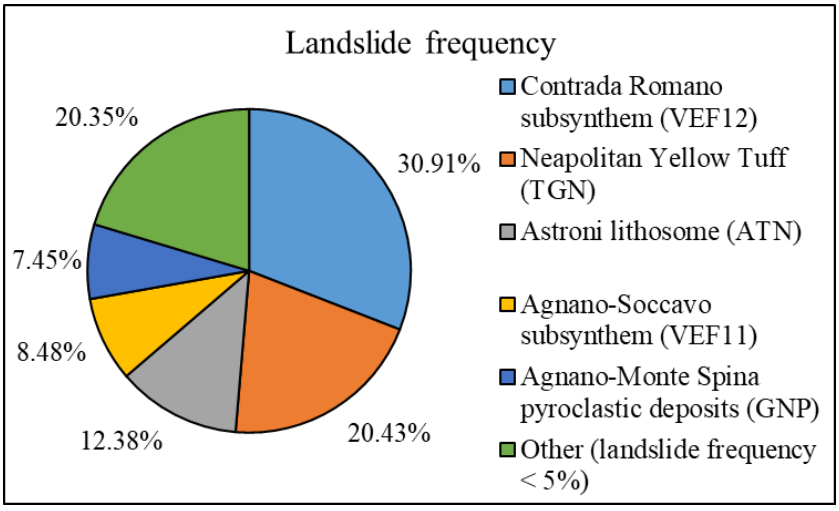

Figure 4.11: Landslide frequency in different units and subsynthems.

5. APPLICATION TO A CASE STUDY RESULTS: THE CITY OF NAPLES

This case study showcased the Risk assessment and the Multirisk approach adopted to characterize the impact of different geohazards on urban areas and on other geohazards. Analyses were performed using a laptop with the following specifications: Intel® i7-10750H CPU @ 2.60GHz, 16 GB of RAM, and NVIDIA GeForce RTX 2060 GPU. The machine uses the Microsoft Windows 11 Home 64-bit operating system.

5.1. Geohazard Inventories update and sampling

The Landslides Inventory used in this project is a subset of the one published by Fusco et al. (2023) (Figure 5.1). The majority of the entries (57.6%) do not show data regarding the date of occurrence, while 9.6% of landslides occurred between 1868 and 1899, 22.6% between 1900 and 1999, and 10.2% between 2000 and 2023. As for the type of movement (Figure 5.2): (i) falls represent 12% of the inventory, (ii) cases where it was not possible to distinguish between falls and topples are 4% of the total, (iii) slides (rotational and translational) consist of 18% of the inventory, (iv) flows represent 28% of the entries, (v) 3% of the data only refers to a general unstable area where one or more types of landslides could occur (Diffuse Shallow Instability Area), (vi) 35% of the entries are undefined. During the first phase of this thesis, the landslides of this inventory were studied and, eventually, updated with new information. This operation was carried out mainly by comparing the information at disposal, such as: (i) year of occurrence, (ii) optical imagery, (iii) lithology, (iv) slope angle, and (v) old aerial photography. After this update (Figure 5.3), all the undefined landslides were associated with a landslide type, and the updated inventory (Figure 5.4) is made of: (i) 13% of fall landslides, (ii) in 16% of the cases it was not possible to distinguish between fall or topple landslides, (iii) 13% of landslides were defined as flow, and (iv) 58% of the landslides fell within the slide type. Undefined and Diffuse Shallow Instability Area landslides were reassigned to different landslide types.

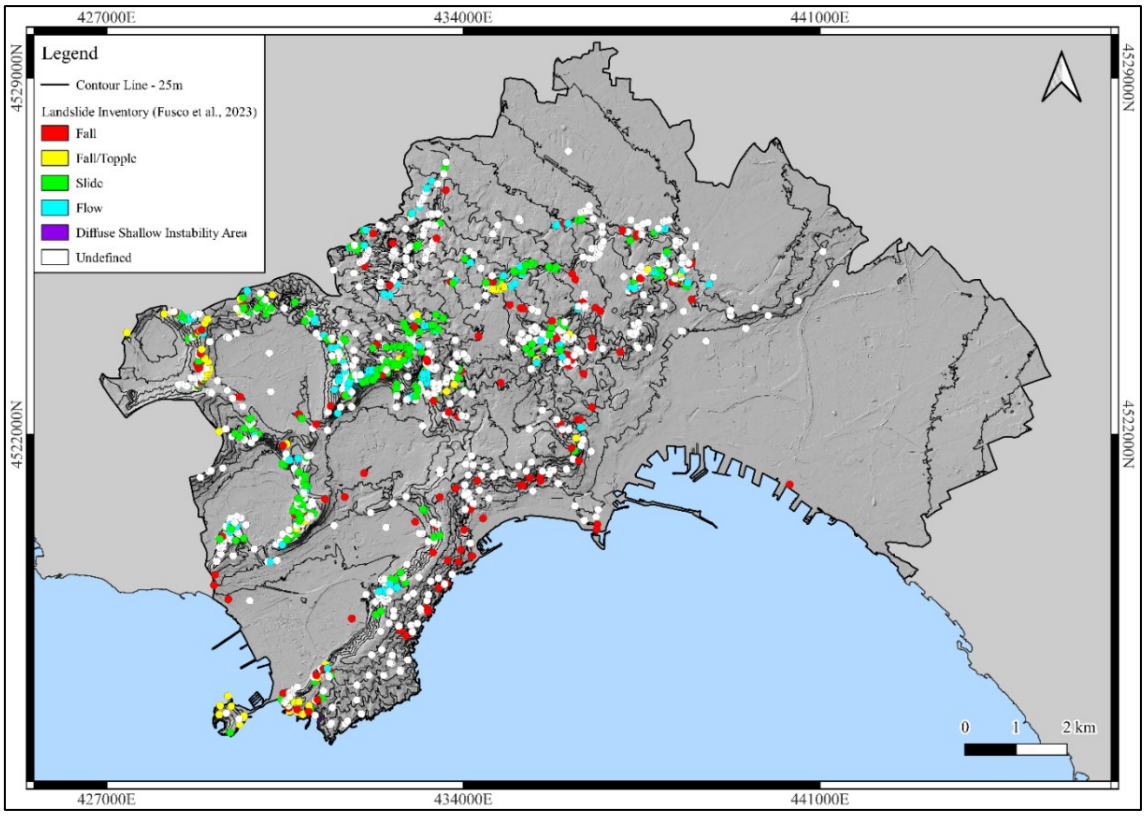

Figure 5.1: Landslide Inventory for the city of Naples (inventory data from Fusco et al., 2023).

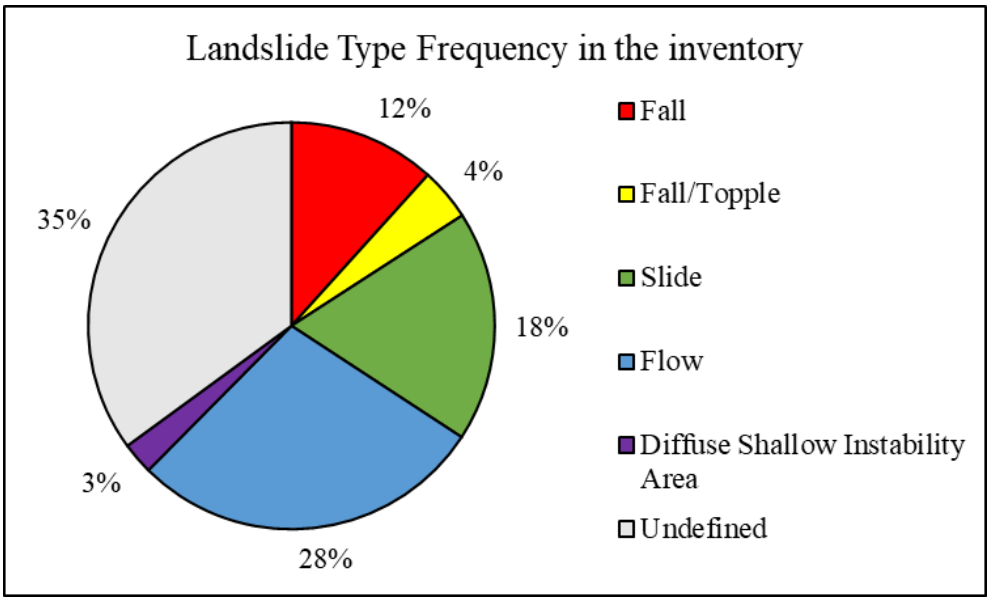

Figure 5.2: Type frequency for the landslide inventory from Fusco et al. (2023).

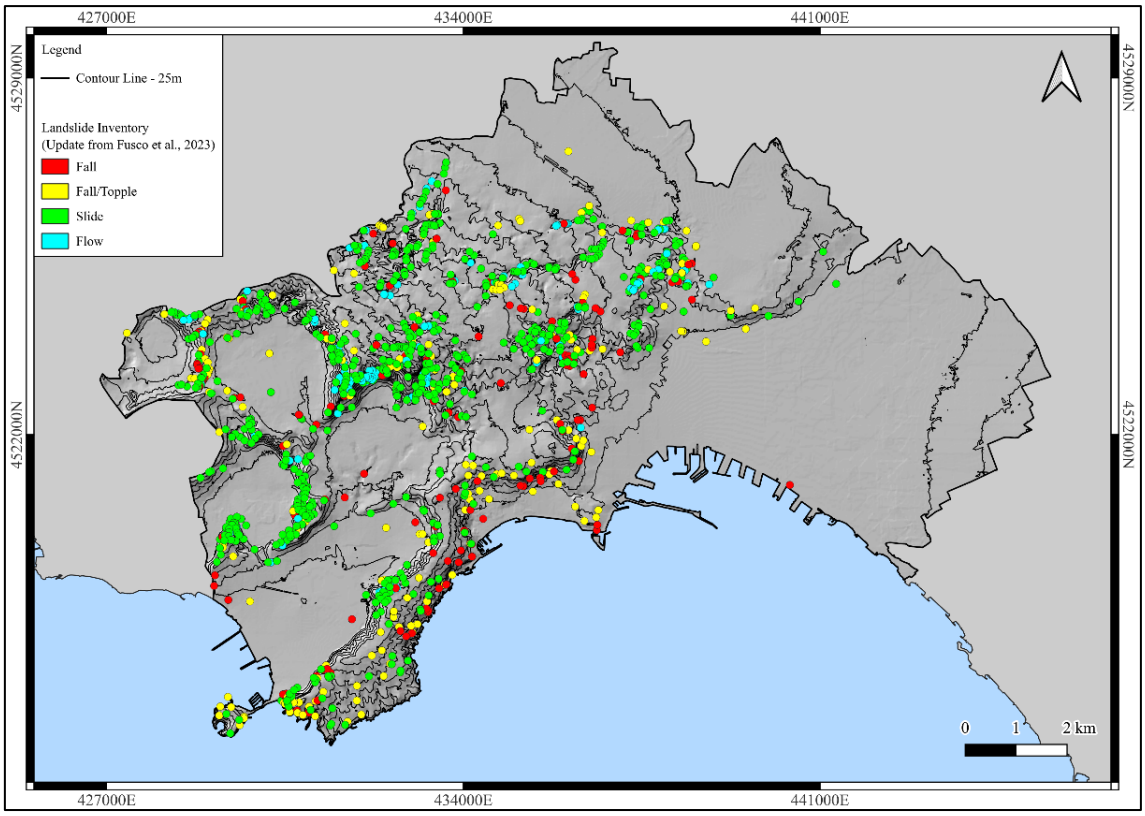

Figure 5.3: Landslide Inventory for the city of Naples (updated inventory data from Fusco et al., 2023).

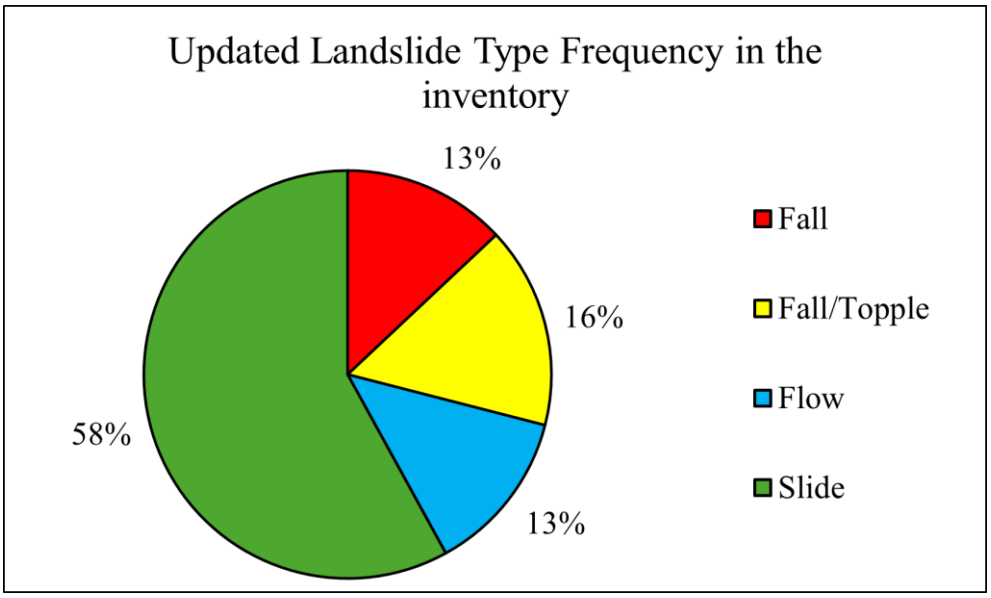

Figure 5.4: Type frequency for the updated landslide inventory.

The anthropogenic sinkhole inventory used as presence points in this study is an updated (up to 2023) version (Figure 5.5) of the inventory published by Tufano et al. (2022). This update was performed using literature data (mainly local and national newspapers, but also city council reports) and fieldwork. The sinkhole inventory published by Tufano et al. (2022) contains 458 entries from 2011 to 2021, circa 268 of which are new addition in relation to the inventory published by Guarino and Nisio (2012). Out of 458 events, the amount of georeferenced sinkholes is 329. The discrepancy between the total amount and the mapped one is due to the lack of information from local and national newspapers, which tend to omit precise geographical details. The sinkhole inventory used in this project consists of 434 mapped sinkholes, a total amount of 105 new events, from June 2021 to May 2023. Around 42% of sinkholes have been triggered by collapse of underground cavities due to material geotechnical properties degradation caused by rainfalls, 15% by leakage of the aqueduct and sewage networks, and 43% have been initiated by an undefined cause (Figure 5.6). Regarding the sinkhole inventory sources, circa 52% of the data was obtained thanks to Local and National News, 6% from city council reports, 4% from field surveys, and 39% from literature (Guarino and Nisio, 2012).

An exhaustive inventory of flooding events in the city of Naples is not available. As the presence data is necessary to assess flood susceptibility through ML algorithms, a sampling of the hazard map provided by the Southern Apennines River Basin District Authority and freely downloadable from their website (https://www.distrettoappenninomeridionale.it/, in Italian) was used. The hazard map used to sample the presence points was produced by the "Unit of Management *Regionale Campania Nord Occidentale*" based on hydrodynamics analysis. Subsequently, as the Southern Apennines River Basin District Authority replaced all the Units of Management of the Campanian Region following the *D.Lgs.* 152/2006 and the *D.M.* n.

294/2016, the hazard map was reclassified following the guidelines from the *D.Lgs.* 49/2010 (Table 5.1).

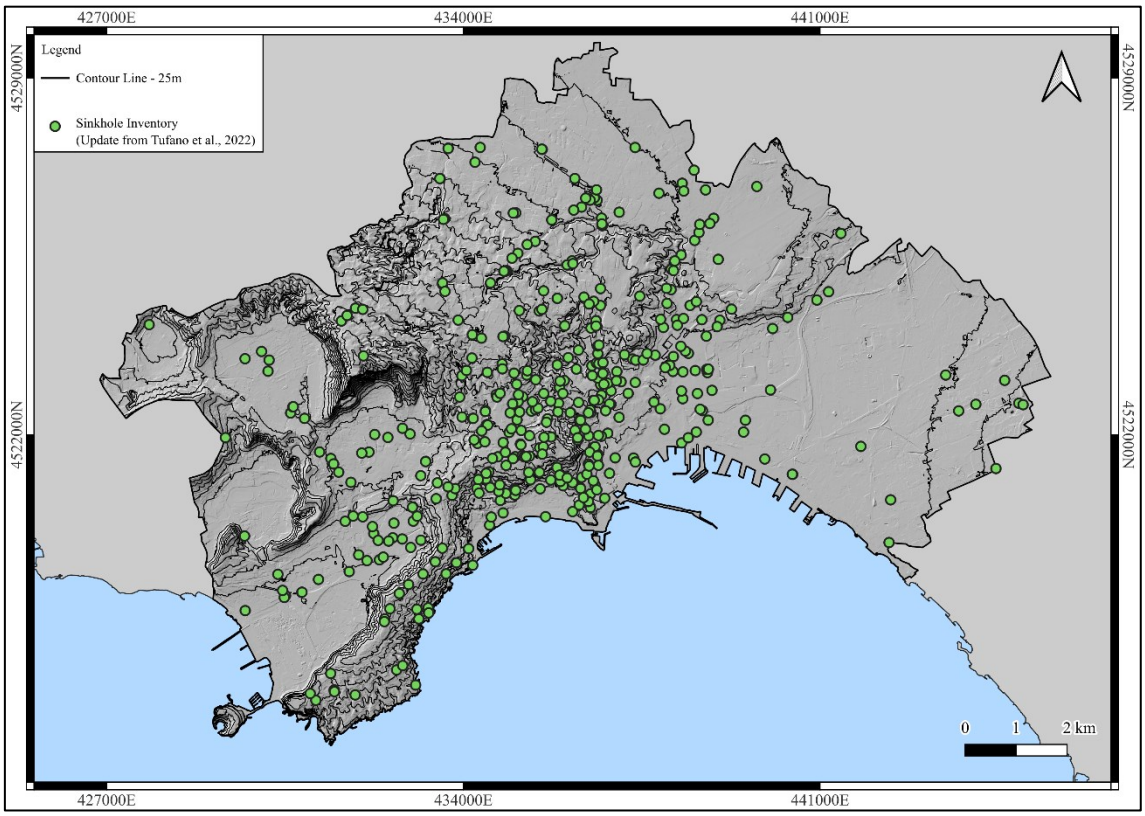

Figure 5.5: Sinkhole Inventory.

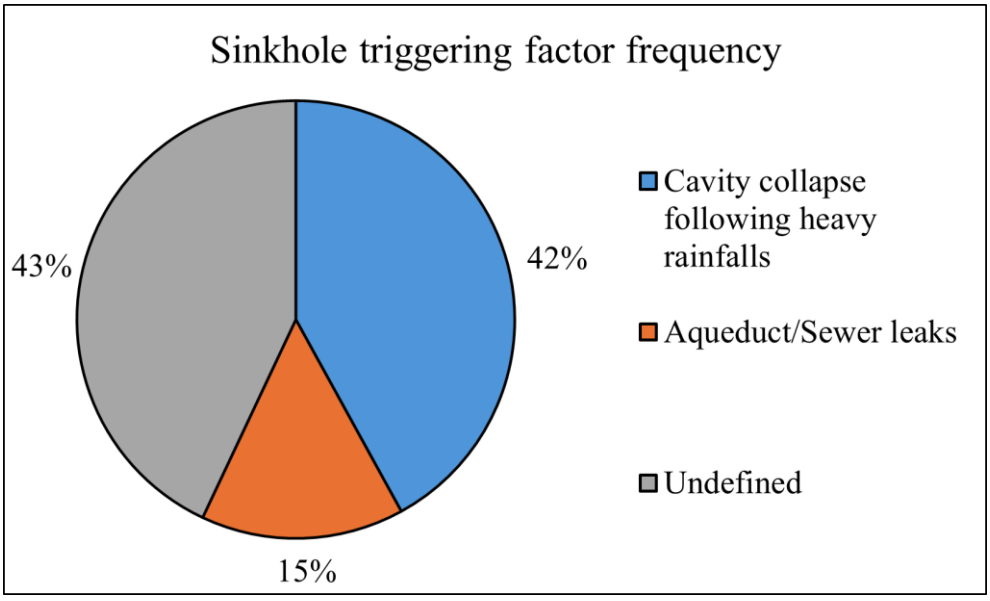

Figure 5.6: Triggering factor frequency in the Sinkhole inventory.

Table 5.1: Flood hazard classes, Southern Apennines River Basin District Authority, D.Lgs. *49/2010.*

Class	Return Period (years)	Flood frequency
P3	20-50	High
P2	100-200	Medium
P1	200-500	Rare

To preserve the flood frequency information which is part of this classification, the number of points extrapolated for every class is proportional to the specific return period of the different classes with a 10:5:1 proportion (P3:P2:P1). This allowed the production of a pseudo-presence inventory (Figure 5.7) of 400 entries (250 for the P3 class, 125 for the P2 class and 25 for the P1 class). A precautionary approach has been employed during the sampling phase, as the proportion is based on the minimum Return Period of every class.

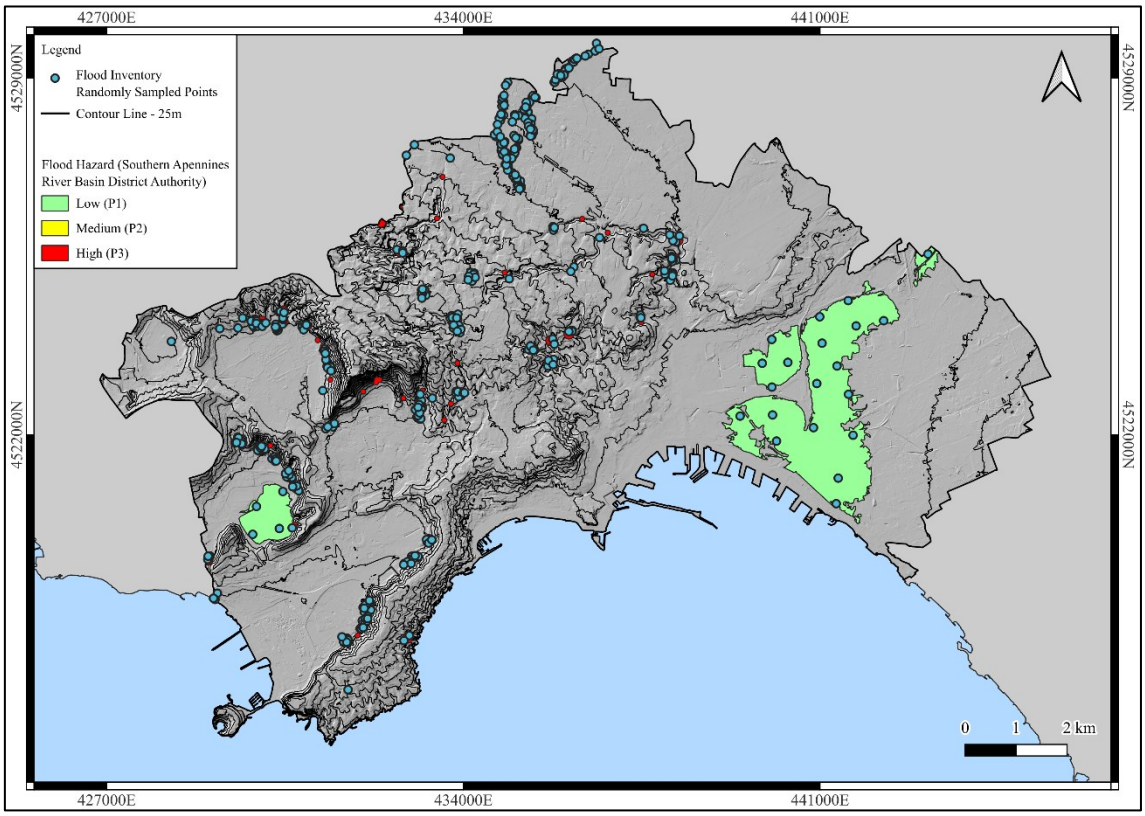

Figure 5.7: Flood Inventory imposed over the Flood Hazard map.

5.2. Predisposing factors

A total of 22 predisposing factors have been used in this study. These factors, obtained from literature, vary from morphological to interferometric data. In particular, the following predisposing factors were obtained from the Italian Ministry of the Environment, Land, and Sea (2005) DTM, which is characterized by a 20m × 20m resolution:

- DTM;
- Slope angle;
- Aspect;
- Planar Curvature (Plan_Cur);
- Profile Curvature (Prof_Cur);
- TPI – Topographic Position Index;
- TWI – Topographic Wetness Index.

All this data were obtained by processing the aforementioned DTM in SAGA GIS (Conrad et al., 2015) and are characterized by a 20m × 20m resolution.

The interferometric data were obtained from the European Ground Motion Service (EGMS) (Costantini et al., 2021). The downloaded data, for the 2018 – 2022 time frame, was in Shapefile format and rasterized using QGIS (QGIS Development Team, 2024).

- EGMS_E: the E-W component of the data (x-axis);
- EGMS_U: the vertical component of the data (z-axis).

The following data was obtained from the local administration (Naples municipality) and was processed in QGIS to obtain both the element density and the distance from the features maps. The density map measure unit is the # of features/km^2, while the distance map measure unit is in meters.

- AS_Net: which represents the aqueduct and sewer networks;
- Cav: the underground cavity networks, which comprehends galleries, cisterns, and catacombs;
- Cov_Thic: the thickness of the cover layers;
- Road: main and secondary road network.

The remaining predisposing factors were obtained from different sources:

- Hydr: the hydrographic network, data from ISPRA;
- Geology: the geological map from the CARG (Geological CARtography) project (*Servizio Geologico d'Italia*, 2015);
- GW_Lev: groundwater level (in meters a.s.l.) from Celico et al. (2001);
- Land_Use: data from the Corine Land Cover (European Union's Copernicus Land Monitoring Service, 2020);
- M_YRain: mean value of yearly rainfall for the last ~20 years, data from the Agricultural Department of the *Regione Campania*.

All the predisposing factors were rasterized in QGIS with a resolution of 20m × 20m, and EPSG (European Petroleum Survey Group) 32633 (WGS84 / UTM Zone 33N). An analysis to prevent collinearity problems with the predisposing factors has been carried out. In particular, the Variance Inflation Factor (VIF) analysis was performed in R. The Analysis showed extremely high collinearity issues with the vertical (EGMS_U) and E-W component (EGMS_E) of the interferometric data. The DTM and the Groundwater elevation data too show, although less severe, collinearity problems (Figure 5.8). Using the "*usdm*" package in R, an additional analysis with a threshold equal to 5 was performed. Two predisposing factors were removed from the following Relative Hazard assessment analysis: (i) DTM and (ii) EGMS_E.

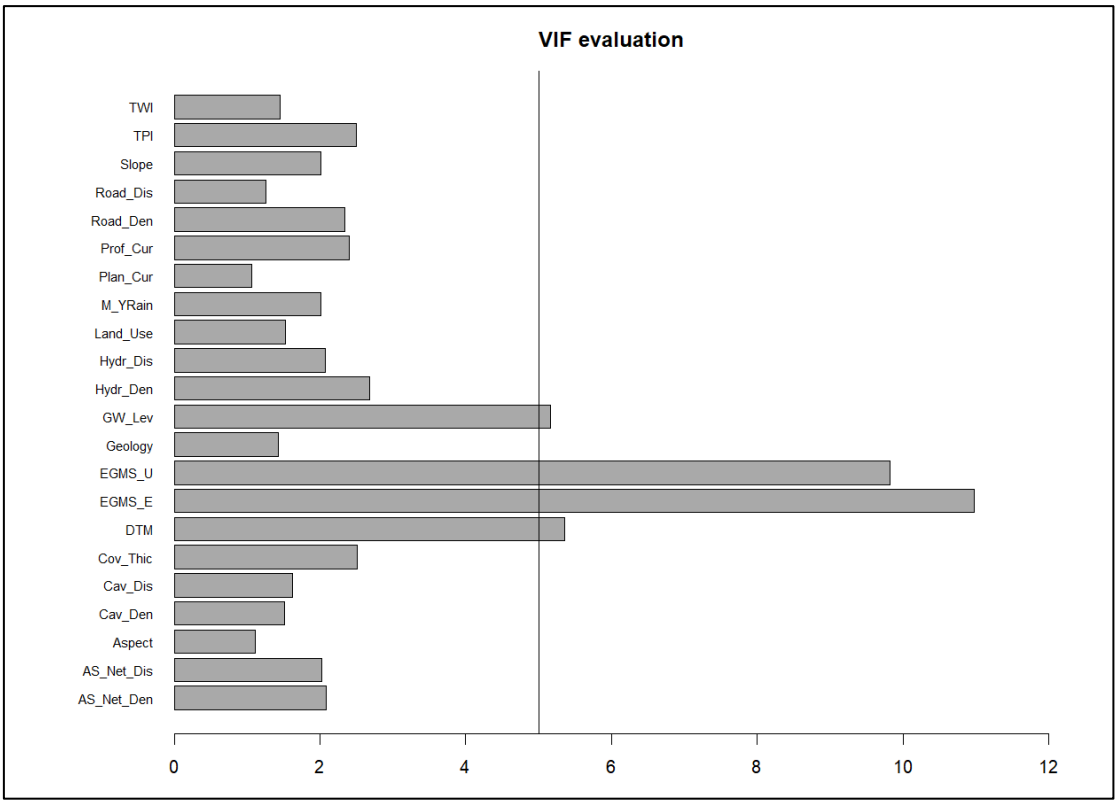

Figure 5.8: Results of the first iteration of the VIF analysis. The vertical black line is the threshold.

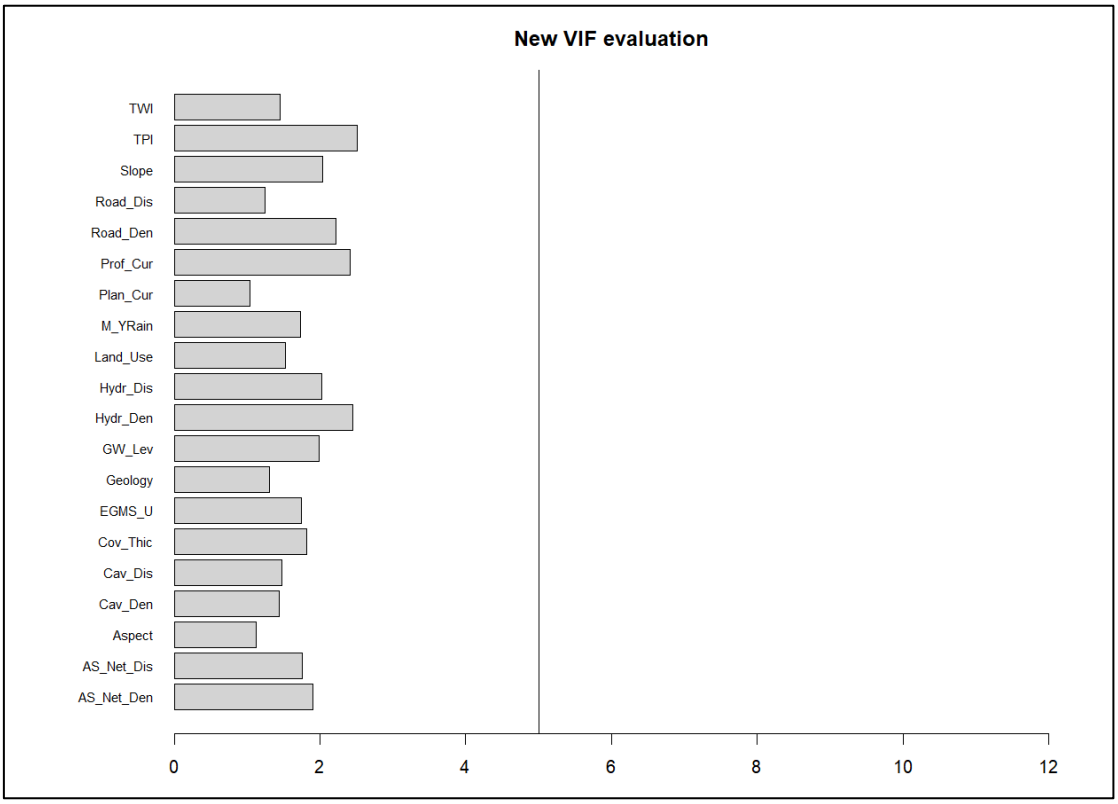

Figure 5.9: Results of the second iteration of the VIF analysis. The vertical black line is the threshold.

5.3. Elements at Risk (ER)

The ER map has been obtained by combining five different layers that represent both the strategic infrastructural network of the city of Naples and its valuable resources. In particular, the following maps have been categorized into Strategic and Non-Strategic elements (except for the Population Density):

- Buildings (Figure 5.10). Train stations, airport, port, schools, administrative and government buildings, barracks, museums etc. have been selected as buildings of strategic interest. For this reason, a higher weight value was attributed to those buildings;
- Natural Reserves (Figure 5.11). The Regional Phlegrean Fields Park and the *Parco Metropolitano delle Colline di Napoli* (Metropolitan Park of the Neapolitan Hills) are divided into three different zones and different weights have been attributed to every zone. The three zones are the (i) Zone A Integral Reserve, where no activities are allowed except for research; (ii) Zone B General Reserve, only tourism and activities related to local traditions are allowed by the Park; (iii) Zone C: Protected Landscape. In these zones, agrosilvopastoral and tourism-related activities can be planned.
- Population density (Figure 5.12) evaluated from the census data published by ISTAT. The population density varies from 0 to 0.184 inhabitants/m^2. The data was divided into five different classes using the Natural Breaks method (Jenks, 1977). Most of the Very High Population Density class are located within the city centre.
- The Road network (Figure 5.13) has been divided into strategic and non-strategic infrastructure. Within the strategic class fall the highways and the main roads due to their strategic importance in reaching or leaving the city.
- The Railway network (Figure 5.14), on the other hand, has been considered of strategic importance in its entirety.

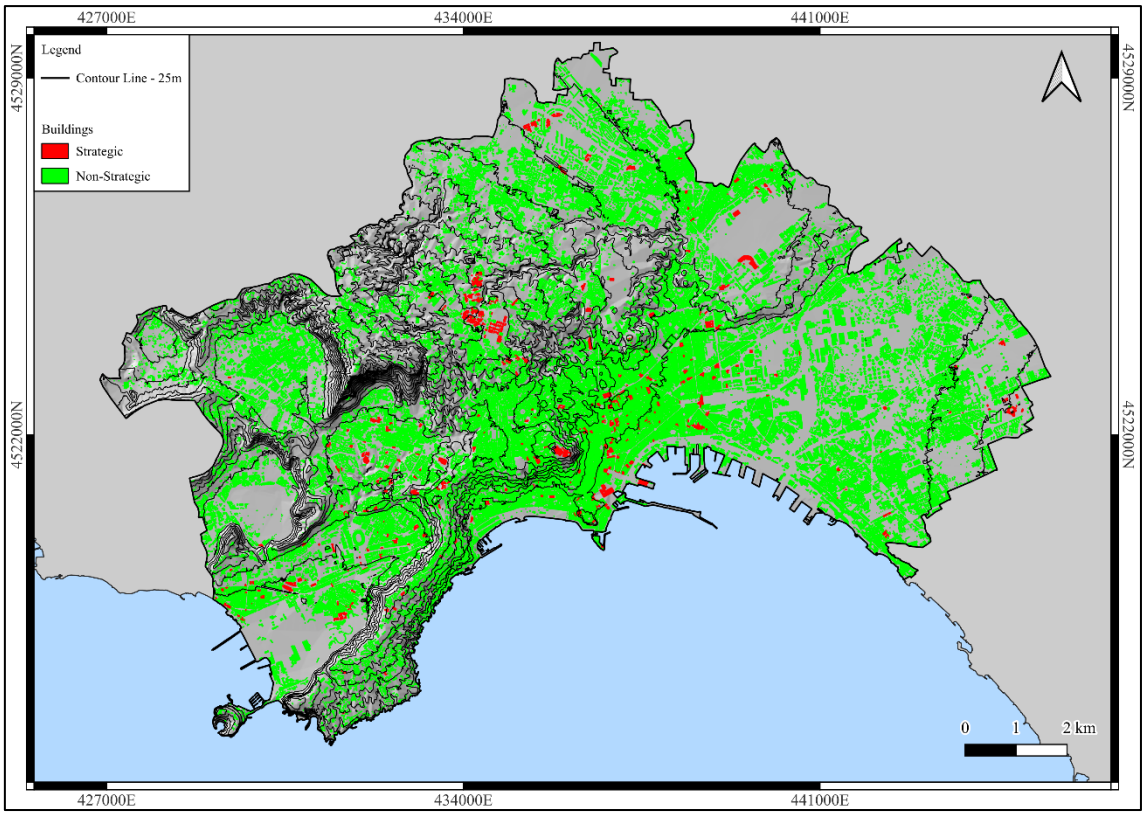

Figure 5.10: Strategic and non-strategic buildings in the city of Naples.

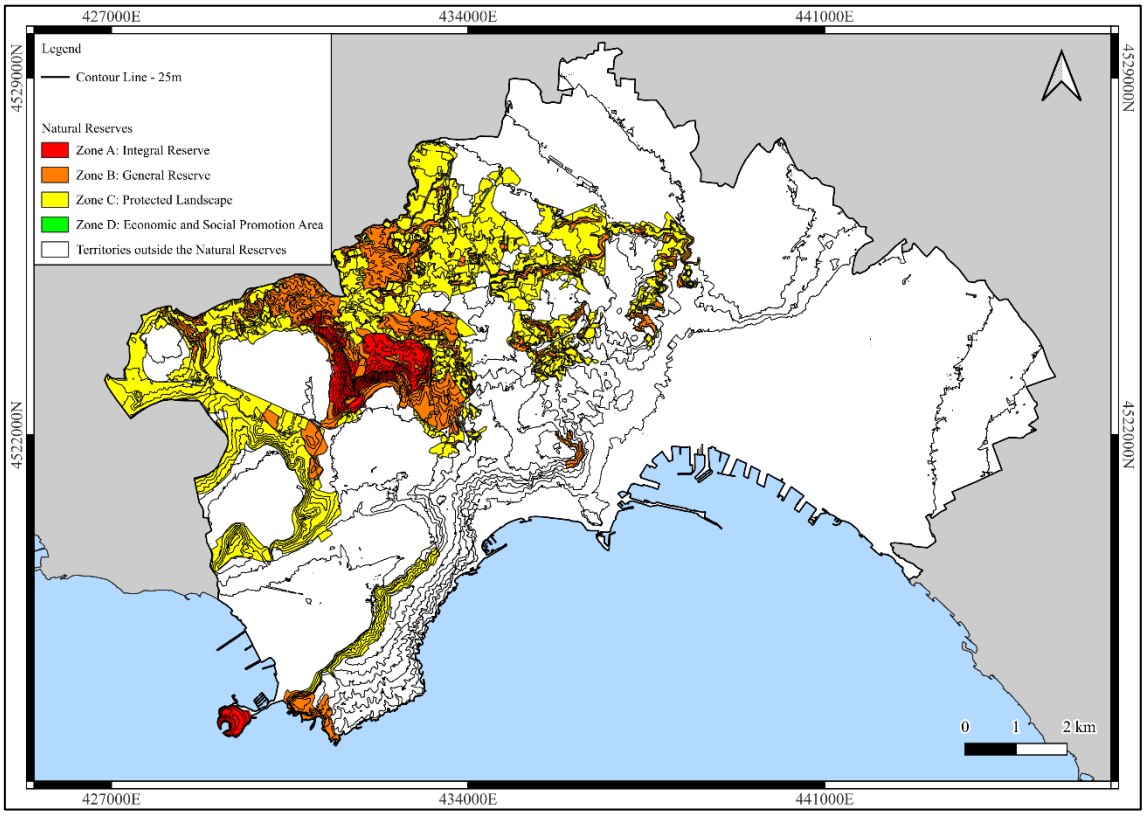

Figure 5.11: Natural Reserves map of the city of Naples.

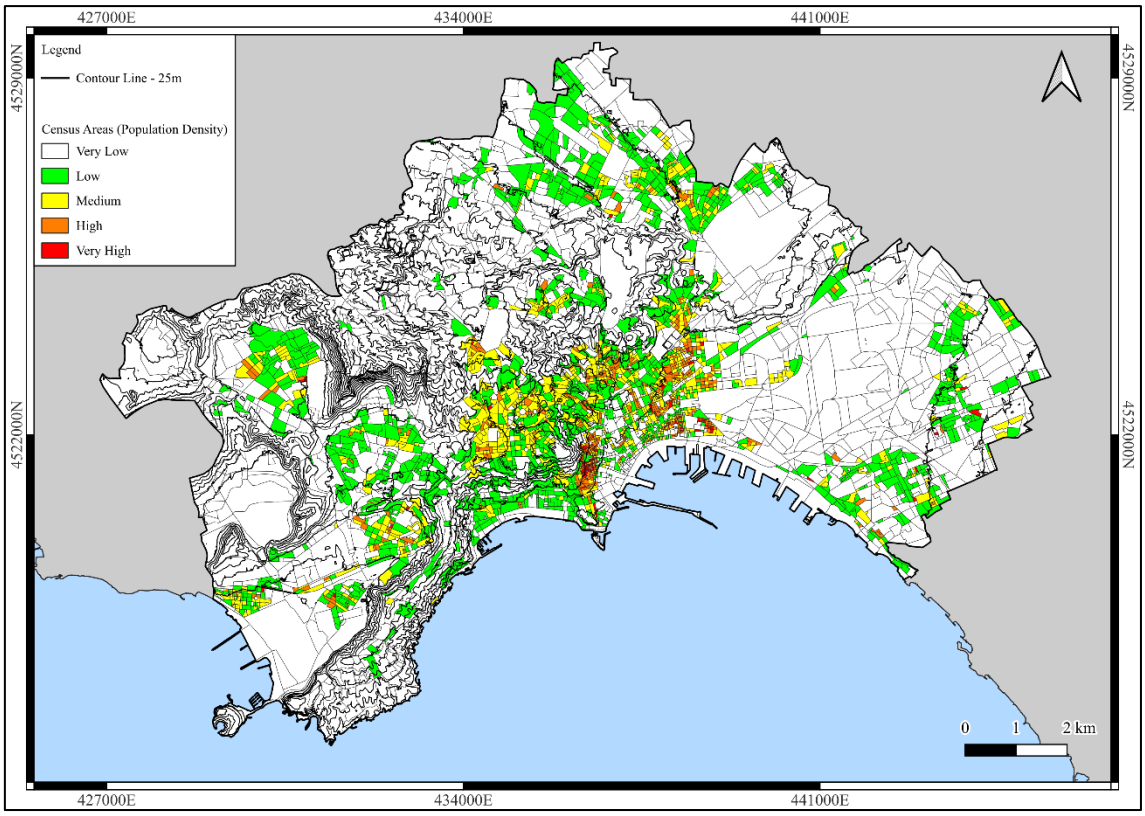

Figure 5.12: Population density map, data obtained from ISTAT.

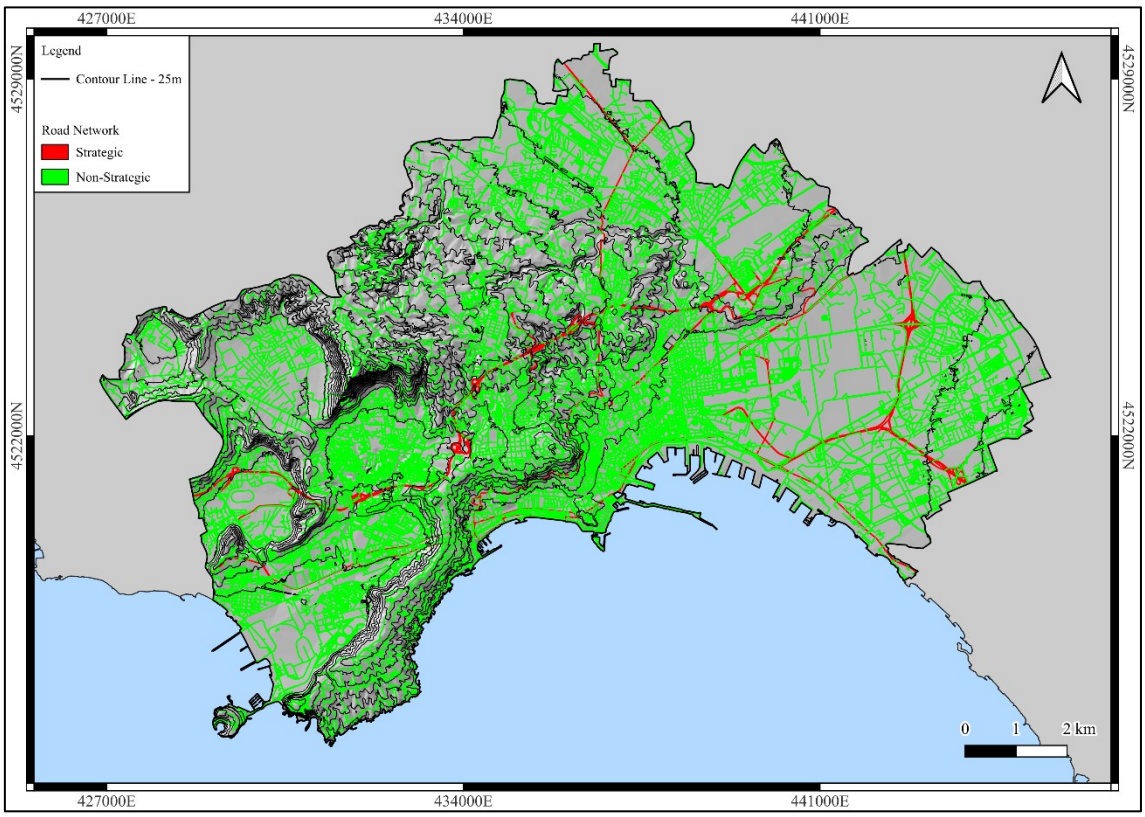

Figure 5.13: Road Network map for the city of Naples.

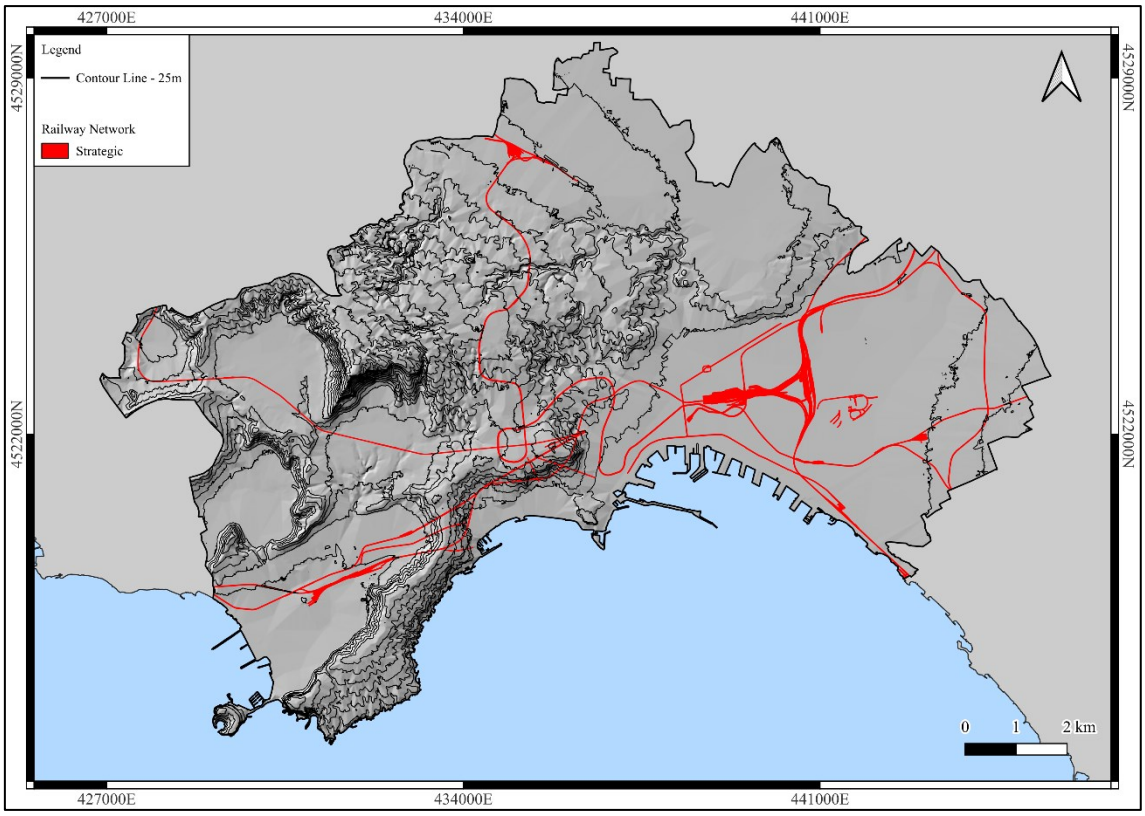

Figure 5.14: Railway Network of the city of Naples.

Subsequently, the aforementioned five layers were combined into a single Elements at Risk layer using QGIS. This union process also allowed us to inherit the weight value of every original layer. Finally, the field calculator tool was used to find the highest Element at Risk weight value among the ones inherited from the original layers for every area. The evaluation of the Damage map (Elements at Risk × Vulnerability) is the final step of the preprocessing phase (Figure 5.15). Due to the high complexity of the study area (extremely heterogeneous and highly urbanized) a cautionary approach was implemented. The Vulnerability value for the entire study area was set as 1.

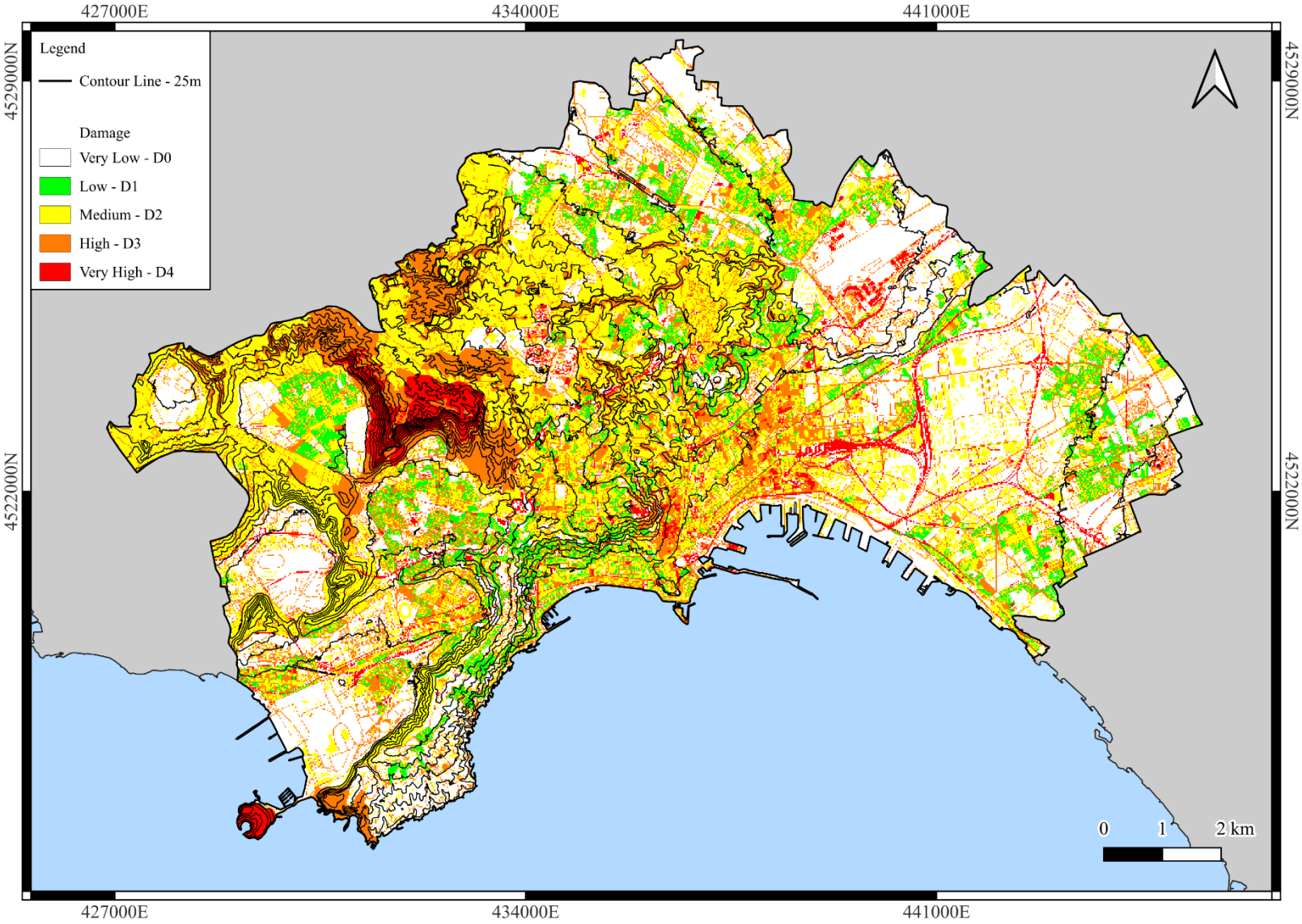

Figure 5.15: Damage map of the city of Naples.

5.4. Relative Hazard assessment

The Relative Hazard evaluation has been performed using the ML algorithms MaxEnt and RF. Fifteen Pseudo Absence (PAb) data sets were produced with the *"biomod2"* package (Figure 5.16 to 5.18).

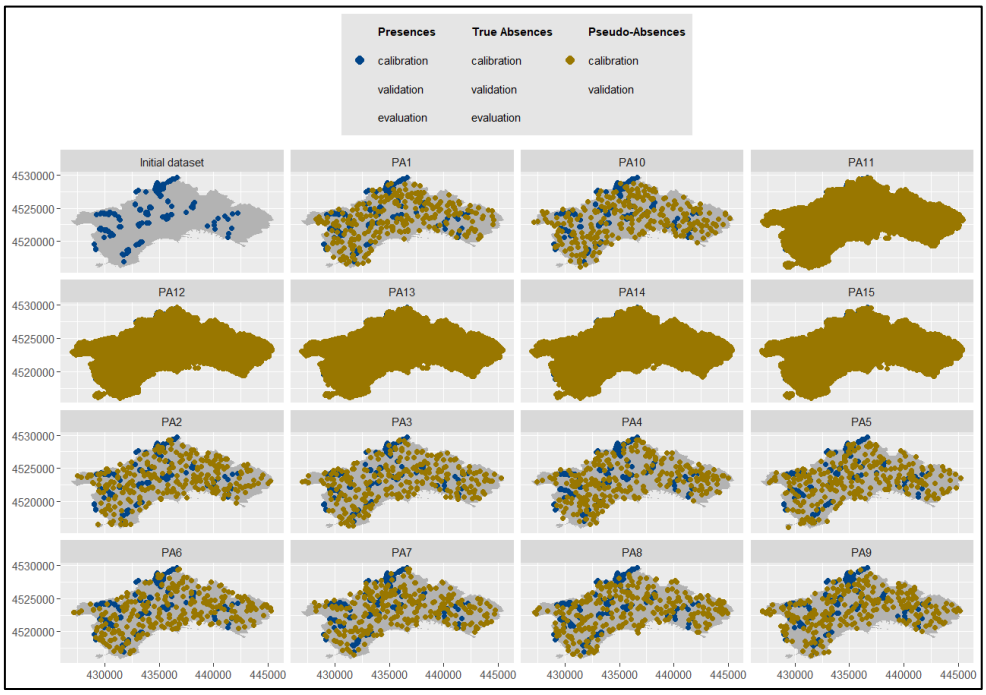

Figure 5.16: Flood Presence and Pseudo Absence points.

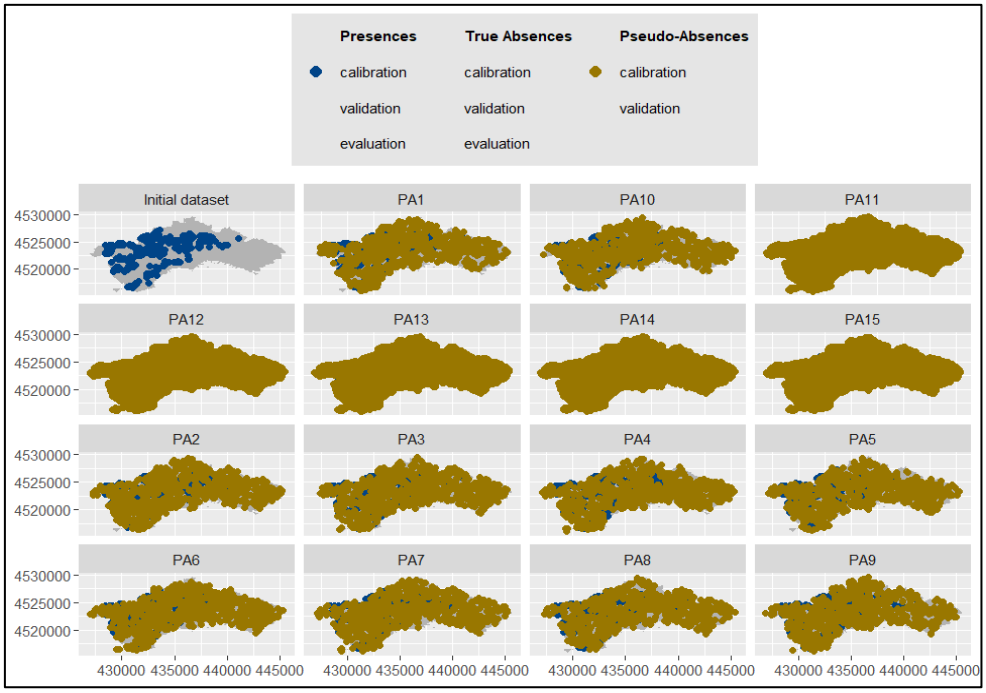

Figure 5.17: Landslide Presence and Pseudo Absence points.

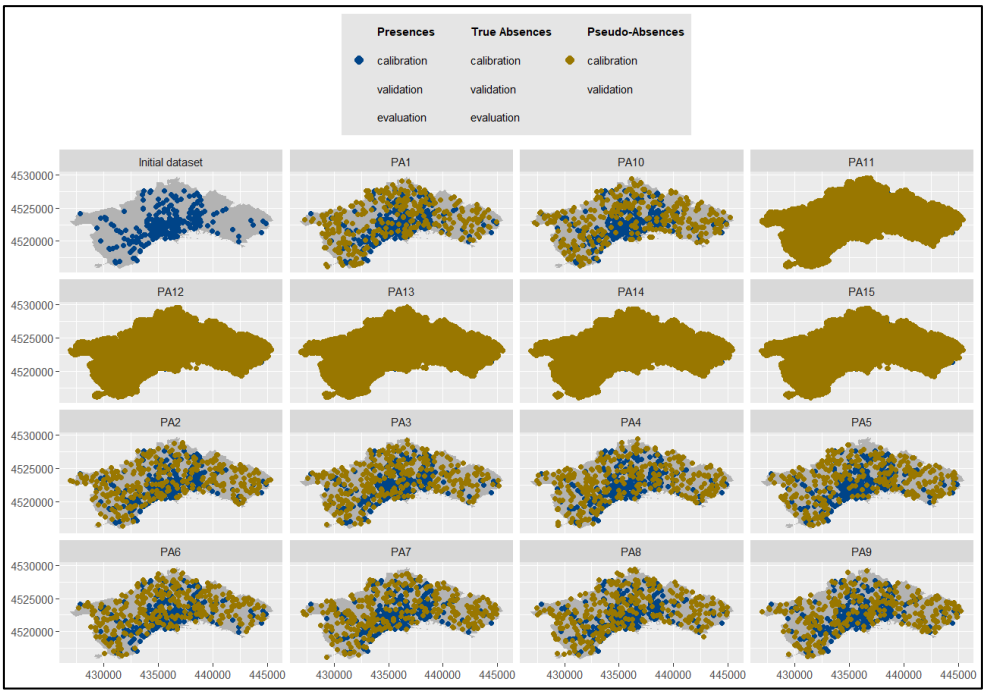

Figure 5.18: Sinkhole Presence and Pseudo Absence points.

The first ten were used by the RF algorithm (PA1, PA2, PA3, PA4, PA5, PA6, PA7, PA8, PA9, PA10) and were produced by randomly selecting a number of PAb points equal to the number of training set points for every geohazard. The remaining five sets were reserved for the MaxEnt algorithm (PA11, PA12, PA13, PA14, PA15) and employed 10000 PAb random points. Using the k-fold cross-validation technique (with k = 3), every modelization cycle performed for every PAb set was repeated three times, alternating the training sets and the validation set, for a total of 30 RF models and 15 MaxEnt models.

The performance of the models were validated by the "*biomod2*" package itself with the ROC/AUC technique using the 3-fold cross-validation. This step was necessary as the EM assessment uses only the models with a ROC/AUC score higher than the user-set threshold (in this study, 0.85). The performance scores achieved by every model is shown in the following table (Table 5.2) and, most of them, have achieved an excellent performance, falling above the 0.85 threshold (Figure 5.19).

Table 5.2: ROC score (performance) of the Relative Hazard maps.

PAb set	*k*	Algorithm	Flood Validation	Landslide Validation	Sinkhole Validation
PA1	RUN1	RF	0.94	0.94	0.88
PA1	RUN2	RF	0.90	0.92	0.89
PA1	RUN3	RF	0.91	0.92	0.86
PA2	RUN1	RF	0.90	0.90	0.90
PA2	RUN2	RF	0.92	0.89	0.87
PA2	RUN3	RF	0.89	0.93	0.83
PA3	RUN1	RF	0.91	0.93	0.90
PA3	RUN2	RF	0.92	0.93	0.89
PA3	RUN3	RF	0.89	0.94	0.90
PA4	RUN1	RF	0.95	0.95	0.93
PA4	RUN2	RF	0.95	0.92	0.87
PA4	RUN3	RF	0.91	0.92	0.87
PA5	RUN1	RF	0.92	0.93	0.93
PA5	RUN2	RF	0.94	0.92	0.89
PA5	RUN3	RF	0.90	0.90	0.89
PA6	RUN1	RF	0.94	0.93	0.84
PA6	RUN2	RF	0.91	0.92	0.89
PA6	RUN3	RF	0.92	0.92	0.83
PA7	RUN1	RF	0.94	0.91	0.93
PA7	RUN2	RF	0.91	0.92	0.86
PA7	RUN3	RF	0.93	0.93	0.87
PA8	RUN1	RF	0.93	0.92	0.84
PA8	RUN2	RF	0.93	0.95	0.91
PA8	RUN3	RF	0.91	0.91	0.89
PA9	RUN1	RF	0.91	0.94	0.87
PA9	RUN2	RF	0.88	0.93	0.91
PA9	RUN3	RF	0.96	0.91	0.90
PA10	RUN1	RF	0.93	0.89	0.91
PA10	RUN2	RF	0.93	0.93	0.87
PA10	RUN3	RF	0.95	0.92	0.90
PA11	RUN1	MAXENT	0.92	0.92	0.88
PA11	RUN2	MAXENT	0.87	0.90	0.87
PA11	RUN3	MAXENT	0.91	0.91	0.86
PA12	RUN1	MAXENT	0.95	0.90	0.87

PA12	RUN2	MAXENT	0.91	0.92	0.88
PA12	RUN3	MAXENT	0.89	0.92	0.85
PA13	RUN1	MAXENT	0.91	0.92	0.84
PA13	RUN2	MAXENT	0.87	0.93	0.89
PA13	RUN3	MAXENT	0.90	0.90	0.89
PA14	RUN1	MAXENT	0.85	0.91	0.89
PA14	RUN2	MAXENT	0.86	0.91	0.86
PA14	RUN3	MAXENT	0.91	0.92	0.84
PA15	RUN1	MAXENT	0.90	0.92	0.89
PA15	RUN2	MAXENT	0.90	0.90	0.86
PA15	RUN3	MAXENT	0.94	0.92	0.86

In particular (Table 5.3), the minimum and maximum performance score (ROC/AUC) obtained for the RF algorithm for Flood Relative Hazard assessment is 0.88 and 0.96, against 0.85 and 0.95 from MaxEnt. The average and the standard deviation evaluated are, respectively, 0.92 and 0.019 for RF and 0.90 and 0.026 for MaxEnt. Considering all the runs, the minimum, maximum, average and standard deviation are equal to 0.95, 0.96, 0.91, and 0.024. As for the Landslide Relative Hazard validation scores, the RF algorithm minimum, maximum, average and standard deviation obtained are 0.89, 0.95, 0.92, and 0.014, while the MaxEnt algorithm is characterized by the following statistics: 0.90 (minimum value), 0.93 (maximum value), 0.91 (average value), and 0.010 (standard deviation). The statistics evaluated on the entire set of models is 0.89, for the minimum, 0.95 for the maximum, 0.92 as the average and 0.013 for the standard deviation. Finally, the statistics for the RF and MaxEnt Sinkhole Relative Hazard assessment, respectively, are the following: 0.83 and 0.84 (minimum); 0.93 and 0.89 (maximum); 0.88 and 0.87 (average); 0.026 and 0.017 (standard deviation). In general, the statistics evaluated on the entire set of models are: 0.83 (minimum); 0.93 (maximum); 0.88 (average); and 0.025 (standard deviation).

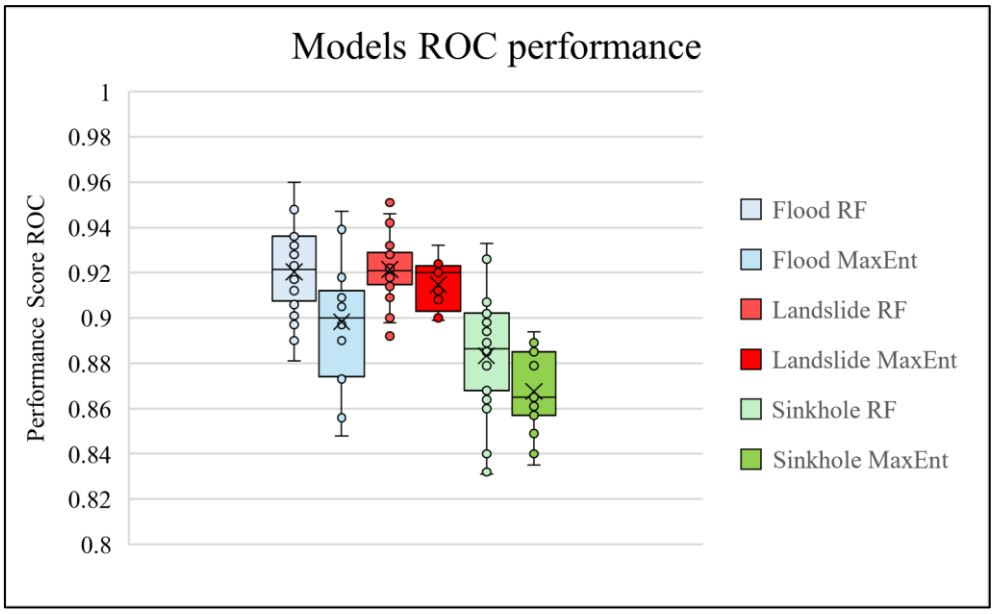

Figure 5.19: ROC performance of the Flood, Landslide, and Susceptibility Relative Hazard models.

Table 5.3: Statistics of the models obtained using the biomod2 package.

Statistics	Flood	Landslide	Sinkhole
Min ROC/AUC (total)	0.85	0.89	0.83
Min ROC/AUC (RF)	0.88	0.89	0.83
Min ROC/AUC (MaxEnt)	0.85	0.90	0.84
Max ROC/AUC (total)	0.96	0.95	0.93
Max ROC/AUC (RF)	0.96	0.95	0.93
Max ROC/AUC (MaxEnt)	0.95	0.93	0.89
Average ROC/AUC (total)	0.91	0.92	0.88
Average ROC/AUC (RF)	0.92	0.92	0.88
Average ROC/AUC (MaxEnt)	0.90	0.91	0.87
Standard Deviation (total)	0.024	0.013	0.025
Standard Deviation (RF)	0.019	0.014	0.026
Standard Deviation (MaxEnt)	0.026	0.010	0.017

The importance of the predisposing factors used for the Relative Hazard assessment are shown in the following table (Table 5.4). These values are the average of the importance values obtained for every single model produced. For every run, the Variable Importance was evaluated three times for every Variable, adding to 135 Variable Importance scores evaluated for every model. This means that, for every Relative Hazard Map, 2700 Variable Importance scores were calculated, for a total of 2700 evaluations for every Relative Hazard map (135 × 20 Predisposing Factors), for a total of 8100 permutations.

Table 5.4: Normalized importance of predisposing factors evaluated with the permutation importance.

Predisposing Factor	Variable Importance [%]		
	Flood	Landslide	Sinkhole
AS_Net_Den	5.06	1.34	3.86
AS_Net_Dis	1.54	1.50	19.18
Aspect	1.35	1.15	1.42
Cav_Den	2.52	1.87	5.39
Cav_Dis	3.22	1.57	13.75
Cov_Thic	3.93	1.22	0.64
EGMS_U	4.98	3.68	1.22
Geology	0.98	1.75	1.28
GW_Lev	13.76	6.75	3.68
Hydr_Den	4.45	2.84	6.87
Hydr_Dis	22.93	6.82	2.92
Land_Use	1.99	2.81	0.18
M_YRain	10.10	1.50	2.47
Plan_Cur	0.55	0.85	0.77
Prof_Cur	1.36	1.48	1.07
Road_Den	11.09	6.89	2.47
Road_Dis	1.42	1.40	29.60
Slope	5.47	46.54	1.53
TPI	1.15	2.08	0.78
TWI	2.15	5.96	0.92

From the analysis, it appears that the most influential parameters for the Flood Relative Hazard modelization are (i) distance from the hydrographic network, (ii) groundwater elevation, (iii) road density, and (iv) mean annual rainfall. For the Landslide Relative Hazard assessment, the most significant predisposing factors are (i) slope angle, (ii) road density, (iii) distance from the hydrographic network, (iv) groundwater elevation. As for the Sinkhole Relative Hazard modelization, the most important predisposing factors are (i) road network distance, (ii) aqueduct and sewer main networks distance, (iii) underground cavities distance, and (iv) density of the hydrographic network. The models were combined in an Ensemble with a Weighted Mean approach. The weight was evaluated from the previously shown validation scores (Table 5.2), meaning that models with higher performance were characterized by a higher weight. The threshold set was 0.85, which means that all the models that fall under that value

were excluded from the EM process. Out of 45 models, all of them were used to produce the Flood and the Landslide, while seven Sinkhole Relative Hazard models did not reach the threshold value (four RF models and three MaxEnt models). The remaining 38 models were combined to produce the Sinkhole Relative Hazard map. The performance scores of the three produced maps (Figure 5.20 to 5.22) were subsequently assessed, using the ROC/AUC technique with independent test data. The High and Very High Flood Relative Hazard classes are located mainly at the foot of the hills (*Camaldoli*, northern side of *Posillipo*, *Capodimonte* and *Arenella* Hills), the *Pisani* area, *Agnano* and *Pianura* plains, and the northern sector of the city (*Chiaiano* neighbourhood) (Figure 4.3 for the toponym positions). High flood Relative Hazard is also located in the eastern sector of the city (*Barra* and *Ponticelli*). The central and North-eastern sectors of the city appear to be less susceptible to floods. At the same time, the portions of *Soccavo* and *Fuorigrotta* neighbourhoods located far from the hills also fall within the Very Low Relative Hazard class (Figure 5.20). As for the Landslide Relative Hazard map (Figure 5.21), the High and Very High classes are located along the steepest slopes (*Camaldoli* Hill and northern side of the *Posillipo* Hill), the hillsides on the border of the *Agnano* Plain and the *Pianura* neighbourhood, along the San Rocco Valley, and the *Chiaiano* quarries. The Medium Relative Hazard class is widespread along the aforementioned areas and the southern side of the *Posillipo* and *Vomero* Hills. *Bagnoli*, *Fuorigrotta*, *Soccavo*, *Pianura*, the eastern and the northern sectors of the city seem to be characterized by Low and Very Low Relative Hazard. As for the Sinkhole Relative Hazard map (Figure 5.22), the High and Very High classes are located in the city center, the *Vomero* and *Arenella* Hills, and along the main roads of the remaining neighbourhoods. The *Pisani* location and the *Agnano* plain are characterized by the presence of Low and Very Low Sinkhole Relative Hazard. Most hillslopes of the city (western *Posillipo*, *Monte Spina*, *Camaldoli*, hillslopes around the *Agnano* plain, quarries of *Chiaiano* neighbourhood) fall within the Very Low Relative Hazard class.

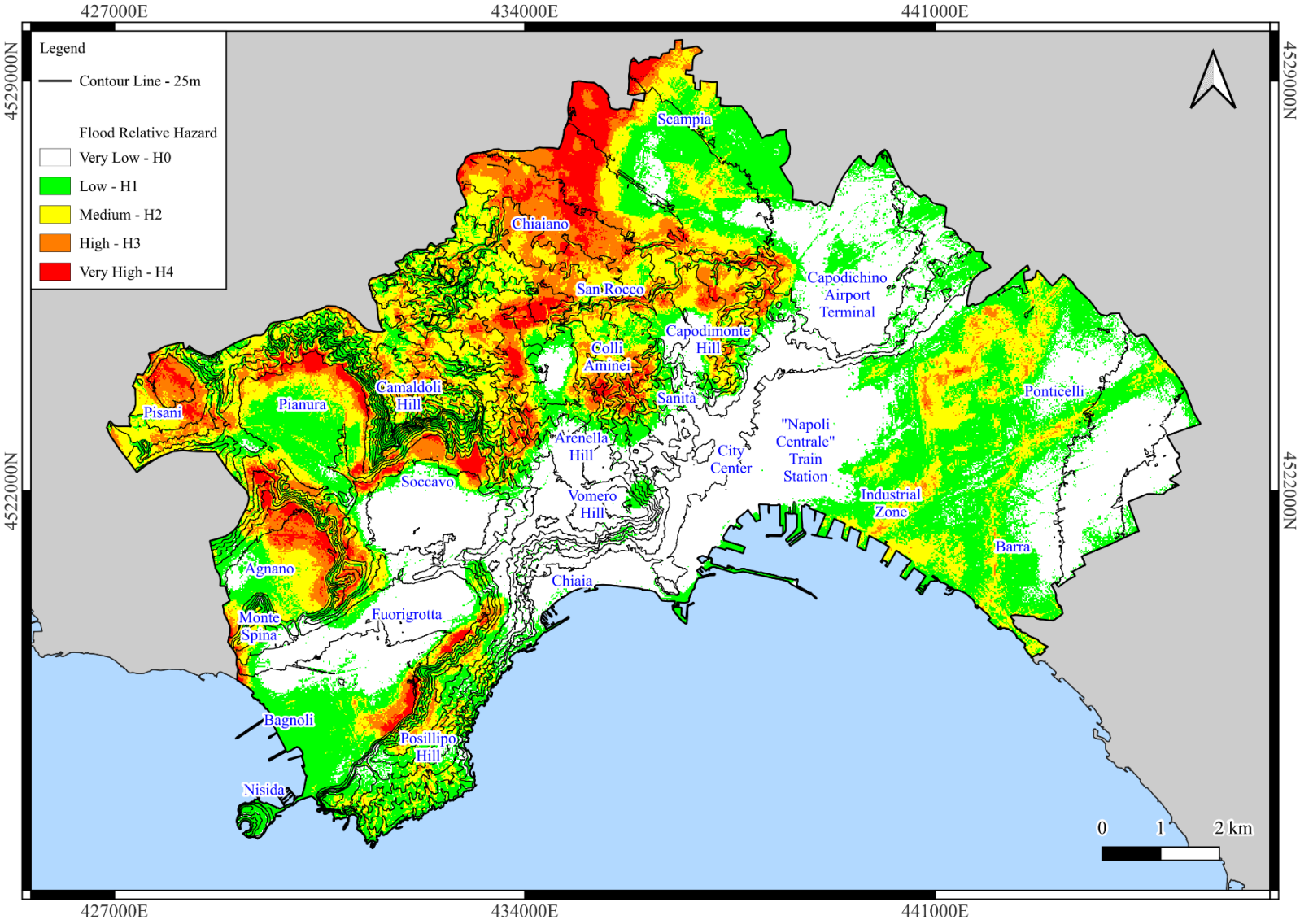

Figure 5.20: Flood Relative Hazard Map.

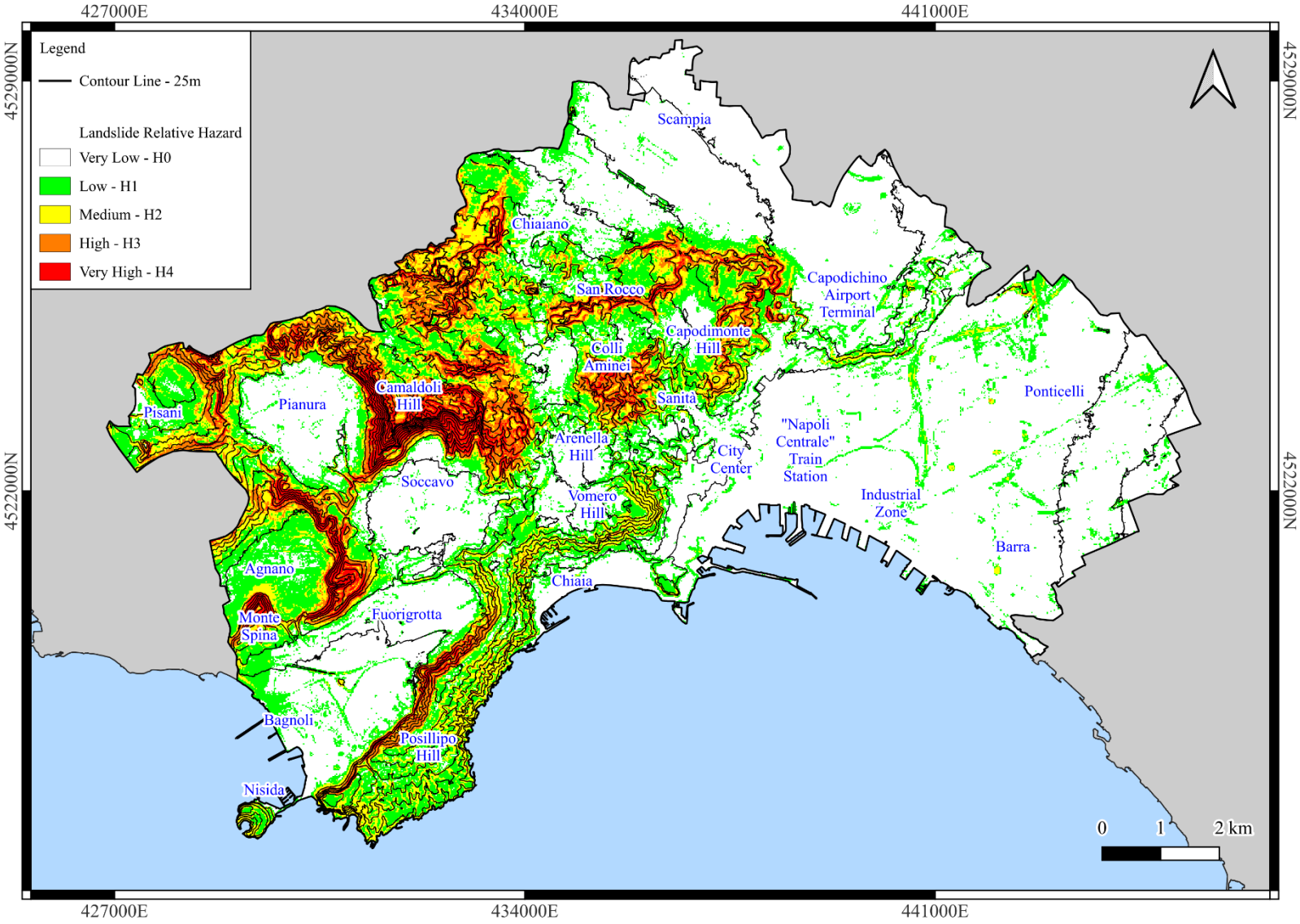

Figure 5.21: Landslide Relative Hazard Map.

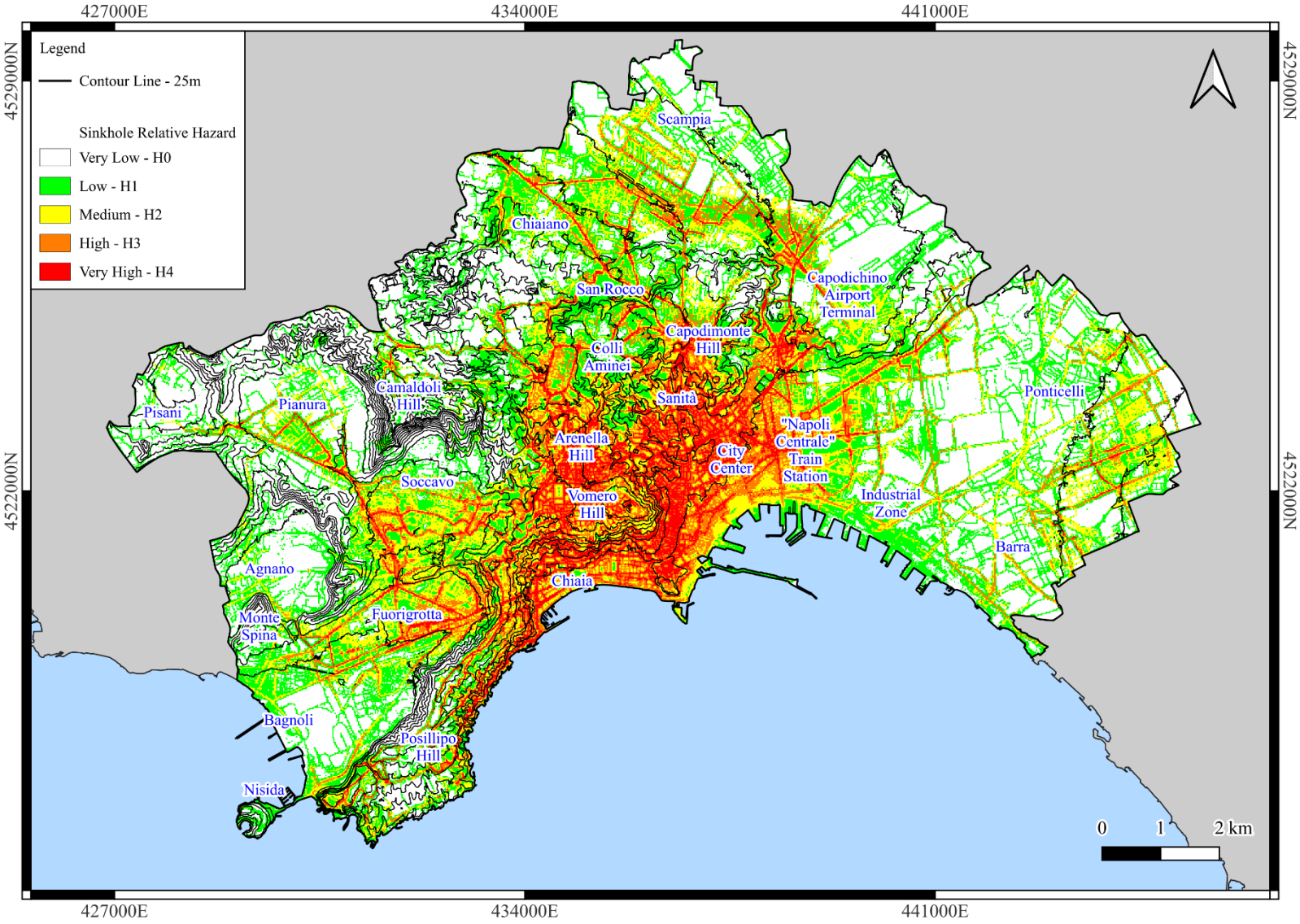

Figure 5.22: Sinkhole Relative Hazard map.

The performance obtained by this model has been evaluated using a totally independent test data, composed of 30% of the original inventories, to assure that no positive bias was present within the final performance score. Flood (Figure 5.23) and Landslide (Figure 5.24) Relative Hazard are both characterized by excellent performance scores (ROC/AUC = 0.94), while the Sinkhole Relative Hazard (Figure 5.25) performance is lower (ROC/AUC = 0.89), but still good.

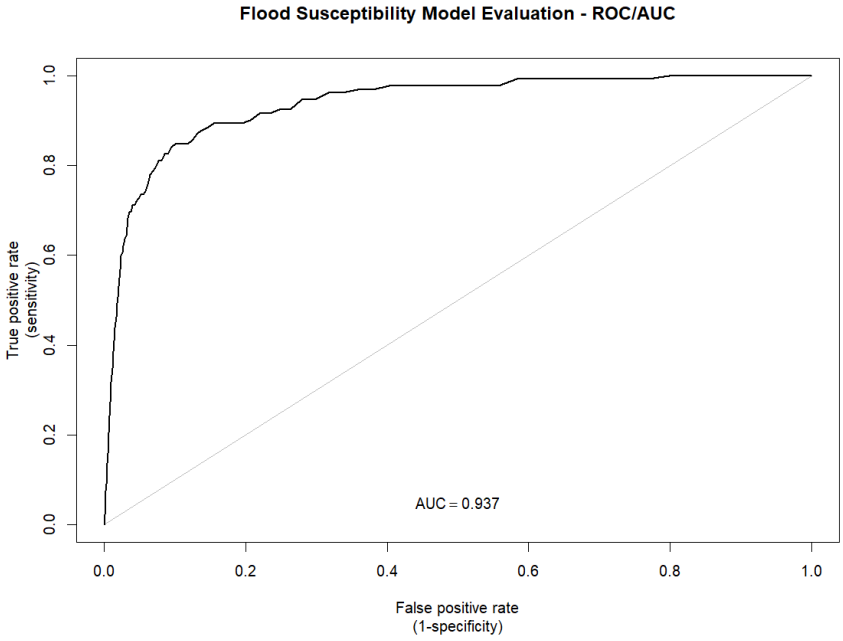

Figure 5.23: ROC/AUC diagram for the performance evaluation of the Flood Relative Hazard map, using the modEvA package.

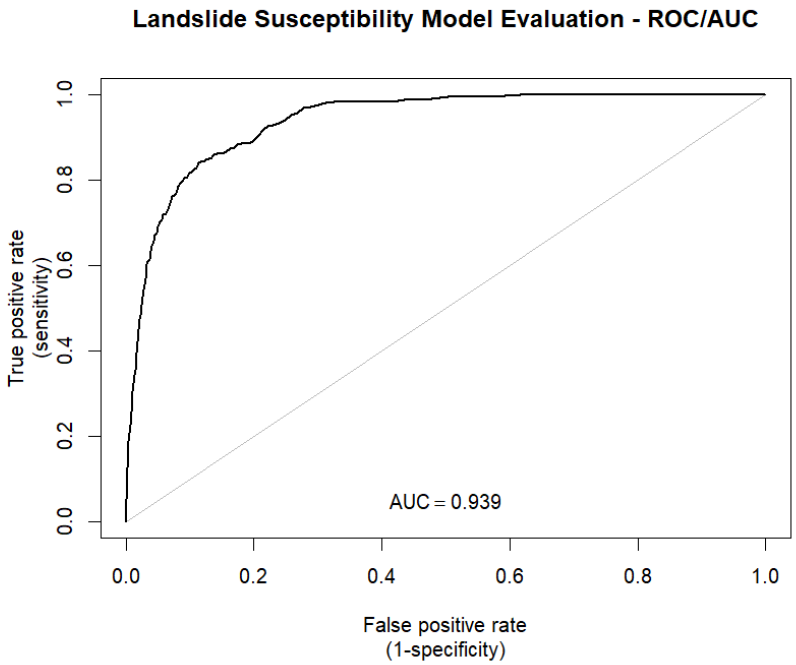

Figure 5.24: ROC/AUC diagram for the performance evaluation of the Landslide Relative Hazard map, using the modEvA package.

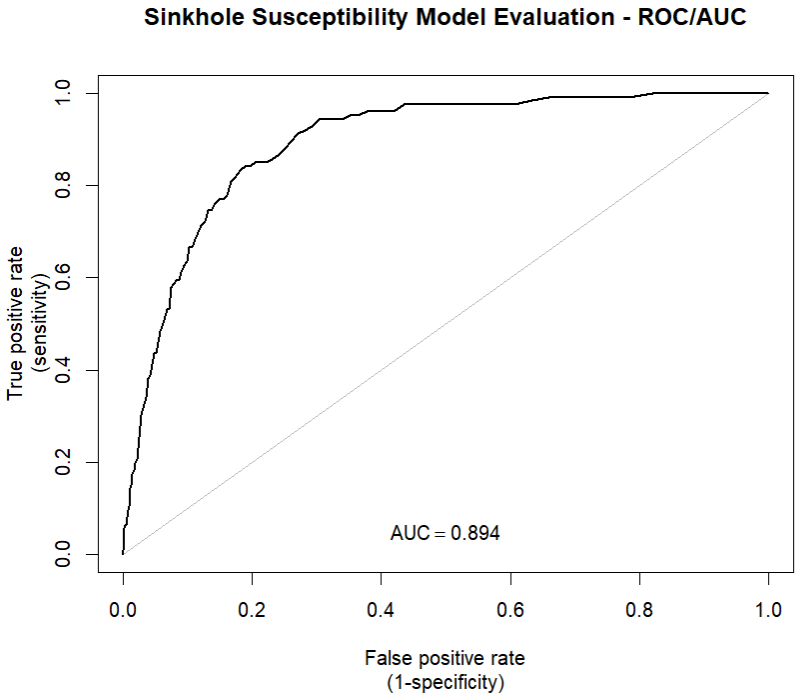

Figure 5.25: ROC/AUC diagram for the performance evaluation of the Sinkhole Relative Hazard map, using the modEvA package.

5.5. Geohazard Risk assessment

The Flood (Figure 5.26), Landslide (Figure 5.27), and Sinkhole (Figure 5.28) Risk maps were obtained by combining Relative Hazard maps with Damage map using the Risk Matrix (Table 5.5). The Relative Hazard map has been used instead of the Hazard map due to the lack of an adequate amount of temporal information in the inventories used as presence data. Approximately 57% of the landslide inventory and 100% of the flood inventory did not, indeed, contain temporal information. The Matrix appears different from a traditional Matrix (Table 5.6) due to the changes related to the column H0 and the row D0. These columns and rows were set as R0 throughout the matrix, as they represent an absence of Damage and/or Relative Hazard.

Table 5.5: Risk Matrix.

Risk Matrix		Relative Hazard				
		H0	H1	H2	H3	H4
Damage	D0	R0	R0	R0	R0	R0
	D1	R0	R1	R2	R2	R3
	D2	R0	R2	R2	R3	R3
	D3	R0	R2	R3	R3	R4
	D4	R0	R3	R3	R4	R4

Table 5.6: A more traditional Matrix.

Risk Matrix		Relative Hazard				
		H0	H1	H2	H3	H4
Damage	D0	R0	R1	R1	R2	R2
	D1	R1	R1	R2	R2	R3
	D2	R1	R2	R2	R3	R3
	D3	R2	R2	R3	R3	R4
	D4	R2	R3	R3	R4	R4

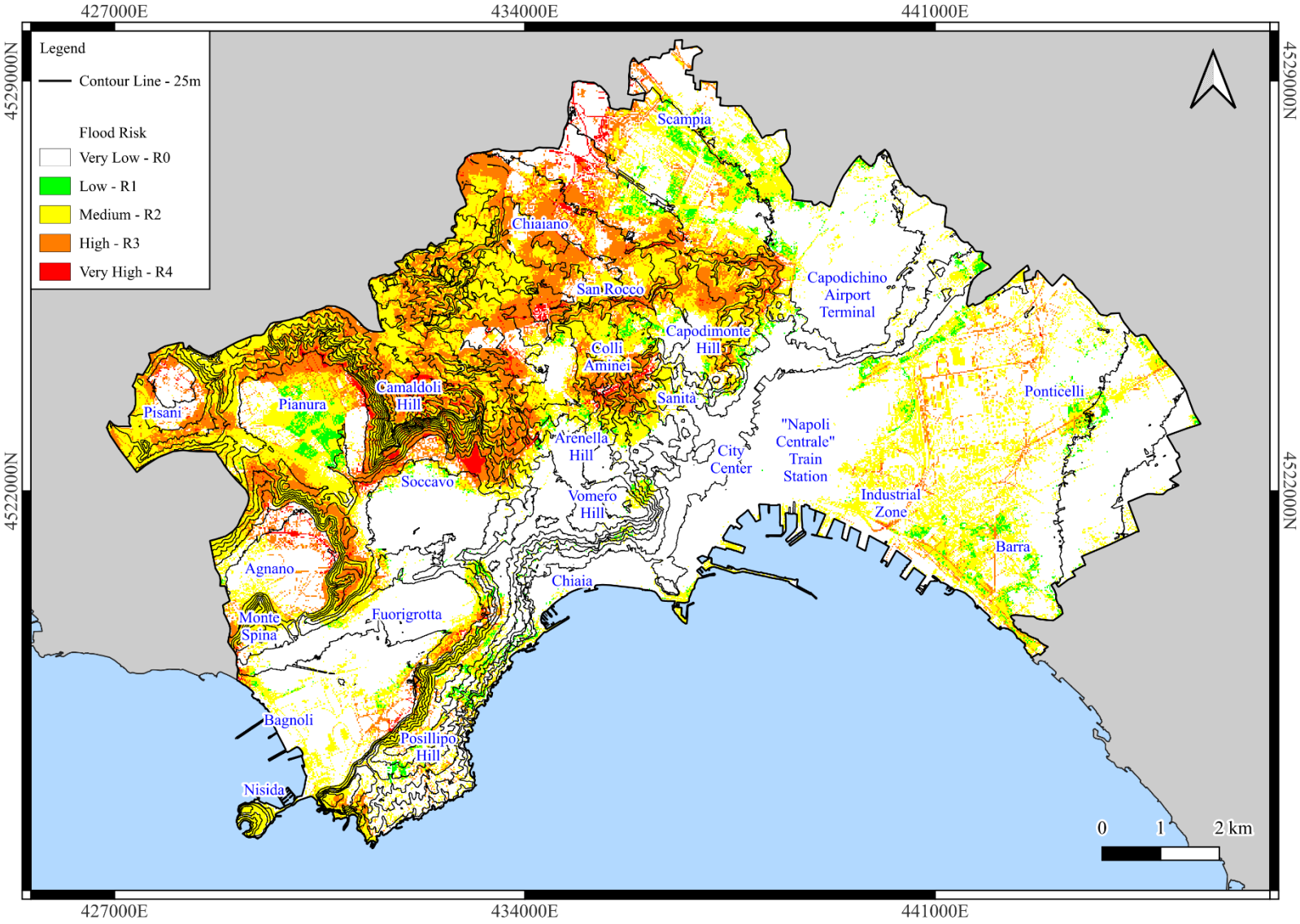

Figure 5.26: Flood Risk Map.

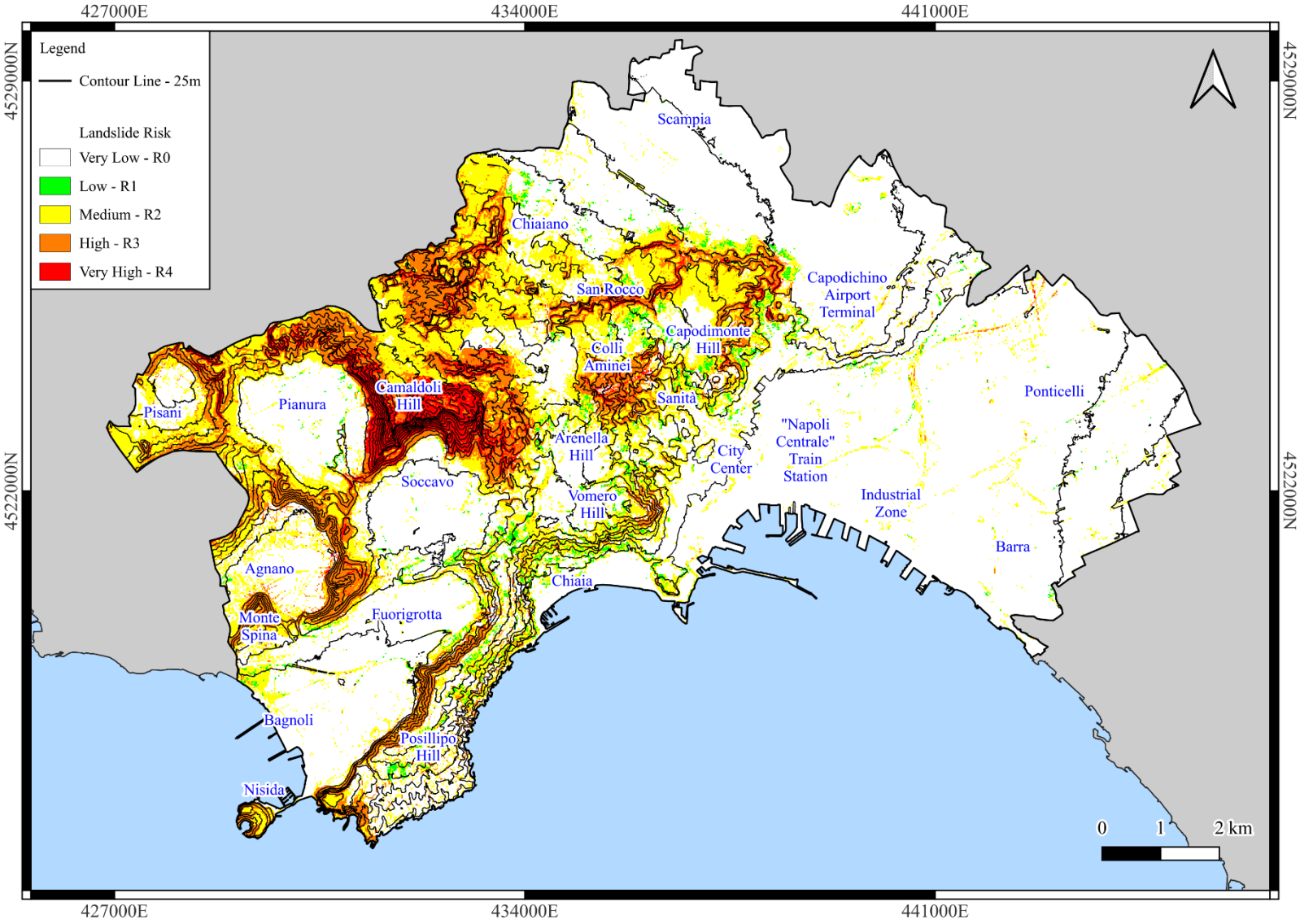

Figure 5.27: Landslide Risk Map.

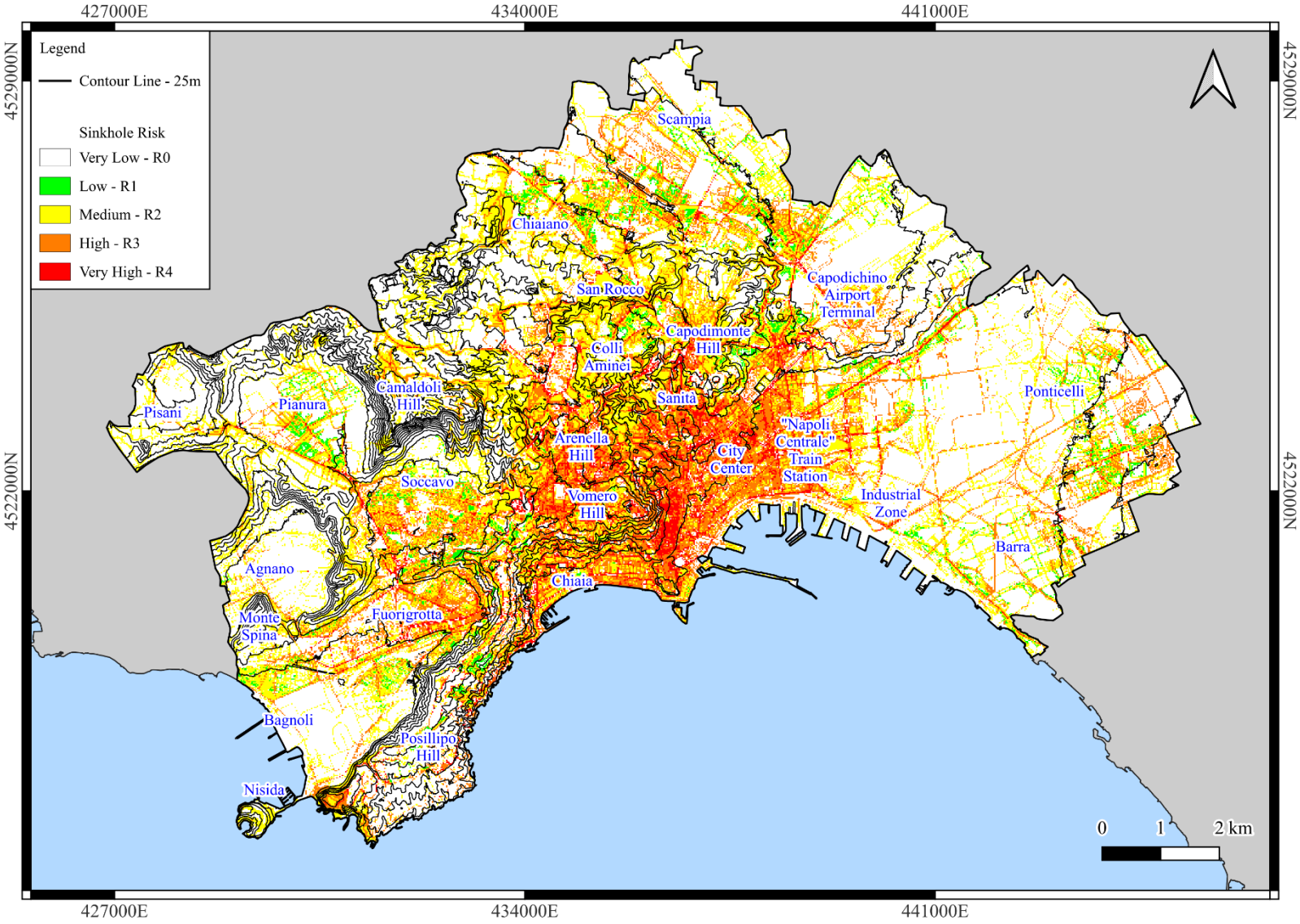

Figure 5.28: Sinkhole Risk Map.

The Flood risk map is characterized by the presence of Very High Risk areas in the northern sector of the city, along the *Capodimonte* and *Arenella* Hills, and in the plains located in the eastern sector of the city and *Agnano* (Figure 4.3 for the toponym positions). Very High Risk also characterizes the foot of the *Camaldoli* Hill (*Pianura* and *Soccavo* neighbourhoods). The High and Medium Risk classes are located in the eastern sector of the city, in the *Bagnoli* neighbourhood, the northern sector of the city, and the *Chiaiano* neighbourhood, the *Vallone San Rocco* and the Natural Reserves. Most of the city center, the *Vomero* hill, and the *San Pietro a Patierno* (North-North-East sector of the city) neighbourhood are characterized by Very Low Flood Risk.

As for the Landslide risk map, the Very High and High Risk classes are mainly located along the *Camaldoli* hillslopes, the *Chiaiano* quarries, the *Vallone San Rocco* and *Capodimonte*. The High Risk class is also located along the western and northern sides of the *Posillipo* Hill, *Nisida*, *Monte Spina*, and along the slopes of *Vomero* hill that face the city center. The slopes that border the *Pisani* and the *Agnano* areas are also characterized by High Risk. Most of the remaining areas of the city are characterized by Very Low Landslide Risk, with Medium and Low landslide risk along at the areas characterized by higher Landslide Risk. There is an exception in the eastern sector of the city, where small areas that fall within the Medium, High and Very High Risk classes are located.

High and Very High Sinkhole Risk classes are present in most areas of the city of Naples. The city center and the *Vomero* and *Arenella* Hills are the most affected zones. *Soccavo* and *Fuorigrotta* too are largely impacted by High and Very High Sinkhole Risk, while *Bagnoli*, *Pisani*, *Agnano* and the South-West sector of the *Posillipo* Hill and most hillslopes seem to be the less affected areas. The Medium and Low Risk classes are quite widespread all over the city, except the aforementioned city center.

5.6. Multirisk Analysis using the RES approach

Using the RES approach, it is possible to analyze a problem as if it were a System. In this case, the investigated system is the Multirisk. The RES approach requires the identification of the system parameters and, in this case, a relative coarse interaction matrix was employed by using the Geohazards as parameters. In the related Matrix (Table 5.7), six scores have been assigned to define the influence of one parameters on the others (Causes, along the rows) and, vice versa, the influence of the other parameters over the examined parameter (Effects, along the columns). The score varies from 0 (absolutely no interaction between the two parameters) up to 3 (heavy influence of a parameter on the other).

Table 5.7: Interaction Matrix for the calculation of the Interactivity [%].

				Causes
	Flood Hazard	3	3	6
	2	Landslide Hazard	1	3
	1	2	Sinkhole Hazard	3
Effects	3	5	4	

These scores were assigned based on a heuristic approach. After attributing the cause and effect scores to the parameters, they were plotted in the Cause-Effect Diagram (Figure 5.29) to obtain additional information about the Multirisk system. In this case, the parameter that describes the flood hazard appears to be the only dominant parameter in the system. Landslide and Sinkhole Hazards, on the other hand, fall within the subordinate parameter area of the Causes-Effects diagram. It does not appear to be any substantial difference on the interactivity of the parameters. In table 5.8, the quantitative value of the Interactivity is calculated (in %). For the last steps of the project, presence/absence maps of the three geohazards have been produced (H0 = 0; H1+H2+H3+H4 = 1). These maps (Figures 5.30 to Figure 5.32) were multiplied by the respective interactivity value of each geohazards, obtaining an Interactivity Map for each parameter. By adding up these maps, the Multihazard Interactivity Map has been

obtained (Figure 5.33). The map was divided in classes using the Natural Breaks method (Jenks, 1977) from Very Low to Very High Interactivity.

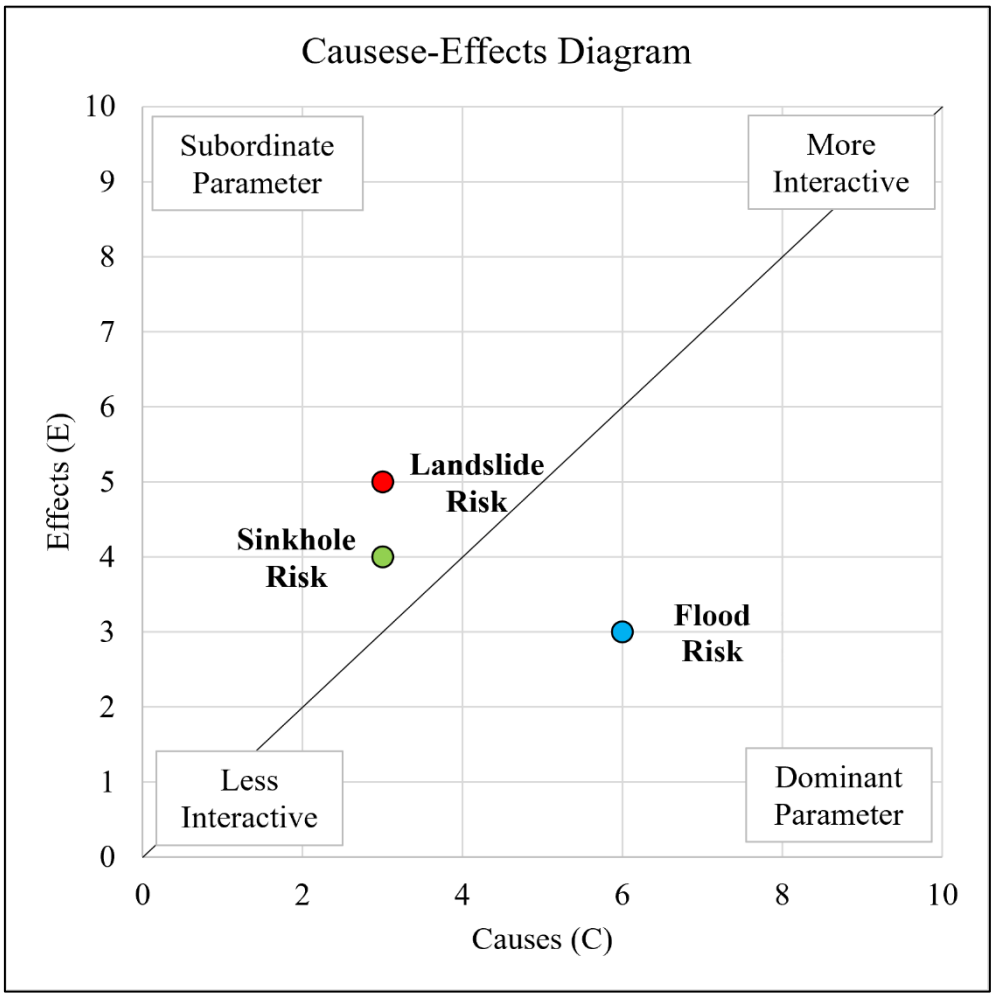

Figure 5.29: Causes-Effects diagram.

Table 5.8: Causes, Effects and Interactivity of the parameters (Geohazards).

Parameter	Causes	Effects	C+E	Interactivity I [%]
Flood Risk	6	3	9	37.5
Landslide Risk	3	5	8	33.3
Sinkhole Risk	3	4	7	29.2

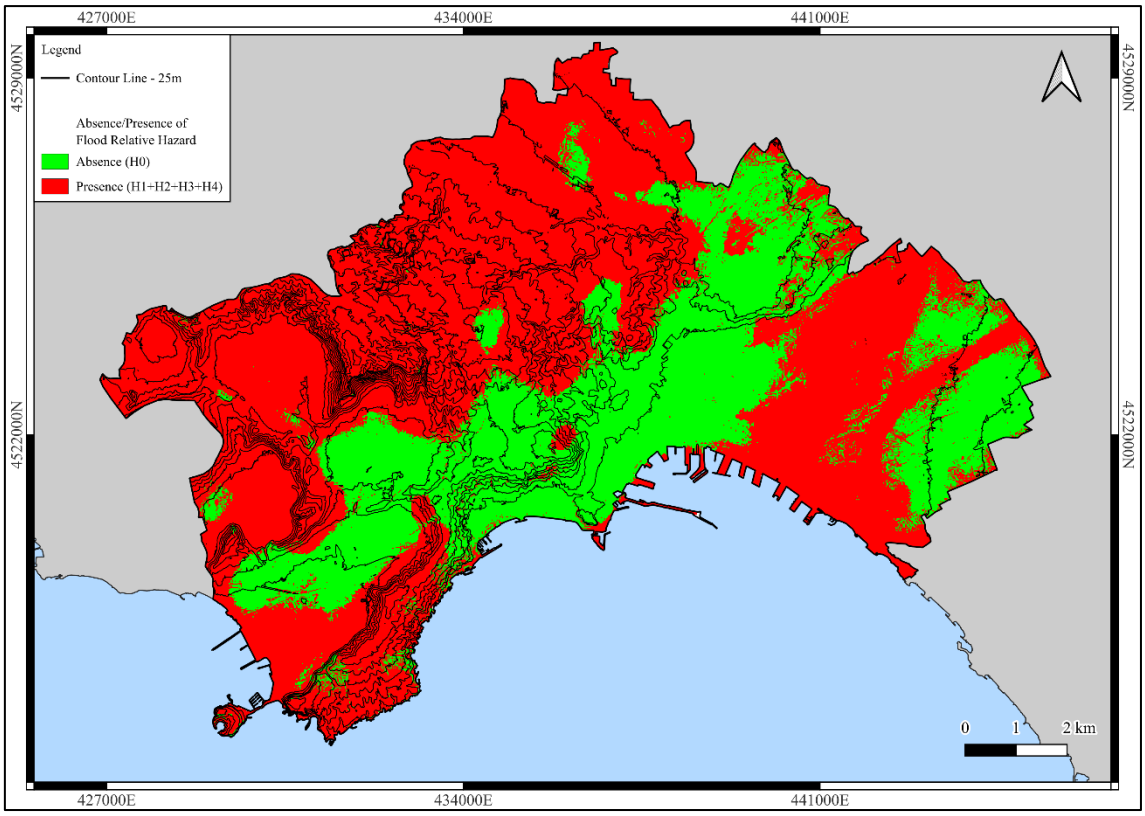

Figure 5.30: Absence/Presence map of Flood and Relative Hazard.

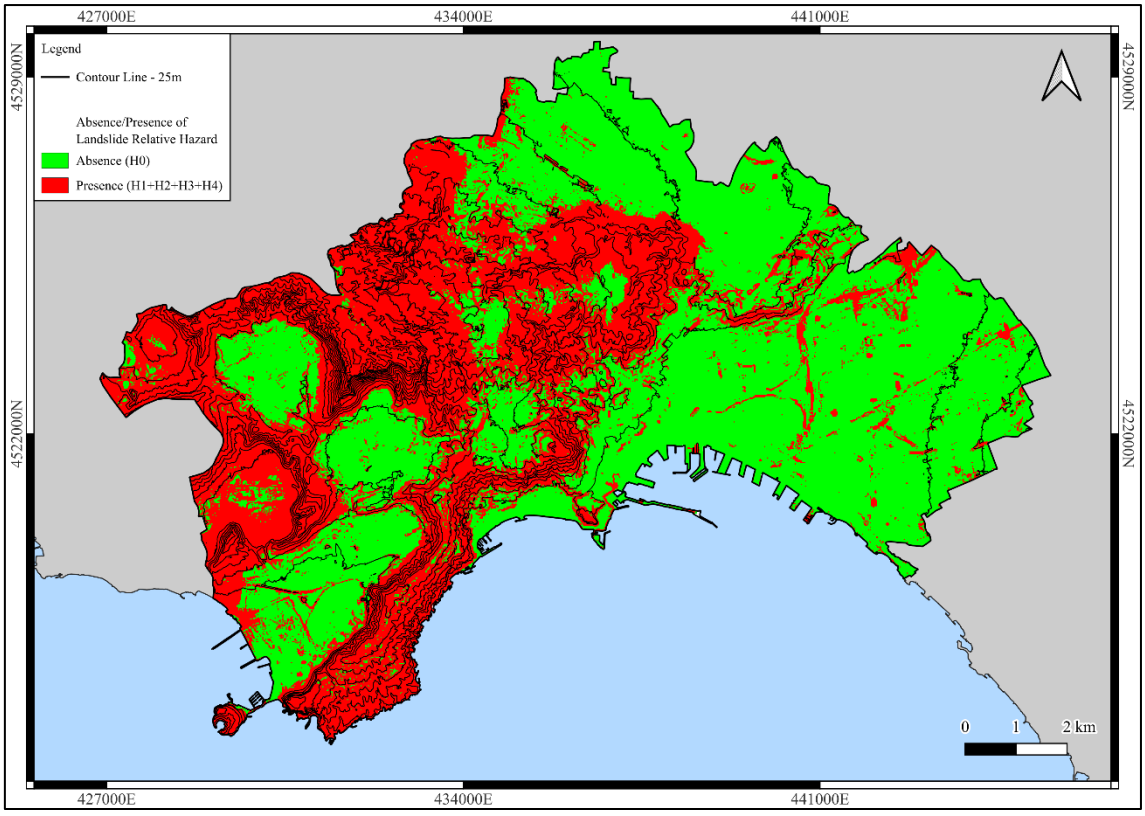

Figure 5.31: Absence/Presence map of Landslide Relative Hazard.

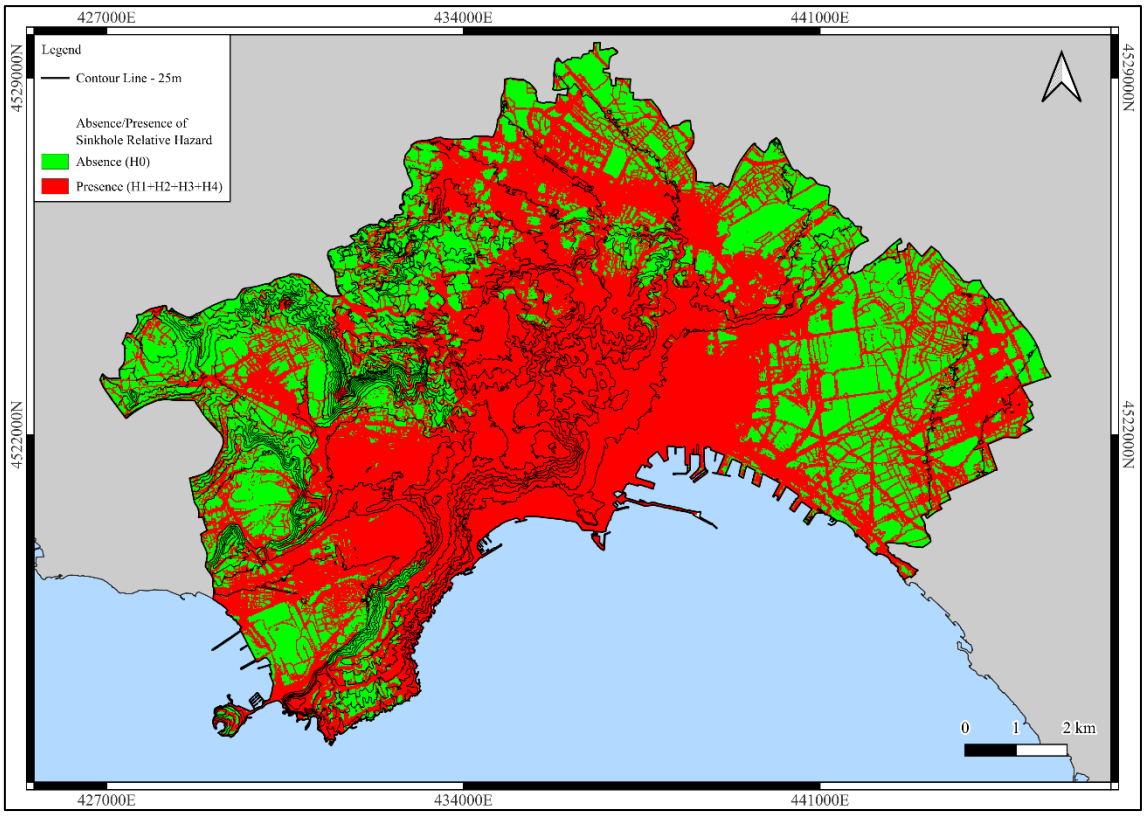

Figure 5.32: Absence/Presence map of Sinkhole Relative Hazard.

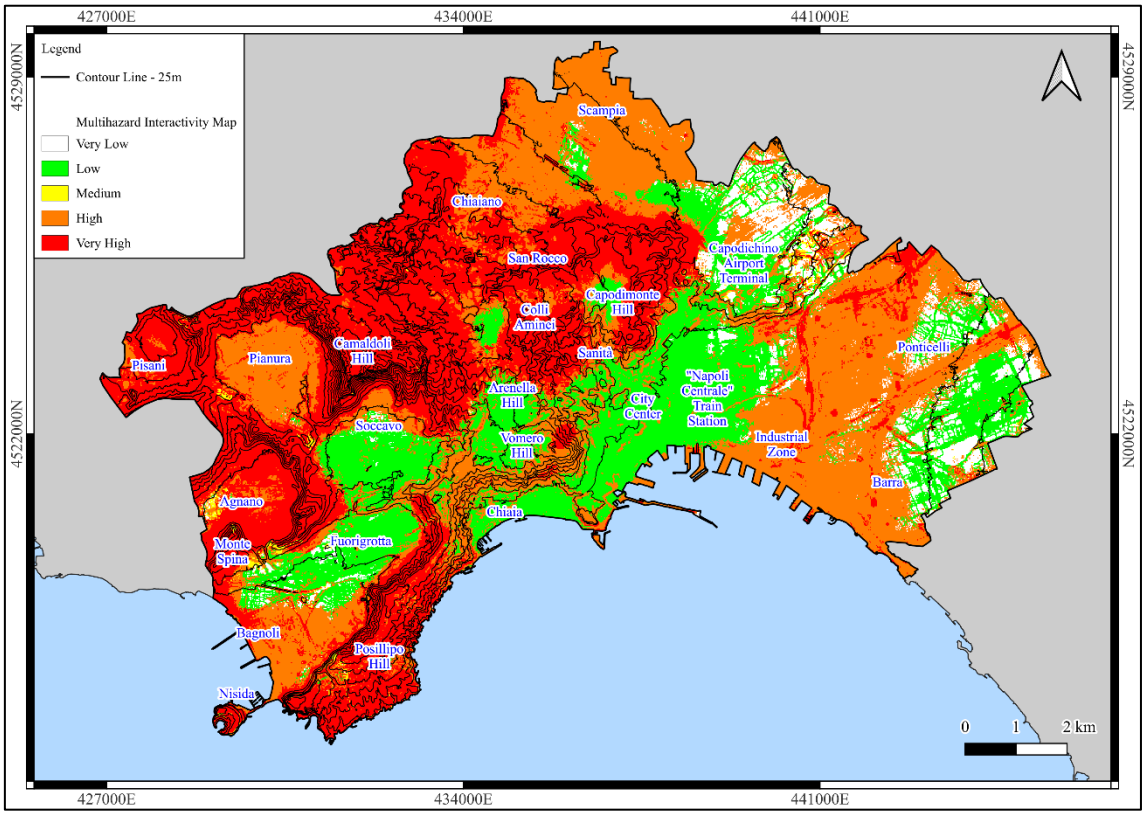

Figure 5.33: Interactivity Map of the city of Naples, classified using the Natural Breaks method (Jenks, 1977).

As shown in Figure 5.33, the eastern sector of the city is interested by Low, High and Very High Multihazard Interactivity. The northern sector of the city, the *Pianura* and *Bagnoli* Plains, and the hillslopes along the city center are characterized by High Multihazard Interactivity. The *Capodimonte*, *Arenella*, *Posillipo*, and *Camaldoli* hills and the areas of the *Chiaiano* quarries, *Agnano* and *Pisani* also fall within the Very High Multihazard Interactivity. The area of the Airport is only partially impacted by High Multihazard Interactivity, while the remaining areas fall mostly within the Low or Very Low Multihazard Interactivity.

By combining this product with the Damage map using the Risk Matrix (Table 5.5), the Multirisk Map of the City of Naples was obtained (Figure 5.34). The High and Very High Multirisk classes are located along the main hillslopes of the city (*Camaldoli*, *Vomero*, western side of *Posillipo*, *Capodimonte* and *Colli Aminei*). The High Multirisk class areas also include *Pianura*, the *Agnano* Plain and *Pisani*. The *Agnano* Plain itself appears to be impacted by Very High Multirisk along the road network. Medium and Low Multirisk affect the areas of *Soccavo*, *Bagnoli*, *Fuorigrotta*. As for the Central and northern section of the city, the *Chiaia* Neighborhood, the city centre, most of *Vomero* and *Arenella* Hills are impacted by Medium and Low Multirisk. As for the *Capodichino* Airport and the "*Napoli Centrale*" train station, these strategic infrastructures also fall within the Medium and Low Multirisk. High and Very High Multirisk characterize the areas along the hydrographic network (*Vallone San Rocco*, the *Camaldoli* hydrographic network), the hillsides, and the *Chiaiano* quarries area. The A56 Highway along the hillsides of *Capodimonte* and *Colli Aminei* also falls within the Very High Multirisk class.

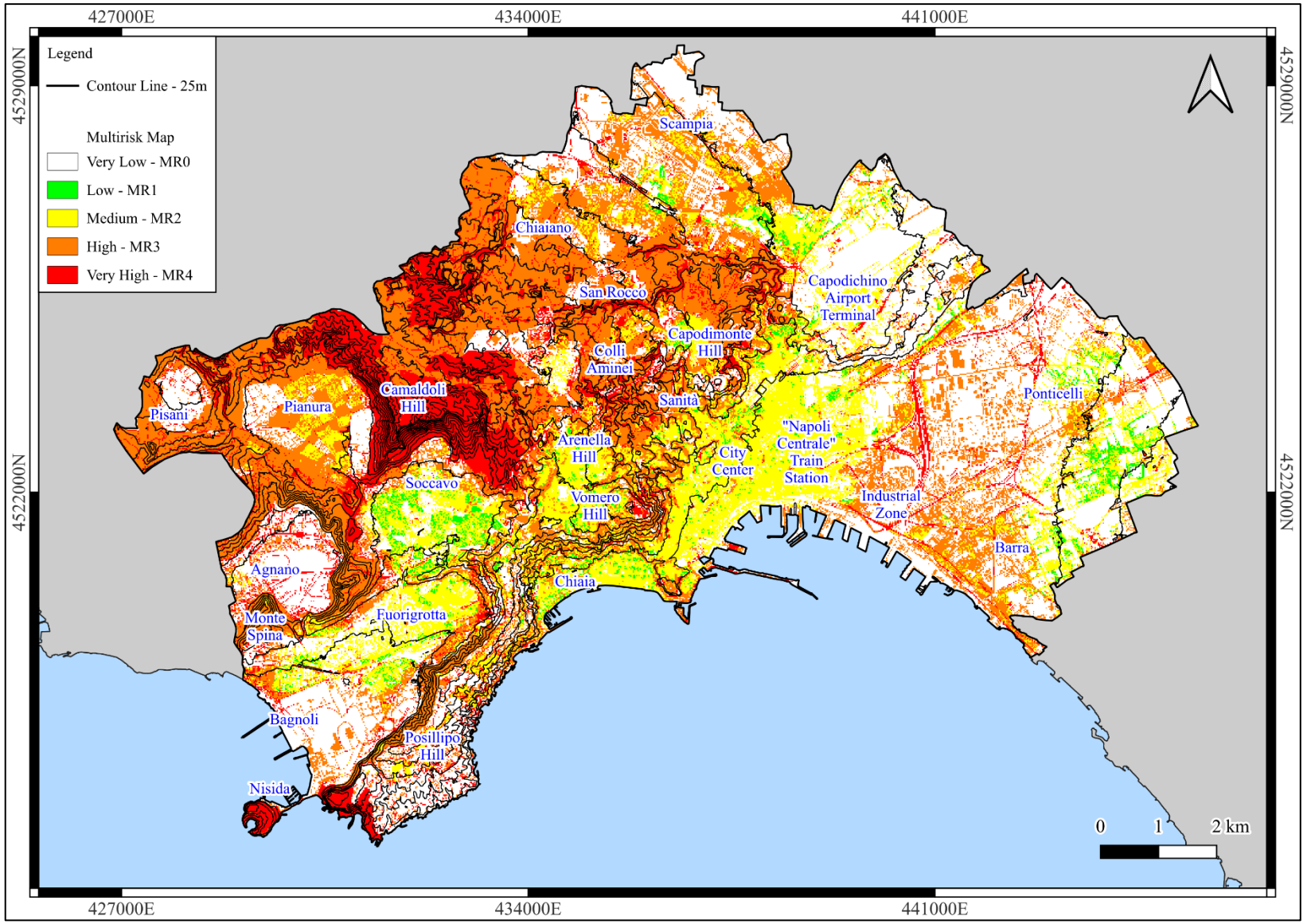

Figure 5.34: Multirisk map of the city of Naples.

6. DISCUSSION

During the first phase, the update of the inventories used as presence data for the MaxEnt and RF algorithms achieved two objectives: (i) validation of the inventories dataset and/or (ii) adding new data to the inventories as to increase the statistical meaning of the analysis. This is a crucial part of the first phase of this study as the occurrence inventory is, in fact, required to train, validate, and test the ML models. The three inventories used in this study have been obtained through different methods. The Landslide Inventory from Fusco et al. (2023) was obtained by uniforming and updating data from three different sources: (i) landslide inventories from the Units of Management of the *Campania* Region (now Southern Apennine Hydrological District); (ii) the Italian Landslide Inventory (IFFI); (iii) literature data. This inventory was produced through three main steps: (i) gathering the data from different sources; (ii) merging of the data and first validation; (iii) uniforming process of the landslide types, sometimes even modifying the data due to the presence of new, updated, information. In the case of highly urbanized areas, as it happens in Naples, landslides often leave little to no trace behind. This is why a relative high amount of landslide type is undefined (35%). During this phase, different available data were used to evaluate and update the existing inventory:

- Year of occurrence, to obtain information about the existing conditions at the time of the occurrence;
- Optical imagery, for example Google Earth optical images;
- Lithology;
- Slope angle;
- Old aerial photography, useful for old landslides that could have occurred before the anthropization of a hillside.

All the landslide data from the inventory were, eventually, updated or validated (Figure 5.3). Similarly, the sinkhole inventory published by Tufano et al. (2022) was updated, which

started from the inventory published by Guarino and Nisio that contains data that start from 1890 and reaches 2011, with 168 mapped sinkholes (188 in total). The update of the Sinkhole Inventory has been performed as part of this research project. Different sources have been used to fill the gap between 2011 and 2023, from national and local newspapers, to local authorities reports, and field work (Figure 6).

Figure 6.1: Ospedale del Mare sinkhole (08/01/2021). Photo by Giuseppe Bausilio.

Lastly, the as there is no available flood inventory for the city of Naples, a sampling of the Flood Hazard Map from the Unit of Management *Regionale Campania Nord Occidentale*, based on hydrodynamics analysis, was performed. This technique has been already used in literature with good results (Allocca et al., 2021) although, in this case, this method was not used to increment the sample population but to obtain a new presence dataset.

From the VIF analysis (Figure 5.8 and 5.9), the DTM and the EGMS_E seem to be affected by collinearity problems. As for the EGMS_E, it is likely that this is due to the

Phlegrean Fields uplift heavy influence, causing both EGMS_E (Figure 6.2) and EGMS_U (Figure 6.3) to show collinearity issues.

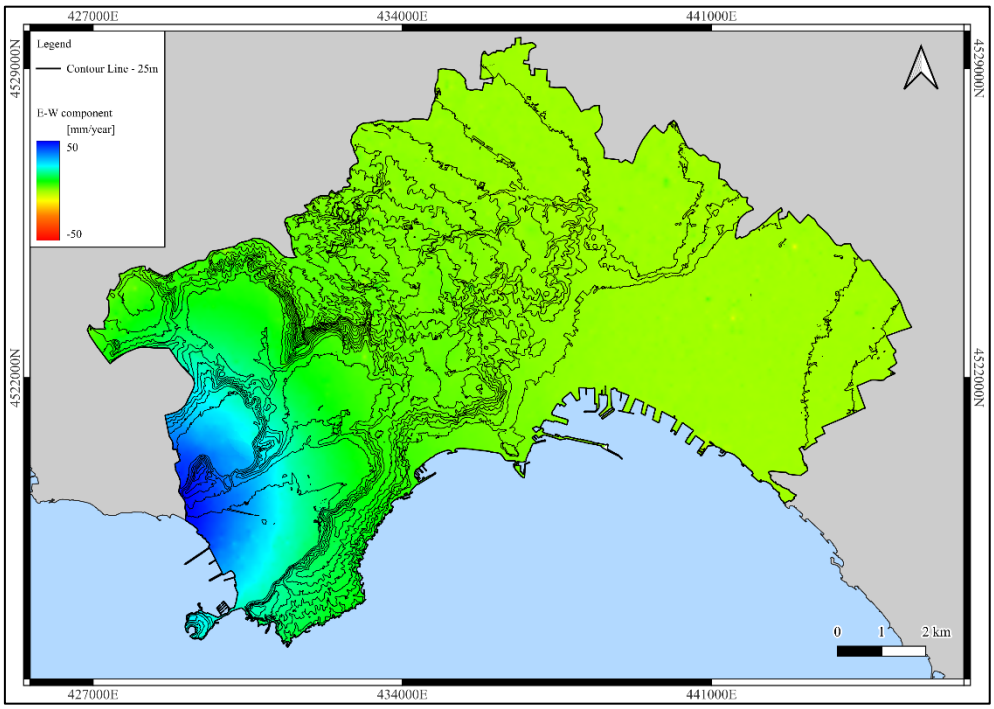

Figure 6.2: Horizontal (E-W axis) component of the interferometric data. Interferometric data from the European Ground Motion Service (Costantini et al., 2021).

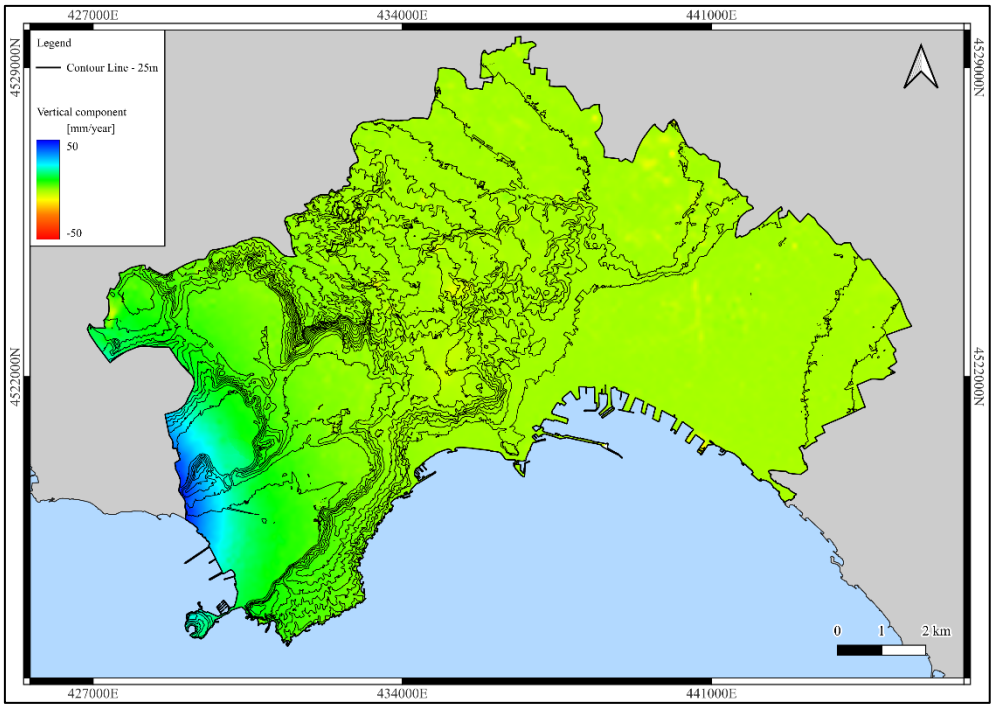

Figure 6.3: Vertical (z axis) component of the interferometric data. Interferometric data from the European Ground Motion Service (Costantini et al., 2021).

As for the DTM, it is probably due to the other predisposing factors that are derived from the DTM itself (Slope angle, Aspect, Planar Curvature, Profile Curvature, Topographic Position Index, and Topographic Wetness Index). Finally, the groundwater data collinearity problems are probably due to the general similarity between DTM and groundwater data as both of them increase from 0 m a.s.l., next to the seaside, to their maximum values towards the hinterland and the *Camaldoli* Hill. The Elements at Risk were obtained by over imposing the five different layers (Figure 5.10 to 5.14) and attributing to every cell the highest value of Elements at Risk. In the western and northern sectors (Figure 5.15), the presence of large homogeneous polygons belonging to the Medium, High, and Very High classes seems to indicate a strong effect of the natural reserve (Figure 5.12) layer on the Damage Map. In the remaining sectors of the city, most High and Very High extended polygons are related to railways and strategic buildings or roads (Figure 6.4).

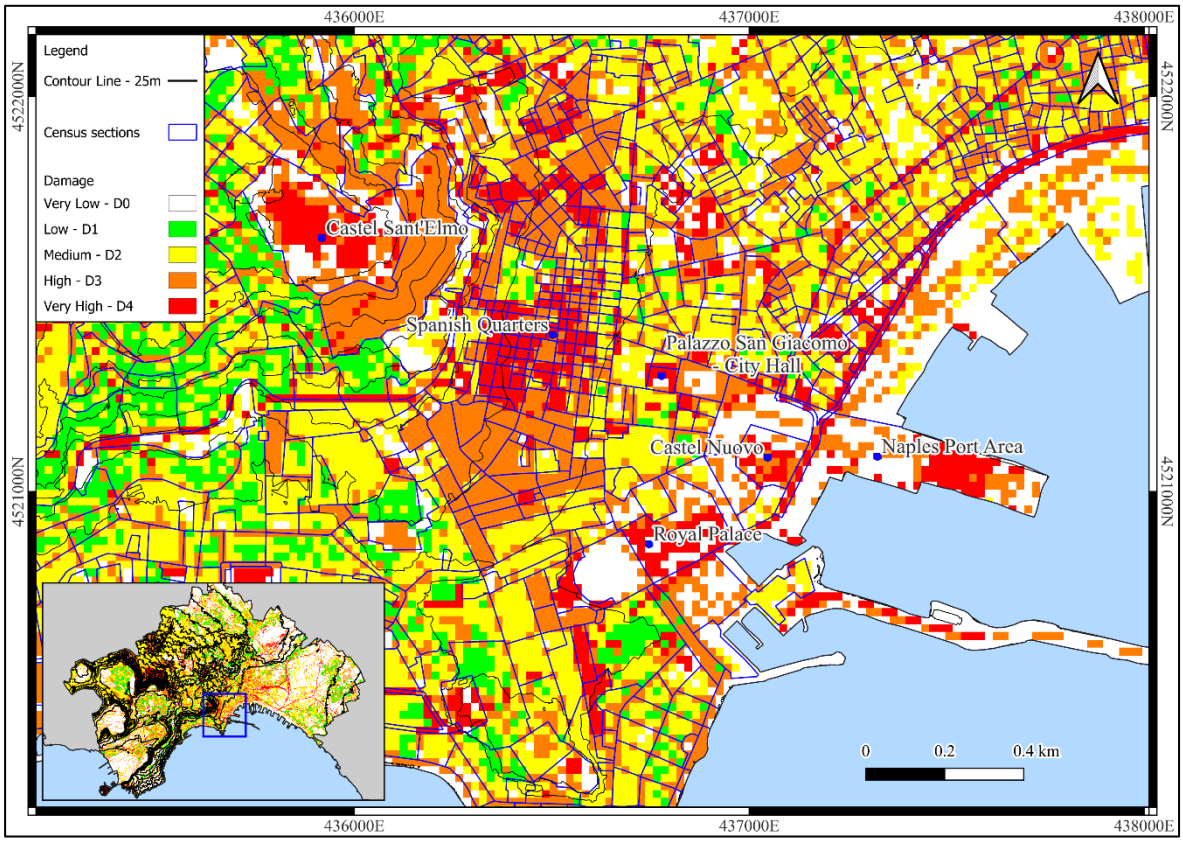

Figure 6.4: Detail of the Damage map. The area in the map is represented by the blue square in the inlet map.

The employed ML algorithms (RF and MaxEnt) have shown constant good performance (Table 5.2). Out of the 45 models, the average ROC/AUC scores obtained show that all three products have achieved great performance (Table 5.3) and most of them fall above the threshold (0.85) for the following EM analysis (Figure 5.19). Generally speaking, it seems that the RF algorithm has achieved better performance overall, although with a higher standard deviation in two out of three Relative Hazard assessment (Landslide and Sinkholes).

Except for seven Sinkhole Relative Hazard models (four RF models and three MaxEnt models), all the models were employed for the EM analysis. The total elaboration time required for these analyses was, on average, of about 4 hours using an Intel® i7-10750H CPU @ 2.60GHz, 16 GB of RAM, and NVIDIA GeForce RTX 2060 GPU laptop. The obtained Relative Hazard maps were divided into 5 classes using the Natural Breaks method (Jenks, 1977), from Very Low (H0) to Very High (H4). In all three Relative Hazard maps, the classes areal extensions (Table 6.1) show a decreasing trend (Figure 6.5), while the Presence data frequency per class (Table 6.2) shows an increasing trend (Figure 6.6).

Table 6.1: Class areal extension of the different Relative Hazard maps.

Geohazard	Classes areal extension [%]				
	Very Low - H0	Low - H1	Medium - H2	High - H3	Very High - H4
Flood	34.1	30.8	21.0	9.9	4.2
Landslide	54.9	20.6	11.9	7.6	5.0
Sinkhole	37.3	26.4	18.0	10.9	7.4

Table 6.2: Presence data frequency per class.

Geohazard Presence data	Class Frequency [%]				
	Very Low - H0	Low - H1	Medium - H2	High - H3	Very High - H4
Flood	0.5	1.3	5.5	11.0	81.7
Landslide	0.5	2.0	8.1	16.7	72.7
Sinkhole	0.5	1.2	7.2	22.5	68.6

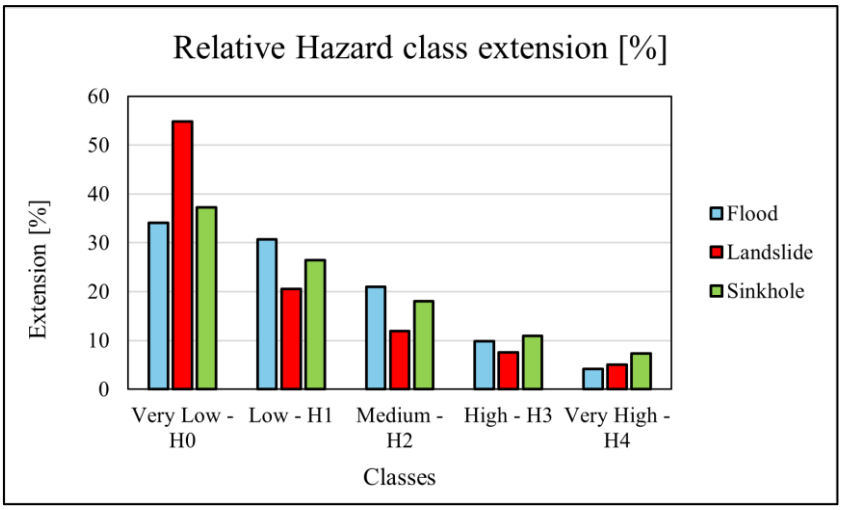

Figure 6.5: Areal extension of the different classes in the Relative Hazard maps.

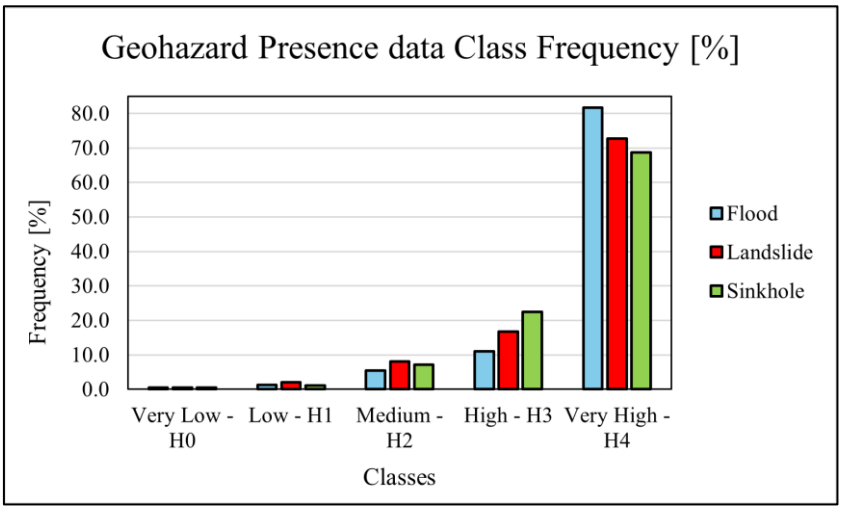

Figure 6.6: Histogram of presence data frequency in the five different classes.

The Flood Relative Hazard map (Figure 5.20) is characterized by the presence of High and Very High areas localized at the foot of the hills and in the plains (western and eastern sectors of the city). Generally, the higher classes are also located wherever the contour lines are widespread, rarely even along the hillslopes. Although the presence-only inventory was composed mainly of points located in plain areas or at the foot of the hills (Figure 5.7), some areas along the hillslopes have been characterized by High or Very High values of Flood Relative Hazard. By studying the permutation importance for Flood Relative Hazard modelling (Table 5.4), it is clear that this is mostly due to the heavy weight of the Hydrographic Network Distance predisposing factor in the model. As most presence points from the flood pseudo-

inventory were located either along channels (*Vallone San Rocco* – San Rocco Valley and the hydrographic network in the northern and eastern sections of the city) or at the end of the hillslope canals, the model obtained has given great importance to the Hydrographic Network Distance predisposing factor. It seems like the Flood Relative Hazard map obtained could be reinterpreted: this model has not only modelized the flood geohazard but also the hydraulic erosion, transport, and deposition (hereafter HETD) processes along the channelled hillslopes. This is a great example of why tools like ML algorithms must still be accompanied by an in-depth interpretation phase of the results, as to avoid possible misinterpretations. The eastern section of the city is also characterized by the presence of the High and Very High classes in correspondence with the local channels (*Lagno di Trocchia* – Trocchia Channel and *Fosso Cuzzone* – Cuzzone Canal). In the northern part of the city, the higher classes are located along the *Vallone San Rocco*, the hydrographic network on the northern side of the *Camaldoli* Hill, the *Chiaiano* neighbourhood and along the channels located north-east of *Chiaiano* that form a natural border between the Naples and *Melito* (*Lavinaio di Melito*).

As for the Landslide Relative Hazard Map, the Slope Angle and distance from the Hydrographic Network high influence (Table 5.4) were excepted. On the other hand, the Road Density being showcased as more important than the Road Distance (as roads usually represents cuts along the hillslope) was not expected. This is due to the values' importance within the variable. The analysis of the road density predisposing factor contribution showcases that higher landslide Relative Hazard is not related to road network high density values, but to the lower ones. In order to prove this theory, an evaluation of the Landslide Relative Hazard was performed using the MaxEnt software (Phillips et al., 2023). One of the products of the software are the response curves for the different predisposing factors. As shown by the Road Density response curve (Figure 6.7), the high importance of the aforementioned predisposing factor is

most likely related to the higher presence of the lower values of Road Density along the hillslopes (Figure 6.8).

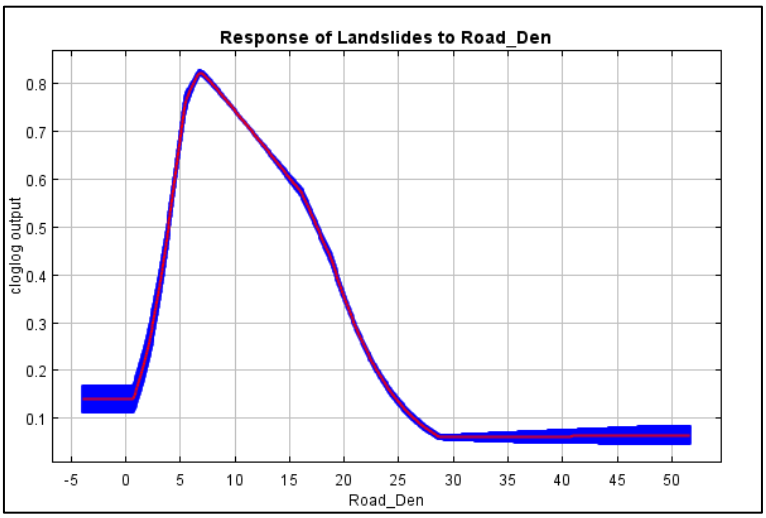

Figure 6.7: Response curve of the Road Density predisposing factor. Red line is the mean values obtained from 5 iterations, the blue area represents the standard deviation. Diagram produced using the MaxEnt software (Phillips et al., 2023).

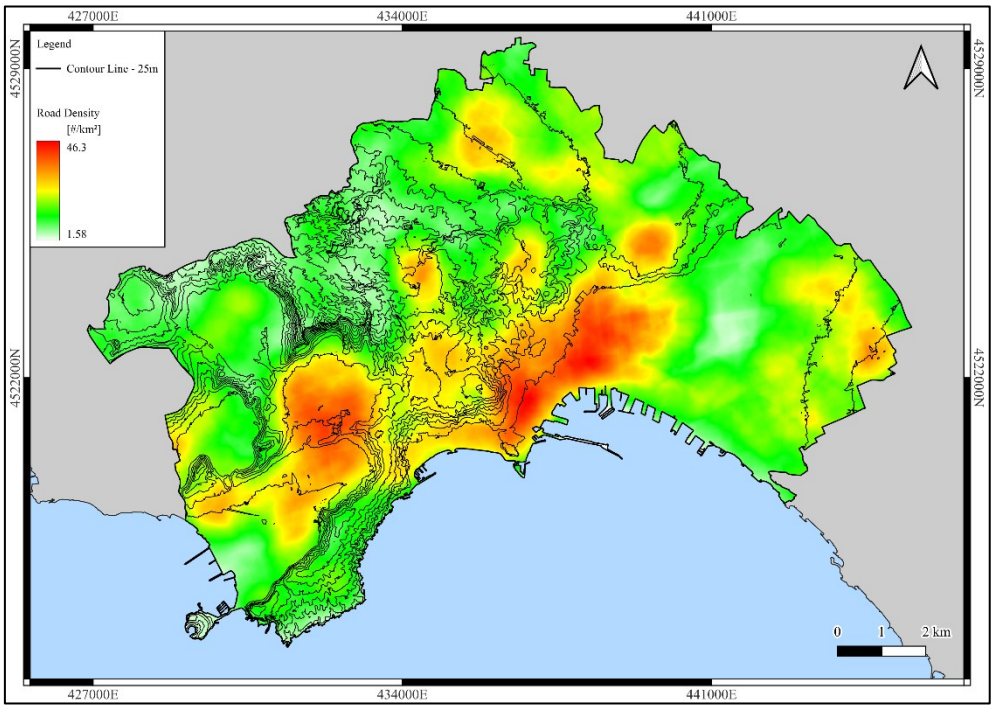

Figure 6.8: Road density map of the City of Naples.

The High and Very High classes related to the Sinkhole Relative Hazard map are mainly located in the historical city centre and the *Vomero*, *Arenella* and *Posillipo* hills. The four most important predisposing factors seem to be (i) the road network distance, (ii) the distance to aqueduct and sewer main networks, (iii) the distance to underground cavities, and (iv)

hydrographic network density. The relationship between the latter and Sinkhole Relative Hazard is linked to the lower values of the hydrographic network density (Figure 6.9). This is because the highest values of hydrographic network density are mainly located along the northern hillside of the *Camaldoli* hill and along the *Vallone San Rocco*. The road network distance, the aqueduct and sewer networks distance, and the underground cavities distance are directly linked to the presence of underground voids. In particular, the roads are often related to the underground secondary aqueduct and sewer network (which are not represented in the AS_Net predisposing factor that contains only the main network), while the underground cavities are related to tunnels excavated for different purpose throughout history and often converted to collectors, cisterns, or even bunkers. The eastern and the western sectors of the city seem less affected by sinkhole Relative Hazard, except along the roads (Figure 5.22).

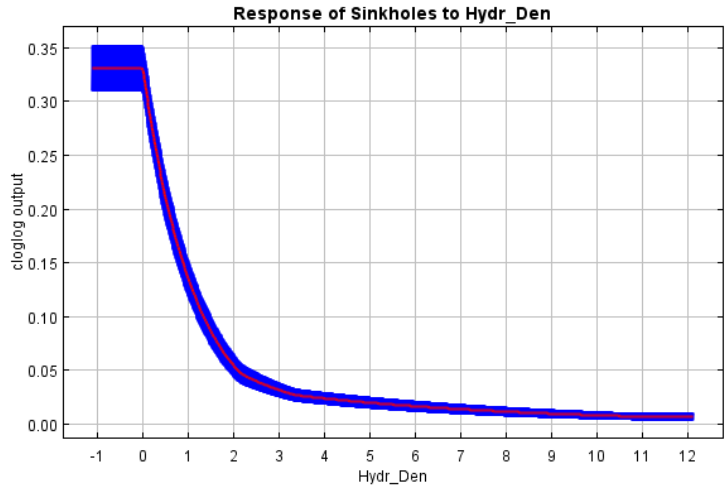

Figure 6.9: Response curve of the Hydrographic Density predisposing factor. Red line is the mean values obtained from 5 iterations, the blue area represents the standard deviation. Diagram produced by the MaxEnt software (Phillips et al., 2023).

The EM performance scores were obtained by testing the 30% of the inventory data that has been kept out of the training phase since the start of the process. This is an approach employed in order to avoid any positive bias on the performance score that could have been derived from the use of the training data itself in the test stage. These results appear to be better than the average of the models (Table 5.3). This confirms the reliability of the EM approach in Relative Hazard assessment problems.

In the following step, the Risk assessment, the Risk Matrix from Table 5.5 was used instead of the one in Table 5.6. This choice was made due to the possibility that, by using the matrix in Table 5.6) there could have been cases of Medium Landslide Risk in Plain areas caused by the presence of a Very High Damage area. This would have been an unrealistic modelization of reality. According to the results obtained after combining the Relative Hazard Maps with the Risk Matrix, it seems like the Very High Flood Risk linked to the eastern sector of the city is related to the presence of railway tracks and strategic roads like *Via Argine*, Highways A3 and Highway SS162. The last two connect Naples with the rest of the Campanian region. In the central and northern sections of the city, the areas most affected by the Flood & HETD Risk are *Vallone San Rocco* (San Rocco Valley) and other secondary channels, Highway A56, Provincial Road SP500, the *Chiaiano* neighbourhood and the quarries. In this case, too, the Highway and the Provincial Road are both essential infrastructures for the city. As for the western section of the city, the highest risk classes are located along the portion of the Highway A56 located in the *Agnano* neighbourhood. On top of that, the areas at the foot of the *Camaldoli* and *Pozzuoli* Hills are also characterized by Very High Flood & HETD Risk. High and Very High Landslide Risk characterize the slopes of the *Camaldoli* Hill, the northern side of the *Posillipo* Hill. Within the western sector of the city, the slopes around the *Agnano* Plain and the ones in the *Pisani* area are also affected by High Landslide Risk, while in the central and northern sector, the highest risk classes are located along the slopes of the *Vomero* Hill, *Materdei*, along the *Vallone San Rocco* and the *Chiaiano* quarries general area. In the eastern sector, Landslide Risk seems to interest only local areas along the main roads like *Via Nuova Poggioreale*, *Via Stadera* and Highway A1, also called *Autostrada del Sole* – Highway of the Sun. Anthropogenic Sinkhole Risk is characterized by a radial distribution: the High and Very High classes are widespread all over the city centre, especially at the foot of the *Vomero* Hill (the so-called *Quartieri Spagnoli* – Spanish Quarters). It seems like sinkholes the only

geohazard to impact the Airport area and, to a lesser extent, the main Train Station area. Generally speaking, High and Very High Sinkhole Risk also impact the road network of the City Hills (*Vomero*, *Colli Aminei*, *Rione Alto*) and Highway A52. The only hillside that seems to be involved in sinkhole risk is the southern portion of *Posillipo* Hill, which is highly urbanized and characterized by a well-developed road network. As expected, the Risk Matrix showed in Table 5.5 limited the potential heavy influence of the Damage map. In particular, even though the *Camaldoli* hillside is characterized by the highest Damage class, the Sinkhole Risk map was not influenced by it. In case it was used a more traditional Risk Matrix (Table 5.6) the aforementioned hillslope would have fall within the Medium Risk class. An unexpected result as it would imply a moderate presence of anthropogenic sinkhole on a Natural Reserve hillslope. On the same note, using the traditional Risk Matrix, the Airport Terminal and the "*Napoli Centrale*" train station (Figure 4.3) would have fall within the Medium Landslide Risk class even though both structures are located in plain areas. Lastly, the Natural Reserve influence is clear along the hillslopes in the western and northern sections of the Flood & HETD and Landslide risk maps, as shown by the presence of High and Very High Risk areas.

The last phase of this project is the evaluation of the geohazards influence on each other through the use of a Multirisk approach. As stated by different authors (Selva, 2013; Gallina et al., 2016), the multirisk evaluation approaches can be separated into two main categories: i) those that focus on the evaluation of a true multihazard/multirisk, including the "cascade" effect, and ii) the approaches that evaluate what could be more correctly defined as "multiple hazard/risk", when the possible interaction between geohazards is not considered in the analysis. Multiple studies have been conducted during the years on different urban areas all over the world, most of them different from each other, as there is no definite methodology.

Regarding Naples, there are other examples in the literature of multirisk evaluation within the city. In particular, Marzocchi et al. (2012) evaluates the multirisk from a probabilistic

approach in the *Casalnuovo* municipality (part of the Metropolitan City of Naples). In their study, the authors evaluate the geohazards impact on each other, starting from the very foundation of their methodology: the events catalogue. Using a complete and detailed catalogue that also contains information about past interactions between different hazards (volcanic eruption, earthquake, flooding, landslide and industrial risk), an evaluation of the possible "cascade" effect was performed. It is a very detailed approach that requires an in-depth knowledge of the geohazards in a study area, allowing the characterization of specific "cascade" effects (specifically, Industrial risk affected by volcanic activity).

Barría et al. (2019) also evaluated the multirisk for the coastal cities of Chile. Their approach consisted in the Risk evaluation for every geohazard (flood, earthquake, tsunami and landslide) as product of the exposure to the geohazard and the vulnerability. The latter was not evaluated from an economic point view, but by giving a weight score to the different categories of elements at risk (housing, facilities, infrastructures). The multirisk assessment, although, did not consider the "cascade" effect, as the final product is obtained by overlapping the risk map of every hazard evaluated singularly. Similarly, Johnson et al. (2016) evaluated the risk for three different hazards (heat waves, typhoons and landslides) in two Hong Kong districts. The methodology includes an analysis of the vulnerability based on population, rather than buildings or type of land use. In this case vulnerability evaluation consider, for every subdivision of the study area, the amount of people (percentage of the total population of Hong Kong) and some statistical population data like i) percentage of population under age 5; ii) percentage of population over age 35; iii) percentage of unemployed; iv) income; v) percentage of population based on their minimum educational degree and vi) percentage of households with single inhabitants. After the hazard assessment phase and the risk evaluation (as the product of Hazard and Vulnerability), the multirisk map is obtained by overlaying the three hazard maps, without considering the "cascade" effect.

Lastly, a different approach from the above-mentioned ones is the one presented by Mascheri et al. (2024) applied to an area of the city of Lisbon. The authors evaluate the multirisk as a sum of economic losses related to the flood and earthquake geohazards. In particular, the authors highlight the different type of impact that the two geohazards exert on the buildings, producing two different vulnerability maps on top of the two geohazard maps.

Regarding this project, the employed multihazard approach starts from the Interaction Matrix. The following table (Table 6.3) describes the meaning behind the scores assigned in Table 5.7. The last column and row of the Interaction Matrix contain the sum of Causes and Effects scores for all the parameters. These scores are used in the Cause-Effect diagram to describe the behaviour of the parameters within the System.

Table 6.3: Expanded version of the Interaction Matrix, based on operators' expert judgment.

				Causes
	Flood & HETD Hazard	Floods can cause either imbibition of slope materials, degrading its geotechnical properties and causing a flow-like landslide, or cause foot erosion along slopes and consequential fall/topple/slope landslides.	Flood events can trigger/accelerate underground erosional events or degrade the geotechnical characteristics of the cavity roof materials, causing collapses and triggering sinkholes.	6
	Landslides can obstruct a stream, causing localized water accumulation.	***Landslide Hazard***	Landslides can be the triggering event of the subsidence/collapse phenomenon when thelandslide that affects a cavity could cause a cavity roof collapse or when the displaced material would impact an area above an underground cavity, causing a collapse.	3
	The presence or formation of a cavity can represent a collection point for rainwater.	The edge of relatively large collapse sinkholes is made of scarps. Along these scarps, there could be landslide initiation.	***Sinkhole Hazard***	3
Effects	3	5	4	

The Flood & HETD parameter was assigned the maximum Causes score over both the Landslide Hazard and the Sinkhole Hazard parameters. This is mostly due to the degenerative effect that a great amount of water can apply on the geotechnical parameters of the materials, lowering, for example, the resisting forces. On top of that, running water can cause erosion of geological materials, causing the creation of underground voids or foot erosion. On the other hand, the effect of other parameters on the Flood & HETD geohazard is limited: landslides could obstruct a stream, allowing a localized water accumulation, while sinkholes can generate a depression (caused by either collapse or subsidence) that could represent a collection point for run-off water.

Moving on to the second parameter (Landslide Hazard), the cause score attributed to Sinkhole Hazard is lower than the one attributed before for Flood & HETD hazard. A Sinkhole initiation could also trigger a landslide whenever the activated sinkhole is a relatively big collapse sinkhole: if the triggered phenomenon is vertically developed, the rim could be made up of possibly unstable walls. In these conditions, landslides could trigger along the scarps. On the other hand, the effect score attributed to the Sinkhole Hazard over the Landslide Hazard is even lower: a sinkhole could be triggered by a landslide whenever (i) the impact of the displaced material (a boulder from a rock fall, for example) would cause the collapse of an underground cavity or (ii) a landslide that affects a cavity could cause a cavity roof collapse.

The validation of the Interactivity values was experimentally performed, independently from the previous steps, using MaxEnt. An inventory of 500 random pseudo-presence points was extracted from the Relative Hazard areas of all three parameters (Figure 6.10). As predisposing factors, instead, three maps representing only the Very High Relative Hazard class of the three geohazards were used (Figure 6.11 to 6.13). In this case, the ML algorithm was performed to identify which of the three Geohazards is the more influential on a random sample of geohazard occurrences. The process was carried out using a 5-fold cross-validation approach.

The results showed that the most influential parameter was the Flood & HETD Relative Hazard, followed by the Landslide Relative Hazard and the Sinkhole Relative Hazard.

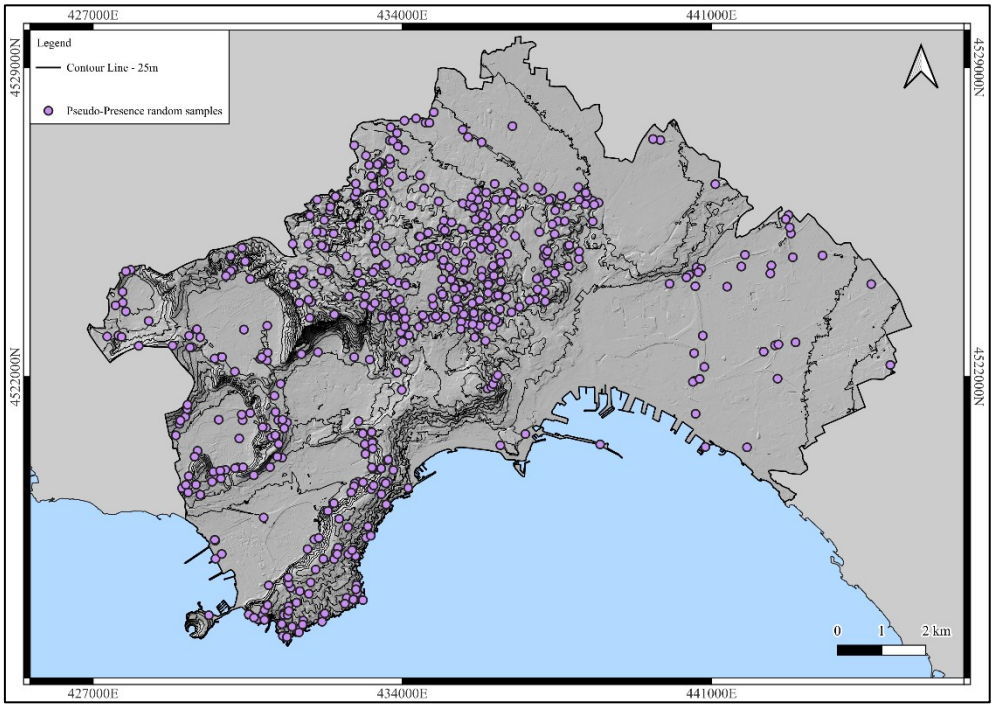

Figure 6.10: Pseudo-Presence random Samples for Interactivity score validation.

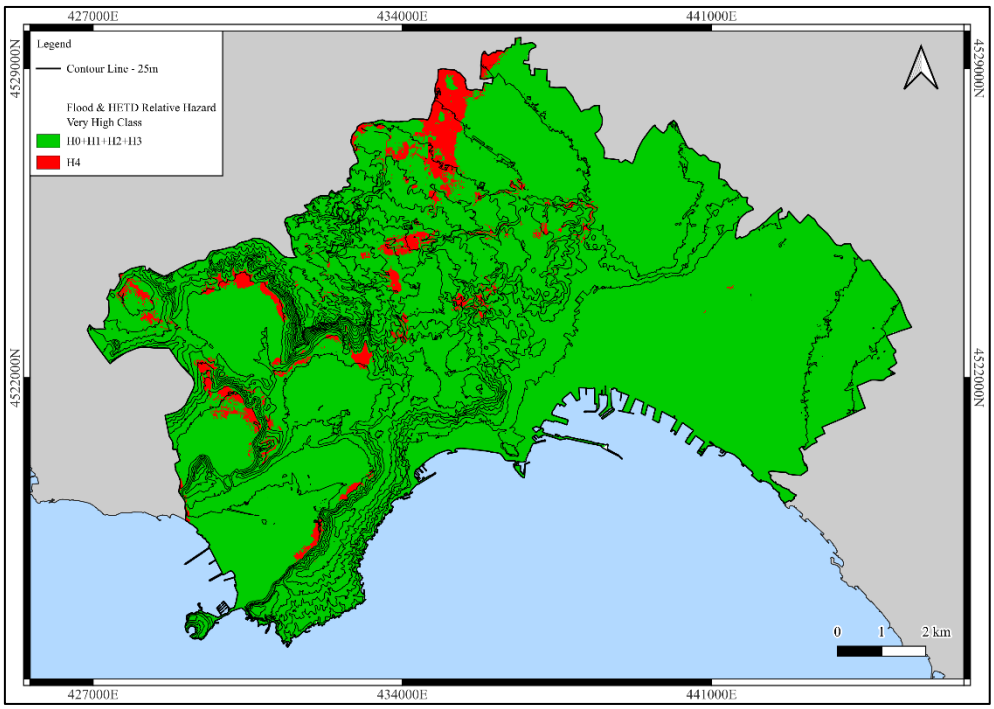

Figure 6.11:Very High Flood & HETD Relative Hazard.

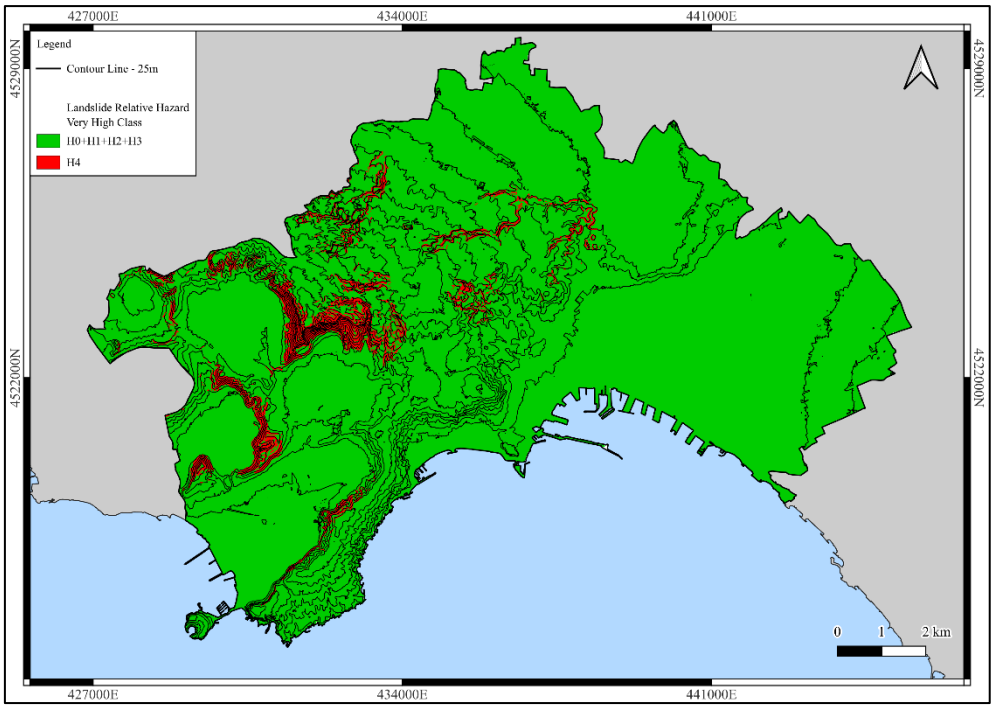

Figure 6.12: Very High Landslide Relative Hazard.

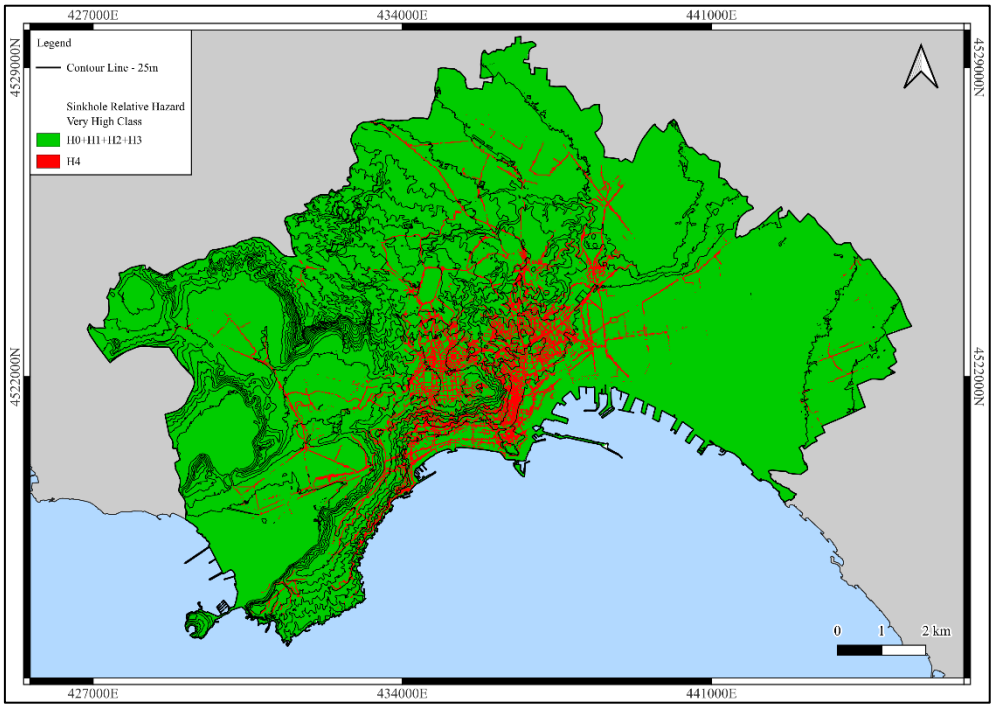

Figure 6.13: Very High Sinkhole Relative Hazard.

The following Table (Table 6.4) shows the permutation importance score of the three parameters. These data seems to support the scores attributed during the Interaction Matrix phase, which assumes that the Flood & HETD Geohazard is the most influential.

Table 6.4: Permutation importance for the parameters related to the pseudo-inventory of random points extracted in multi-hazard areas.

Parameter	Permutation importance
H4_Flood & HETD	52.8
H4_Landslide	32.6
H4_Sinkhole	14.6

After combining the Geohazards Interactivity Maps, the Multihazard Interactivity Map was obtained (Figure 5.33). The eastern sector of the city shows a clear distinction between the Highways (A1 and A3) and the railway tracks (strategic infrastructures) against the rest of the road network and the buildings. The former fall within the Very High Multirisk, while the remaining are included in the High, Medium, and Low Multirisk. What appears to be highlighted by the Multihazard Interactivity map is the high interaction between Landslide and Flood & HETD processes in the *Camaldoli* and *Capodimonte* Hills, *Chiaiano*, and the western sector of the city. In the eastern sector of the city and the *Pianura* neighbourhood, instead, Flood and Sinkhole Relative Hazards highly impact some main strategic infrastructures, railroads and highways, that connect the city with the rest of the *Campania* region. The remaining Low Multihazard Interactivity class seems to highlight the areas that are interested only by Sinkhole Relative Hazard (historic centre, *Fuorigrotta* and *Soccavo*). The final Multirisk Map (Figure 5.34) highlights the importance of the Damage map in the final product. The entire city centre is characterized by the Medium Multirisk, mostly due to the presence of strategic and historically and culturally important buildings. The railroad network and the Highways are also characterized by the Very High Multirisk class all over the city. Even so, the Natural Reserve highly impacts the Multirisk Map. The *Camaldoli* hill, the hillslopes along the *Pisani* and *Agnano* neighbourhood, *Monte Spina*, *Nisida* and the northern side of the *Posillipo* Hill fall within the Very High and High Multirisk classes. This was expected due to both the importance of the Natural Reserves and the effect of landslides on the Multihazard system (the second most interactive after the flood and HETD hazard).

The results show the importance of evaluating the relationship between geohazards, using a multihazard/multirisk approach, in this case employing the RES method. This is an important advantage of this methodology, as the "cascade" effect evaluation is recognized as a challenge in the literature (Komendantova et al., 2016).

In the context of the presented procedures, the shown methodology is a mixture of both approaches: we evaluate the multirisk starting from singular geohazard susceptibility assessment, combining these maps after weighing their impact in a "cascade" scenario through the RES approach. The RES approach has been already used in literature for multirisk analysis (Liu et al., 2015), demonstrating the good performance that this method can obtain in multirisk assessment.

It must be highlighted that, by using the RES, we limited some process automatization, as the approach now needs the direct intervention of an expert with deep knowledge of the study area. On the other hand, the implementation of the EM approach using ML algorithms in an R script allows high replicability and customizability (number of folds, sets of Pseudo-Absence points, etc.) for different study areas to obtain high performance geohazard susceptibility map. Although, due to the use of statistical methodologies during the susceptibility assessment phase, the geohazard inventories (presence dataset) are critical to the training, validation, and evaluation of the models. This dependency can sometimes be a limit, for example, in areas wherein the inventory is either unavailable or contains strong uncertainties in its spatial coordinates. An approach to overcome this limitation was presented in this thesis, as the flood inventory was obtained by sampling the flood hazard map from the Basin Authority. The results were acceptable but, as this pseudo-inventory lacked temporal occurrence information, a true hazard assessment was not feasible and the Relative Hazard (Parise, 2001) was employed. Finally, the vulnerability evaluation for an entire city is another recognized challenge in literature, making it a demanding, sometimes even problematic, step (Mastrantoni et al., 2023).

One of the most common vulnerability assessments in the literature is the estimation of the damage to buildings (Julià and Ferrerira, 2021; Mastrantoni et al., 2023) while, whenever economic and land value data are available from the local administration, in-depth study of vulnerability are performed either by analyzing the land-use (Grünthal et al., 2006). In this study, different elements at risk were considered (population, buildings, infrastructures and natural reserves). In this way, we evaluated in great detail the typology of goods that could be impacted by a geohazard, on the other hand, we could not attribute a degree of loss to all the elements at risk with the same detail, employing a cautionary approach to vulnerability assessment.

7. CONCLUSIONS

This research project starting point is the need to deepen the knowledge about geohazards interactions with each other. To evaluate this "*cascade*" effect, a Multirisk approach, the Rock Engineering System (RES) from Hudson (1992) was applied. It isn't easy to evaluate and model this kind of interactions, but the continuous expansion of the urban fabric all over the world requires an effort from the scientific community to give their contribution towards a more resilient urban planification to preserve the historical heritage, the socioeconomical fabric and, most importantly, human lives.

This study followed a three phases approach, using a remarkable amount of data but still achieving a simplicity of use that permits the application of this approach to different urban contexts. The three phases, summarized, are:

- Preprocessing phase – gathering data about the predisposing factors, the geohazard inventories and the evaluation of the Damage (Elements at Risk × Vulnerability);

- Risk assessment phase – using Machine Learning algorithms, the Relative Hazard for the different Geohazards is evaluated and combined with the Damage, using a risk matrix, to obtain the Geohazard Risk;
- Multirisk assessment phase – using the RES approach, the Geohazards are treated as parameters of a system and their impact is evaluated using the interaction matrix. Once the Geohazard impact has been characterized using the interactivity (I), the Multirisk interactivity map is produced and combined with the Damage, using the risk matrix, in order to produce the Multirisk map.

During the first phase of this approach, the landslide and sinkhole inventories have been updated and checked, while a statistical approach has been experimented to obtain a pseudo-inventory for the flood geohazard. Starting form the official flood hazard map from the Unit of Management, a number of random points have been extracted from the hazard polygons.

Meanwhile the Variance Inflation Factor (VIF) analysis showed collinearity problems with the predisposing factors related to interferometric and elevation data, mostly related to the Phlegrean Fields bradyseism and to the role of the DTM role as starting data for the geomorphological analysis. In the future this first phase would certainly focus on the update of the geohazard inventories, which are the base of the following phases. A method to clear the interferometric data of the regional contribution from the Phlegrean Fields bradyseism would certainly allow to add a most interesting factor in the analysis as the interferometric data is an accurate and useful tool for geohazard modelling and monitoring.

The second phase of the approach confirmed the good performance of the products obtained with the Ensemble Modeling approach. The analysis also showed how a certain amount of predisposing factors (Planar Curvature, Profile Curvature, Topographic Position Index) had really low importante in the Relative Hazard assessment. Future work may involve

different predisposing factors, a more in-depth study of the ones already proposed in this study, or the application of other machine learning technique on top Random Forests and Maximum Entropy, like the Generalized Linear Model or the Generalized Additive Model.

At last, The RES approach permitted an accurate study of the different Geohazards impact on each other. The interaction matrix has proven to be a powerful tool, allowing the user to obtain a schematic description of the influence of the different geohazards on the, in this case study, system "Multirisk". The interaction matrix showed, thanks to the Causes-Effects diagram, that the Flood & HETD Geohazard was the most influential one. On top of that, it was the only dominant parameter, while the Landslide and Sinkhole Geohazards fell within the subordinate parameter area of the diagram. The produced Multirisk map is, therefore, mainly influenced by the following two factors: (i) the number of Geohazards that coexist in a given area and (ii) the interaction score that characterizes the Geohazards.

In this research project, only three Geohazards were studied. Implementing additional Geohazards would allow the production of a more detailed Multirisk map for the city of Naples. Wildfire Risk, for example, is linked to the initiation of landslides and the integration of this Geohazard as a parameter in the Multirisk system would allow for a more in depth modelization in those areas where both these geohazards exist (for example, the Natural Reserves areas). The RES is a method based on the experience and scientific knowledge of the operator. This represents an advantage as it allows the operator to have total control over the interactivity matrix scores. As these scores are based on a previous in-depth study phase of the available Geohazards, the results will be considered more reliable. Furthermore, since this approach is closely linked to the use of GIS and a user-friendly machine learning algorithm such as Maximum Entropy or Random Forest, adding or modifying the input data for a quick re-evaluation of the Multirisk is a simple and fast operation.

In conclusion, the approach used in this research project showed positive results for the evaluation of the existing interactions between the different Geohazards, allowing the operator to identify the most at-risk areas in a densely populated city like Naples. This product is a valid tool for both scientific and administrative purposes. The Multirisk map can help the administrations to locate the Very High and High Multirisk prone areas, where "cascade" effects could be initiated and lead to disastrous effects. Local administrations can use this tool for risk mitigation planning, but for urban planning too as this tool can help to identify areas where critical conditions already exist and where further urban development would also put the elements already present at risk.

REFERENCES

Aassve, A., Cavalli, N., Mencarini, L., Plach, S., and Sanders, S. (2021). Early assessment of the relationship between the COVID-19 pandemic and births in high-income countries. Proceedings of the National Academy of Sciences, 118(36), e2105709118.

Abu-Mostafa, Y. S., Magdon-Ismail, M., and Lin, H. (2012). Learning from data: a short course. [United States], AMLBook.com.

Aleotti, P., and Chowdhury, R. (1999). Landslide hazard assessment: summary review and new perspectives. Bulletin of Engineering Geology and the environment, 58, 21-44.

Alleva, G. (2018). Struttura e dinamica delle unità amministrative territoriali italiane. Dall'unificazione del Regno al 2017. In Annali di Statistica, pp 5-6. Istituto nazionale di statistica. In Italian.

Allocca, V., Coda, S., Calcaterra, D., and De Vita, P. (2022). Groundwater rebound and flooding in the Naples' periurban area (Italy). Journal of Flood Risk Management, 15(2), e12775.

Allocca, V., Di Napoli, M., Coda, S., Carotenuto, F., Calcaterra, D., Di Martire, D., and De Vita, P. (2021). A novel methodology for Groundwater Flooding Susceptibility assessment through Machine Learning techniques in a mixed-land use aquifer. Science of the total environment, 790, 148067.

Andrejev, K., Krušić, J., Đurić, U., Marjanović, M., and Abolmasov, B. (2017). Relative landslide risk assessment for the city of Valjevo. In Advancing Culture of Living with Landslides: Volume 5 Landslides in Different Environments, 525-533. Springer International Publishing.

Andriani, G. F., and Parise, M. (2017). Applying rock mass classifications to carbonate rocks for engineering purposes with a new approach using the rock engineering system. Journal of Rock Mechanics and Geotechnical Engineering, 9(2), 364-369.

Aprile, F., Sbrana, A., and Toccaceli, R. M. (2004). Il ruolo dei depositi piroclastici nell'analisi cronostratigrafica dei terreni quaternari del sottosuolo della Piana Campana (Italia meridionale). In Italian Alpine and Mediterranean Quaternary, 17(2/2), 547-554.

Ascione, A., Aucelli, P. P., Cinque, A., Di Paola, G., Mattei, G., Ruello, M., Russo Ermolli, E., Santangelo, N., and Valente, E. (2021). Geomorphology of Naples and the Campi Flegrei: human and natural landscapes in a restless land. Journal of Maps, 17(4), 18-28.

Barbet-Massin, M., Jiguet, F., Albert, C. H., and Thuiller, W. (2012). Selecting pseudo-absences for species distribution models: How, where and how many?. Methods in ecology and evolution, 3(2), 327-338.

Barbosa, A.M., Real, R., Munoz, A.R., Brown, J.A. (2013). "New measures for assessing model equilibrium and prediction mismatch in species distribution models." Diversity and Distributions, 19(10), 1333–1338. doi:10.1111/ddi.12100, https://onlinelibrary.wiley.com/doi/full/10.1111/ddi.12100.

Barría, P., Cruzat, M. L., Cienfuegos, R., Gironás, J., Escauriaza, C., Bonilla, C., Moris, R., Ledezma, C., Guerra, M., Rodríguez, R., and Torres, A. (2019). From multi-risk evaluation to resilience planning: The case of central Chilean coastal cities. Water, 11(3), 572.

Bausilio, G., Annibali Corona, M., Di Martire, D., Guerriero, L., Tufano, R., Calcaterra, D., Di Napoli, M., and Francioni, M. (2022). Comparison of two machine learning algorithms for anthropogenic sinkhole susceptibility assessment in the city of Naples (Italy). In Geotechnical Engineering for the Preservation of Monuments and Historic Sites III, 1112-1123. CRC Press.

Beck, B. F. (1986). A generalized genetic framework for the development of sinkholes and karst in Florida, USA. Environmental Geology and Water Sciences, 8(1-2), 5-18.

Beck, B. F. (2004). Soil piping and sinkhole failures ed WB White Encyclopedia of Caves.

Beutel, J., List, S., and von Schweinitz, G. (2019). Does machine learning help us predict banking crises? Journal of Financial Stability, 45, 100693.

Bianchini, S., Confuorto, P., Intrieri, E., Sbarra, P., Di Martire, D., Calcaterra, D., and Fanti, R. (2022). Machine learning for sinkhole risk mapping in Guidonia-Bagni di Tivoli plain (Rome), Italy. Geocarto International, 37(27), 16687-16715.

Biau, G., and Scornet, E. (2016). A random forest guided tour. Test, 25, 197-227.

Bracken, L. J., Cox, N. J., and Shannon, J. (2008). The relationship between rainfall inputs and flood generation in south–east Spain. Hydrological Processes: An International Journal, 22(5), 683-696.

Brandolini, P., Cappadonia, C., Luberti, G. M., Donadio, C., Stamatopoulos, L., Di Maggio, C., Faccini, F., Stanislao, C., Vergari, F., Paliaga, G., Agnesi, V., Alevizos, G., and Del Monte, M. (2020). Geomorphology of the Anthropocene in Mediterranean urban areas. Progress in Physical Geography: Earth and Environment, 44(4), 461-494.

Breiman, L. (2001). Random forests. Machine learning, 45, 5-32.

Burke, B., Slee, A., McIntosh, P. D., Hofmann, H., and Shulmeister, J. (2020). A reactivated cave system induces rapidly developing cover-collapse sinkholes in Tasmania, Australia. Journal of Cave and Karst Studies, 82(1), 31-50.

Bustillo Sánchez, M., Tonini, M., Mapelli, A., and Fiorucci, P. (2021). Spatial assessment of wildfires susceptibility in Santa Cruz (Bolivia) using random forest. Geosciences, 11(5), 224.

Calcaterra, D., and de Luca Tupputi Schinosa, F. (2006). The February 28, 1868 Mt. Echia rockfall in the framework of the historical and present-day landslide activity at Naples, Italy. In Geophysical Research Abstracts, 8, 4708-4708.

Calcaterra, D., Cappelletti, P., Langella, A., Morra, V., Colella, A., and de Gennaro, R. (2000). The building stones of the ancient centre of Naples (Italy): Piperno from Campi Flegrei. A contribution to the knowledge of a long-time-used stone. Journal of Cultural Heritage, 1(4), 415-427.

Calcaterra, D., Coppin, D., De Vita, S., Di Vito, M. A., Orsi, G., Palma, B., and Parise, M. (2007). Slope processes in weathered volcaniclastic deposits within the city of Naples: The Camaldoli Hill case. Geomorphology, 87(3), 132-157.

Calcaterra, D., Langella, A., De Gennaro, R., de' Gennaro, M., and Cappelletti, P. (2005). Piperno from Campi Flegrei: a relevant stone in the historical and monumental heritage of Naples (Italy). Environmental geology, 47, 341-352.

Calderoni, G., and Russo, F. (1998). The geomorphological evolution of the outskirts of Naples during the Holocene: a case study of the Bagnoli-Fuorigrotta depression. The Holocene, 8(5), 581-588.

Caramanna, G., Ciotoli, G., and Nisio, S. (2008). A review of natural sinkhole phenomena in Italian plain areas. Natural hazards, 45(2), 145-172.

Celico, P. B. (1983). Idrogeologia dei massicci carbonatici, delle piane quaternarie e delle aree vulcaniche dell'Italia centro-meridionale: Marche e Lazio meridionali, Abruzzo, Molise e Campania

. Cassa per il Mezzogiorno.

Cello, G., and Mazzoli, S. (1998). Apennine tectonics in southern Italy: a review. Journal of Geodynamics, 27(2), 191-211.

Cennamo, P., Caputo, P., Marzano, C., Miller, A. Z., Sáiz-Jiménez, C., and Moretti, A. (2016). Diversity of phototrophic components in biofilms from Piperno historical stoneworks. Plant Biosystems-An International Journal Dealing with all Aspects of Plant Biology, 150(4), 720-729.

Cinque, A., Ascione, A., and Caiazzo, C. (2000). Distribuzione spazio-temporale e caratterizzazione della fagliazione quaternaria in Appennino meridionale. Le ricerche del GNDT nel campo della pericolosità sismica, 203-218.

Coates, L. (1999). Flood fatalities in Australia, 1788-1996. Australian geographer, 30(3), 391-408.

Coda, S., Tufano, R., Calcaterra, D., Colantuono, P., De Vita, P., Di Napoli, M., Guerriero, L., and Allocca, V. (2023). Groundwater flooding hazard assessment in a semi-urban aquifer through probability modelling of surrogate data. Journal of Hydrology, 621, 129659.

Cole, P. D., and Scarpati, C. (1993). A facies interpretation of the eruption and emplacement mechanisms of the upper part of the Neapolitan Yellow Tuff, Campi Flegrei, southern Italy. Bulletin of Volcanology, 55, 311-326.

Colella, A., Di Benedetto, C., Calcaterra, D., Cappelletti, P., D'Amore, M., Di Martire, D., Graziano, S.F., Papa, L., de Gennaro, M., and Langella, A. (2017). The Neapolitan Yellow Tuff: an outstanding example of heterogeneity. Construction and Building Materials, 136, 361-373.

Colella, C., Gennaro, M. D., and Aiello, R. (2001). Use of zeolitic tuff in the building industry. Reviews in mineralogy and geochemistry, 45(1), 551-587.

Conrad, O., Bechtel, B., Bock, M., Dietrich, H., Fischer, E., Gerlitz, L., Wehberg, J., Wichmann, V., and Boehner, J. (2015). System for Automated Geoscientific Analyses (SAGA) v. 2.1.4. Geosci. Model Dev., 8, 1991-2007, doi:10.5194/gmd-8-1991-2015.

Convertino M., Troccoli A. and Catani F. (2013) - Detecting fingerprints of landslide drivers: a MaxEnt model. Journal of Geophysical Research: Earth Surface, 118(3), 1367-1386.

Corominas, J., van Westen, C., Frattini, P., Cascini, L., Malet, J. P., Fotopoulou, S., Catani, F., Van Den Eeckhaut, M., Mavrouli, O., Agliardi, F., Pitilakis, K., Winter, M. G., Pastor, M., Ferlisi, S., Tofani, V., Hervás, J., and Smith, J. T. (2014). Recommendations for the quantitative analysis of landslide risk. Bulletin of engineering geology and the environment, 73, 209-263.

Costa, A., Di Vito, M. A., Ricciardi, G. P., Smith, V. C., and Talamo, P. (2022). The long and intertwined record of humans and the Campi Flegrei volcano (Italy). Bulletin of Volcanology, 84, 1-27.

Costantini, M., Minati, F., Trillo, F., Ferretti, A., Novali, F., Passera, E., Dehls, J., Larsen, Y., Marinkovic, P., Eineder, M., Brcic, R., Siegmund, R., Kotzerke, P., Probeck, M., Kenyeres, A., Proietti, S., Solari, L., and Andersen, H. S. (2021, July). European ground motion service (EGMS). In 2021 IEEE International Geoscience and Remote Sensing Symposium IGARSS (pp. 3293-3296). IEEE.

Crozier, M. J. (1986). Landslides: causes, consequences, and environment, Croom Helm, London.

Cruden, D. M., and Varnes, D. J. (1996). Landslides: investigation and mitigation. Chapter 3-Landslide types and processes. Transportation research board special report, (247).

Dai, F. C., Lee, C. F., and Ngai, Y. Y. (2002). Landslide risk assessment and management: an overview. Engineering geology, 64(1), 65-87.

De Bruyn, I. A., and Bell, F. G. (2001). The occurrence of sinkholes and subsidence depressions in the Far West Rand and Gauteng Province, South Africa, and their engineering implications. Environmental and Engineering Geoscience, 7(3), 281-295.

De Seta, C. (1999). Napoli. Laterza, Bari-Roma. In Italian.

De Vita, S., Orsi, G., Civetta, L., Carandente, A., D'Antonio, M., Deino, A., di Cesare, T., Di Vito, M. A., Fisher, R. V., Isaia, R., Marotta, E., Necco, A., Ort, M., Pappalardo, L., Piochi, M., and Southon, J. (1999). The Agnano–Monte Spina eruption (4100 years BP) in the restless Campi Flegrei caldera (Italy). Journal of Volcanology and Geothermal Research, 91(2-4), 269-301.

De Vivo, B., Rolandi, G., Gans, P. B., Calvert, A., Bohrson, W. A., Spera, F. J., and Belkin, H. E. (2001). New constraints on the pyroclastic eruptive history of the Campanian volcanic Plain (Italy). Mineralogy and Petrology, 73, 47-65.

DECRETO LEGISLATIVO 23 febbraio 2010, n. 49. https://www.gazzettaufficiale.it/eli/id/2010/04/02/010G0071/sg. In Italian

DECRETO LEGISLATIVO 3 aprile 2006, n. 152. https://www.gazzettaufficiale.it/dettaglio/codici/materiaAmbientale. In Italian

DECRETO MINISTERIALE 25 ottobre 2016. https://www.gazzettaufficiale.it/eli/id/2017/02/02/17A00772/sg. In Italian

Deino, A. L., Orsi, G., de Vita, S., and Piochi, M. (2004). The age of the Neapolitan Yellow Tuff caldera-forming eruption (Campi Flegrei caldera–Italy) assessed by 40Ar/39Ar dating method. Journal of Volcanology and Geothermal Research, 133(1-4), 157-170.

Dewey, J. F., Helman, M. L., Knott, S. D., Turco, E., and Hutton, D. H. W. (1989). Kinematics of the western Mediterranean. Geological Society, London, Special Publications, 45(1), 265-283.

Di Benedetto, C., Cappelletti, P., Favaro, M., Graziano, S. F., Langella, A., Calcaterra, D., and Colella, A. (2015). Porosity as key factor in the durability of two historical building stones: Neapolitan Yellow Tuff and Vicenza Stone. Engineering Geology, 193, 310-319.

Di Martire, D., De Rosa, M., Pesce, V., Santangelo, M. A., and Calcaterra, D. (2012). Landslide hazard and land management in high-density urban areas of Campania region, Italy. Natural Hazards and Earth System Sciences, 12(4), 905-926.

Di Napoli, M., Carotenuto, F., Cevasco, A., Confuorto, P., Di Martire, D., Firpo, M., Pepe, G., Raso, E., and Calcaterra, D. (2020). Machine learning ensemble modelling as a tool to improve landslide susceptibility mapping reliability. Landslides, 17(8), 1897-1914.

Di Vito, M. A., Isaia, R., Orsi, G., Southon, J. D., De Vita, S., D'Antonio, M., Pappalardo, L., and Piochi, M. (1999). Volcanism and deformation since 12,000 years at the Campi Flegrei caldera (Italy). Journal of Volcanology and Geothermal Research, 91(2-4), 221-246.

Doornkamp, J. C. (1989). Hazards. Earth science mapping for planning, development and conservation, 157-173.

Douben, K. J. (2006). Characteristics of river floods and flooding: a global overview, 1985–2003. Irrigation and Drainage: The journal of the International Commission on Irrigation and Drainage, 55(S1), S9-S21.

Dramsch, J. S. (2020). 70 years of machine learning in geoscience in review. Advances in geophysics, 61, 1-55.

Ducci, D., and Sellerino, M. (2015). Groundwater mass balance in urbanized areas estimated by a groundwater flow model based on a 3D hydrostratigraphical model: the case study of the eastern plain of Naples (Italy). Water resources management, 29, 4319-4333.

European Union's Copernicus Land Monitoring Service (2020). Corine Land Cover 2018 (CLC2018), V2020_20u1. https://doi.org/10.2909/71c95a07-e296-44fc-b22b-415f42acfdf0

Evangelista, A., and Viggiani, C. (2013). A paradise inhabited by devils? The geotechnical risks in the city of Napoli and their mitigation, 75-96. Taylor and Francis London.

Faenza, V., (1996, December 13). Voragine inghiotte padre e figlio, Napoli, sprofonda la strada. L'Unità. 12. https://archivio.unita.news/assets/main/1996/12/13/page_027.pdf. In Italian.

Fedele, L., Insinga, D. D., Calvert, A. T., Morra, V., Perrotta, A., and Scarpati, C. (2011). 40 Ar/39 Ar dating of tuff vents in the Campi Flegrei caldera (southern Italy): toward a new chronostratigraphic reconstruction of the Holocene volcanic activity. Bulletin of Volcanology, 73, 1323-1336.

Fell, R., Corominas, J., Bonnard, C., Cascini, L., Leroi, E., and Savage, W. Z. (2008). Guidelines for landslide susceptibility, hazard and risk zoning for land use planning. Engineering geology, 102(3-4), 85-98.

Florida, R., Rodríguez-Pose, A., and Storper, M. (2021). Cities in a post-COVID world. Urban studies.

Folke, C., Carpenter, S. R., Walker, B., Scheffer, M., Chapin, T., and Rockström, J. (2010). Resilience thinking: integrating resilience, adaptability and transformability. Ecology and society, 15(4).

Ford, D. C. (1997). Principal features of evaporite karst in Canada. Carbonates and Evaporites, 12, 15-23.

Fusco, F., Tufano, R., De Vita, P., Di Martire, D., Di Napoli, M., Guerriero, L., Mileti, F.A., Terribile, F., and Calcaterra, D. (2023). A revised landslide inventory of the Campania region (Italy). Scientific data, 10(1), 355.

Galli, M., Ardizzone, F., Cardinali, M., Guzzetti, F., and Reichenbach, P. (2008). Comparing landslide inventory maps. Geomorphology, 94(3-4), 268-289.

Gallina, V., Torresan, S., Critto, A., Sperotto, A., Glade, T., and Marcomini, A. (2016). A review of multi-risk methodologies for natural hazards: Consequences and challenges for a climate change impact assessment. Journal of environmental management, 168, 123-132.

Galve, J. P., Bonachea, J., Remondo, J., Gutiérrez, F., Guerrero, J., Lucha, P., Cendrero, A., Gutiérrez, M., and Sánchez, J. A. (2008). Development and validation of sinkhole susceptibility models in mantled karst settings. A case study from the Ebro valley evaporite karst (NE Spain). Engineering geology, 99(3-4), 185-197.

Gao, Y., and Alexander, E. C. (2008). Sinkhole hazard assessment in Minnesota using a decision tree model. Environmental Geology, 54, 945-956.

Genske, D. D., and Ruff, A. (2006). Expanding cities, shrinking cities, sustainable cities: challenges, opportunities and examples. IAEG2006 Paper, 82(11).

Glade, T. (1998). Establishing the frequency and magnitude of landslide-triggering rainstorm events in New Zealand. Environmental Geology, 35, 160-174.

Glade, T. (2003). Landslide occurrence as a response to land use change: a review of evidence from New Zealand. Catena, 51(3-4), 297-314.

Gongyu, L., and Wanfang, Z. (1999). Sinkholes in karst mining areas in China and some methods of prevention. Engineering Geology, 52(1-2), 45-50.

Grünthal, G., Thieken, A. H., Schwarz, J., Radtke, K. S., Smolka, A., and Merz, B. (2006). Comparative risk assessments for the city of Cologne–storms, floods, earthquakes. Natural Hazards, 38, 21-44.

Guarino, P. M., and Nisio, S. (2012). Anthropogenic sinkholes in the territory of the city of Naples (Southern Italy). Physics and Chemistry of the Earth, Parts A/B/C, 49, 92-102.

Guarino, P. M., Santo, A., Forte, G., De Falco, M., and Niceforo, D. M. A. (2018). Analysis of a database for anthropogenic sinkhole triggering and zonation in the Naples hinterland (Southern Italy). Natural Hazards, 91, 173-192.

Gutiérrez, F., Guerrero, J., and Lucha, P. (2008). A genetic classification of sinkholes illustrated from evaporite paleokarst exposures in Spain. Environmental Geology, 53, 993-1006.

Gutiérrez, F., Parise, M., De Waele, J., and Jourde, H. (2014). A review on natural and human-induced geohazards and impacts in karst. Earth-Science Reviews, 138, 61-88.

Gutiérrez, F. (2016). Sinkhole hazards. In Oxford research encyclopedia of natural hazard science.

Guzzetti, F. (2000). Landslide fatalities and the evaluation of landslide risk in Italy. Engineering Geology, 58(2), 89-107.

Guzzetti, F., Cardinali, M., and Reichenbach, P. (1996). The influence of structural setting and lithology on landslide type and pattern. Environmental and Engineering Geoscience, 2(4), 531-555.

Guzzetti, F., Reichenbach, P., Ardizzone, F., Cardinali, M., and Galli, M. (2006). Estimating the quality of landslide susceptibility models. Geomorphology, 81(1-2), 166-184.

Heap, M. J., Farquharson, J. I., Kushnir, A. R., Lavallée, Y., Baud, P., Gilg, H. A., and Reuschlé, T. (2018). The influence of water on the strength of Neapolitan Yellow Tuff, the most widely used building stone in Naples (Italy). Bulletin of Volcanology, 80, 1-15.

Helbing, D., Ammoser, H., and Kühnert, C. (2006). Disasters as extreme events and the importance of network interactions for disaster response management. Extreme events in nature and society, 319-348.

Hernangómez, D. (2023). Using the tidyverse with terra objects: the tidyterra package. Journal of Open Source Software, 8(91), 5751. ISSN 2475-9066, doi: https://doi.org/10.21105/joss.05751.

Hijmans, R. (2024a). terra: Spatial Data Analysis. R package version 1.7-79, https://rspatial.github.io/terra/, https://rspatial.org/.

Hijmans, R. (2024b). raster: Geographic Data Analysis and Modeling. R package version 3.6-27, https://rspatial.org/raster.

Hodgkins, G. A., Whitfield, P. H., Burn, D. H., Hannaford, J., Renard, B., Stahl, K., Fleig, A. K., Madsen, H., Mediero, L., Korhonen, J., Murphy, C., and Wilson, D. (2017). Climate-driven variability in the occurrence of major floods across North America and Europe. Journal of Hydrology, 552, 704-717.

Hofierka, J., Gallay, M., Bandura, P., and Šašak, J. (2018). Identification of karst sinkholes in a forested karst landscape using airborne laser scanning data and water flow analysis. Geomorphology, 308, 265-277.

Hofmann, G. (1976). Mapping for urban land-use planning in southeast Queensland-a first approach. Bulletin of Engineering Geology and the Environment, 13(1).

Holling, C. S. (1973). Resilience and stability of ecological systems. Annual review of ecology and systematics, 4(1), 1-23.

Huang, R., Huang, J., Ju, N., and Li, Y. (2013). Automated tunnel rock classification using rock engineering systems. Engineering geology, 156, 20-27.

Hudson, J. A. (1992). Rock engineering systems. Theory and practice.

Hungr, O., Leroueil, S., and Picarelli, L. (2014). The Varnes classification of landslide types, an update. Landslides, 11, 167-194.

Iida, T. (2004). Theoretical research on the relationship between return period of rainfall and shallow landslides. Hydrological Processes, 18(4), 739-756.

Ippolito, F., D'Argenio, B., Pescatore, T., and Scandone, P. (1975). Structural-stratigraphic units and tectonic framework of Southern Apennines. Geology of Italy, 2, 317-328.

Isaia, R., Iannuzzi, E., Sbrana, A., Marianelli, P., Donadio, C., Conforti, A., and D'Argenio, B. (2018). Note Illustrative della Carta Geologica d'Italia alla scala 1: 50.000, Foglio 446-447 Napoli (aree emerse). In Italian.

Isaia, R., Marianelli, P., and Sbrana, A. (2009). Caldera unrest prior to intense volcanism in Campi Flegrei (Italy) at 4.0 ka BP: Implications for caldera dynamics and future eruptive scenarios. Geophysical Research Letters, 36(21).

Italian Ministry of the Environment, Land and Sea (2005). DTM20, Digital Terrain Model of the Italian Peninsula with 20 Meters of Resolution. https://www.sir.toscana.it/sit/content/dtm20.

Iverson, R. M. (2000). Landslide triggering by rain infiltration. Water resources research, 36(7), 1897-1910.

James, G., Witten, D., Hastie, T., and Tibshirani, R. (2021). An Introduction to Statistical Learning: With Applications in R (Second Edition). Springer US. https://doi.org/10.1007/978-1-0716-1418-1

Janizadeh, S., Avand, M., Jaafari, A., Phong, T. V., Bayat, M., Ahmadisharaf, E., Prakash, I., Pam, B.T., and Lee, S. (2019). Prediction success of machine learning methods for flash flood susceptibility mapping in the Tafresh watershed, Iran. Sustainability, 11(19), 5426.

Jenks, G. F. (1977). Optimal data classification for choropleth maps. Department of Geographiy, University of Kansas Occasional Paper.

Johnson, K., Depietri, Y., and Breil, M. (2016). Multi-hazard risk assessment of two Hong Kong districts. International Journal of Disaster Risk Reduction, 19, 311-323.

Julià, P. B., and Ferreira, T. M. (2021). From single-to multi-hazard vulnerability and risk in Historic Urban Areas: a literature review. Natural Hazards, 108(1), 93-128.

Kadavi, P. R., Lee, C. W., and Lee, S. (2018). Application of ensemble-based machine learning models to landslide susceptibility mapping. Remote Sensing, 10(8), 1252.

Komendantova, N., Scolobig, A., Garcia-Aristizabal, A., Monfort, D., and Fleming, K. (2016). Multi-risk approach and urban resilience. International Journal of Disaster Resilience in the Built Environment, 7(2), 114-132.

Kononenko, I. (2001). Machine learning for medical diagnosis: history, state of the art and perspective. Artificial Intelligence in medicine, 23(1), 89-109.

Kotu, V., and Deshpande, B. (2015). Chapter 2—Data Mining Process. In V. Kotu and B. Deshpande (Eds.), Predictive Analytics and Data Mining (pp. 17–36). Morgan Kaufmann. https://doi.org/10.1016/B978-0-12-801460-8.00002-1

Krollner, B., Vanstone, B., and Finnie, G. (2010). Financial time series forecasting with machine learning techniques: A survey. In European Symposium on Artificial Neural Networks: Computational Intelligence and Machine Learning, 25-30.

Lacasse, S., Nadim, F., Lacasse, S., and Nadim, F. (2009). Landslide risk assessment and mitigation strategy. Landslides–disaster risk reduction, 31-61.

Langella, A., Cappelletti, P., Mercurio, M., Calcaterra, D., and de Gennaro, M. (2022). Building Stones and Technological Materials of the Campi Flegrei Caldera, Italy. In Campi Flegrei: A Restless Caldera in a Densely Populated Area, 373-393. Berlin, Heidelberg: Springer Berlin Heidelberg.

Lee, S. A. R. O. (2005). Application of logistic regression model and its validation for landslide susceptibility mapping using GIS and remote sensing data. International Journal of remote sensing, 26(7), 1477-1491.

Lee, S., Kim, J. C., Jung, H. S., Lee, M. J., and Lee, S. (2017). Spatial prediction of flood susceptibility using random-forest and boosted-tree models in Seoul metropolitan city, Korea. Geomatics, Natural Hazards and Risk, 8(2), 1185-1203.

Liu, J. G., Mason, P. J., Clerici, N., Chen, S., Davis, A., Miao, F., Deng, H., and Liang, L. (2004). Landslide hazard assessment in the Three Gorges area of the Yangtze river using ASTER imagery: Zigui–Badong. Geomorphology, 61(1-2), 171-187.

Liu, Z., Nadim, F., Garcia-Aristizabal, A., Mignan, A., Fleming, K., and Luna, B. Q. (2015). A three-level framework for multi-risk assessment. Georisk: Assessment and management of risk for engineered systems and geohazards, 9(2), 59-74.

Lombardo, M. (2003). Colonie di colonie: le fondazioni sub-coloniali greche tra colonizzazione e colonialismo. In Italian.

Luino, F. (2016). Floods. Encyclopedia of engineering geology. Encyclopedia of earth sciences series. Springer, Cham. https://doi. org/10.1007/978-3-319-12127-7.

Marks, D., Kimball, J., Tingey, D., and Link, T. (1998). The sensitivity of snowmelt processes to climate conditions and forest cover during rain-on-snow: A case study of the 1996 Pacific Northwest flood. Hydrological Processes, 12(10-11), 1569-1587.

Martins, P. (2019). Internal Erosion in Volcanic Soils—Challenges for Infrastructure Projects in New Zealand. In IAEG/AEG Annual Meeting Proceedings, San Francisco, California, 2018-Volume 5: Geologic Hazards: Earthquakes, Land Subsidence, Coastal Hazards, and Emergency Response, 137-141. Springer International Publishing.

Marzocchi, W., Garcia-Aristizabal, A., Gasparini, P., Mastellone, M. L., and Di Ruocco, A. (2012). Basic principles of multi-risk assessment: a case study in Italy. Natural hazards, 62, 551-573.

Mascheri, G., Chieffo, N., Arrighi, C., Del Gaudio, C., and Lourenço, P. B. (2024). A framework for multi-risk assessment in a historical area of Lisbon. International Journal of Disaster Risk Reduction, 108, 104508.

Mastrantoni, G., Masciulli, C., Marini, R., Esposito, C., Scarascia Mugnozza, G., and Mazzanti, P. (2023). A novel model for multi-risk ranking of buildings at city level based on open data: the test site of Rome, Italy. Geomatics, Natural Hazards and Risk, 14(1), 2275541.

Mazzeo, G. (2009). Naples. Cities, 26(6), 363-376.

Mazzoccola, D. F. (1992). A comprehensive method of rock mass characterization for indicating slope instability, MoS Thesis, Department of Mineral Resources Engineering - Royal School of Mines. London, Imperial College of Science, Technology and Medicine.

McAdoo, B. G., Quak, M., Gnyawali, K. R., Adhikari, B. R., Devkota, S., Rajbhandari, P. L., and Sudmeier-Rieux, K. (2018). Roads and landslides in Nepal: how development affects environmental risk. Natural Hazards and Earth System Sciences, 18(12), 3203-3210.

McCall, G. J. (2012). Geohazards: natural and man-made. Springer Science and Business Media.

McCall, G. J. H. (1998). Geohazards and the urban environment. Geological Society, London, Engineering Geology Special Publications, 15(1), 309-318.

Meerow, S., Newell, J. P., and Stults, M. (2016). Defining urban resilience: A review. Landscape and urban planning, 147, 38-49.

Merlini, S., and Mostardini, F. (1986). Appennino centro-meridionale: Sesioni geologiche e proposta di modello strutturale. In Geologia dell'Italia centrale. Congresso nazionale, 73, 147-149.

Merow, C., Smith, M. J., and Silander Jr, J. A. (2013). A practical guide to MaxEnt for modeling species' distributions: what it does, and why inputs and settings matter. Ecography, 36(10), 1058-1069.

Meten, M., PrakashBhandary, N., and Yatabe, R. (2015). Effect of landslide factor combinations on the prediction accuracy of landslide susceptibility maps in the Blue Nile Gorge of Central Ethiopia. Geoenvironmental Disasters, 2, 1-17.

Michie, D., Spiegelhalter, D. J., and Taylor, C. C. (1994). Machine learning, neural and statistical classification.

Mitchell, T.M. (1997) Machine Learning. McGraw-Hill, Inc., New York.

Modarres, R., Sarhadi, A., and Burn, D. H. (2016). Changes of extreme drought and flood events in Iran. Global and Planetary Change, 144, 67-81.

Morra, V., Calcaterra, D., Cappelletti, P., Colella, A., Fedele, L., de' Gennaro, R., Langella, A., Mercurio, M., de' Gennaro, M. 2010. Urban geology: relationships between geological setting and architectural heritage of the Neapolitan area. In: (Eds.) Marco Beltrando, Angelo Peccerillo, Massimo Mattei, Sandro Conticelli, and Carlo Doglioni, Journal of the Virtual Explorer, volume 36, paper 26, doi: 10.3809/jvirtex.2010.00261

Mouici, R., Baali, F., Hadji, R., Boubaya, D., Audra, P., Fehdi, C. É., Cailhol, D., Jaillet, S., and Arfib, B. (2017). Geophysical, geotechnical, and speleologic assessment for karst-sinkhole collapse genesis in Cheria plateau (NE Algeria). Mining Science, 24, 59-71.

Muzirafuti, A., Boualoul, M., Barreca, G., Allaoui, A., Bouikbane, H., Lanza, S., Crupi, A., and Randazzo, G. (2020). Fusion of remote sensing and applied geophysics for sinkholes identification in Tabular Middle Atlas of Morocco (the Causse of El Hajeb): Impact on the protection of water resource. Resources, 9(4), 51.

Naimi, B., Hamm, Na, Groen, T.A., Skidmore, A.K., and Toxopeus, A.G. (2014). Where is positional uncertainty a problem for species distribution modelling. Ecography, 37, 191-203. doi:10.1111/j.1600-0587.2013.00205.x.

Newendorp, P. D. (1976). Decision analysis for petroleum exploration.

Nisio, S., Caramanna, G., and Ciotoli, G. (2007). Sinkholes in Italy: first results on the inventory and analysis. Geological Society, London, Special Publications, 279(1), 23-45.

Orsi, G., Civetta, L., D'Antonio, M., Di Girolamo, P., and Piochi, M. (1995). Step-filling and development of a three-layer magma chamber: the Neapolitan Yellow Tuff case history. Journal of Volcanology and Geothermal Research, 67(4), 291-312.

Orsi, G., D'Antonio, M., de Vita, S., and Gallo, G. (1992). The Neapolitan Yellow Tuff, a large-magnitude trachytic phreatoplinian eruption: eruptive dynamics, magma withdrawal and caldera collapse. Journal of Volcanology and Geothermal Research, 53(1-4), 275-287.

Pachauri, A. K., and Pant, M. (1992). Landslide hazard mapping based on geological attributes. Engineering geology, 32(1-2), 81-100.

Pacione, M. (1987). Socio-spatial development of the South Italian City: The case of Naples. Transactions of the Institute of British Geographers, 433-450.

Parajka, J., Kohnová, S., Bálint, G., Barbuc, M., Borga, M., Claps, P., Cheval, S., Dumitrscu, A., Gaume, E., Hlavčová, K., Merz, R., Pfaundler, M., Stancalie, G., Szolgay, J, and Blöschl, G. (2010). Seasonal characteristics of flood regimes across the Alpine–Carpathian range. Journal of hydrology, 394(1-2), 78-89.

Parise, M. (2001). Landslide mapping techniques and their use in the assessment of the landslide hazard. Physics and Chemistry of the Earth, Part C: Solar, Terrestrial and Planetary Science, 26(9), 697-703.

Parise, M. (2015). A procedure for evaluating the susceptibility to natural and anthropogenic sinkholes. Georisk: Assessment and Management of Risk for Engineered Systems and Geohazards, 9(4), 272-285.

Parise, M., Calcaterra, D., Schinosa, F. D. L. T., and Palma, B. (2004). Rockfall distribution and magnitude at the western slope of the Camaldoli Hill (Naples, Italy). In Proc. 9th intern. symp. on Landslides, Rio de Janeiro, June 28/July (Vol. 2, p. 2004).

Parise, M., Pisano, L., and Vennari, C. (2018). Sinkhole clusters after heavy rainstorms. Journal of Cave and Karst Studies, 80(1), 28-38.

Parker, W. S. (2013). Ensemble modeling, uncertainty and robust predictions. Wiley interdisciplinary reviews: Climate change, 4(3), 213-223.

Pebesma, E. (2018). Simple Features for R: Standardized Support for Spatial Vector Data. The R Journal, 10(1), 439–446. doi: https://doi.org/10.32614/RJ-2018-009.

Pebesma, E., and Bivand, R. (2023). Spatial Data Science: With applications in R. Chapman and Hall/CRC. doi:10.1201/9780429459016, https://r-spatial.org/book/.

Perrotta, A., Scarpati, C., Luongo, G., and Morra, V. (2006). The Campi Flegrei caldera boundary in the city of Naples. In Developments in volcanology, 9, 85-96. Elsevier.

Pescaroli, G., and Alexander, D. (2015). A definition of cascading disasters and cascading effects: Going beyond the “toppling dominos” metaphor. Planet@ risk, 3(1), 58-67.

Petley, D. (2012). Global patterns of loss of life from landslides. Geology, 40(10), 927-930.

Phillips, S. J., and Dudík, M. (2008). Modeling of species distributions with Maxent: new extensions and a comprehensive evaluation. Ecography, 31(2), 161-175.

Phillips, S. J., Anderson, R. P., and Schapire, R. E. (2006). Maximum entropy modeling of species geographic distributions. Ecological modelling, 190(3-4), 231-259.

Phillips, S. J., Dudík, M., and Schapire, R. E. (2004). A maximum entropy approach to species distribution modeling. In Proceedings of the twenty-first international conference on Machine learning, 83.

Phillips, S. J., Dudík, M., and Schapire, R. E. (2023). [Internet] Maxent software for modeling species niches and distributions (Version 3.4.1). Available from url: http://biodiversityinformatics.amnh.org/open_source/maxent/. Accessed on 2023-5-15.

Pollock, W., and Wartman, J. (2020). Human vulnerability to landslides. GeoHealth, 4(10), e2020GH000287.

Posit Team (2024). RStudio: Integrated Development Environment for R. Posit Software, PBC, Boston, MA. URL http://www.posit.co/.

Prasad, P., Loveson, V. J., Das, B., and Kotha, M. (2022). Novel ensemble machine learning models in flood susceptibility mapping. Geocarto International, 37(16), 4571-4593.

Probst, P., Wright, M. N., and Boulesteix, A. L. (2019). Hyperparameters and tuning strategies for random forest. Wiley Interdisciplinary Reviews: data mining and knowledge discovery, 9(3), e1301.

QGIS Development Team (2024). QGIS Geographic Information System. Open Source Geospatial Foundation. URL http://qgis.org

R Core Team (2023). R: A Language and Environment for Statistical Computing. R Foundation for Statistical Computing, Vienna, Austria. <https://www.R-project.org/>.

Rajula, H. S. R., Verlato, G., Manchia, M., Antonucci, N., and Fanos, V. (2020). Comparison of conventional statistical methods with machine learning in medicine: diagnosis, drug development, and treatment. Medicina, 56(9), 455.

Ramesh, S., Hebbar, R., Niveditha, M., Pooja, R., Shashank, N., and Vinod, P. V. (2018). Plant disease detection using machine learning. In 2018 International conference on design innovations for 3Cs compute communicate control (ICDI3C), 41-45. IEEE.

Rapalo, M. C. (2018). In San Carlo all'Arena district: positive and negative values in a degraded cultural landscape. In La Baia di Napoli. Strategie integrate per la conservazione e la fruizione del paesaggio culturale. In Italian.

Recknagel, F. (2001). Applications of machine learning to ecological modelling. Ecological modelling, 146(1-3), 303-310.

Reddy, R. K. T., and Bonham-Carter, G. F. (1991). A decision-tree approach to mineral potential mapping in Snow Lake area, Manitoba. Canadian Journal of Remote Sensing, 17(2), 191-200.

Reichenbach, P., Busca, C., Mondini, A. C., and Rossi, M. (2014). The influence of land use change on landslide susceptibility zonation: the Briga catchment test site (Messina, Italy). Environmental management, 54, 1372-1384.

Reichenbach, P., Cardinali, M., De Vita, P., and Guzzetti, F. (1998). Regional hydrological thresholds for landslides and floods in the Tiber River Basin (central Italy). Environmental Geology, 35(2-3), 146-159.

Rimal, B., Zhang, L., Keshtkar, H., Sun, X., and Rijal, S. (2018). Quantifying the spatiotemporal pattern of urban expansion and hazard and risk area identification in the Kaski District of Nepal. Land, 7(1), 37.

Rispoli, C., Di Martire, D., Calcaterra, D., Cappelletti, P., Graziano, S. F., and Guerriero, L. (2020). Sinkholes threatening places of worship in the historic center of Naples. Journal of Cultural Heritage, 46, 313-319.

Rolandi, G., Bellucci, F., Heizler, M. T., Belkin, H. E., and De Vivo, B. (2003). Tectonic controls on the genesis of ignimbrites from the Campanian Volcanic Zone, southern Italy. Mineralogy and Petrology, 79, 3-31.

Rosenbaum, M. S., and Culshaw, M. G. (2003). Communicating the risks arising from geohazards. Journal of the Royal Statistical Society Series A: Statistics in Society, 166(2), 261-270.

Rosi, M., Sbrana, A., and Principe, C. (1983). The Phlegraean Fields: structural evolution, volcanic history and eruptive mechanisms. Journal of Volcanology and Geothermal Research, 17(1-4), 273-288.

Rozos, D., Bathrellos, G. D., and Skillodimou, H. D. (2011). Comparison of the implementation of rock engineering system and analytic hierarchy process methods, upon landslide susceptibility mapping, using GIS: a case study from the eastern Achaia County of Peloponnesus, Greece. Environmental Earth Sciences, 63, 49-63.

Russo, F., Calderoni, G., and Lombardo, M. (1998). Evoluzione geomorfologica della depressione Bagnoli-Fuorigrotta: periferia urbana della città di Napoli. Bollettino della Società geologica italiana, 117, 21-38. In Italian

Salvadori, G., De Michele, C., and Durante, F. (2011). On the return period and design in a multivariate framework. Hydrology and Earth System Sciences, 15(11), 3293-3305.

Sangati, M., and Borga, M. (2009). Influence of rainfall spatial resolution on flash flood modelling. Natural Hazards and Earth System Sciences, 9(2), 575-584.

Santangelo, N., Ciampo, G., Di Donato, V., Esposito, P., Petrosino, P., Romano, P., Russo Ermolli, E., Santo, A., Toscano, F., and Villa, I. (2010). Late Quaternary buried lagoons in the northern Campania plain (southern Italy): evolution of a coastal system under the influence of volcano-tectonics and eustatism. Italian journal of geosciences, 129(1), 156-175.

Santangelo, N., Romano, P., Ascione, A., and Ermolli, E. R. (2017). Quaternary evolution of the Southern Apennines coastal plains: A review. Geologica Carpathica, 68(1), 43.

Sbrana, A., Marianelli, P., and Pasquini, G. (2021). The phlegrean fields volcanological evolution. Journal of Maps, 17(2), 557-570.

Scarpati, C., Cole, P., and Perrotta, A. (1993). The Neapolitan Yellow Tuff—a large volume multiphase eruption from Campi Flegrei, southern Italy. Bulletin of Volcanology, 55, 343-356.

Scarpati, C., Perrotta, A., and Sparice, D. (2015). Volcanism in the city of Naples. Rendiconti Online Società Geologica Italiana, 33.

Scarpati, C., Perrotta, A., Lepore, S., and Calvert, A. (2013). Eruptive history of Neapolitan volcanoes: constraints from 40Ar–39Ar dating. Geological Magazine, 150(3), 412-425.

Schaffner, F.J. (Director). (1968). Planet of the Apes [film]. APJAC Productions, Twentieth Century Fox.

Schuster, R. L. (1996). Socioeconomic significance of landslides. Landslides: Investigation and mitigation, 247, 12-35.

Schuster, R. L., and Highland, L. M. (2001). Socioeconomic and environmental impacts of landslides in the western hemisphere (No. 2001-276).

Scott, A. J., and Storper, M. (2015). The nature of cities: The scope and limits of urban theory. International journal of urban and regional research, 39(1), 1-15.

Scotto di Santolo, A., Bausilio, G., Danzi, M., Del Vecchio, U., Di Martire, D., Infante, D., and Ramondini, M. (2022). Monitoring and 3D surveys for the safety fruition of a hypogeum site. In Geotechnical Engineering for the Preservation of Monuments and Historic Sites III, 655-666. CRC Press.

Scotto di Santolo, A., Evangelista, L., Silvestri, F., Cavuoto, G., Di Fiore, V., Punzo, M., Tarallo, D., and Evangelista, A. (2015). Investigations on the stability conditions of a tuff cavity: the Cimitero delle Fontanelle in Naples. Rivista Italiana di Geotecnica XLIX (3), 28-46.

Selva, J. (2013). Long-term multi-risk assessment: statistical treatment of interaction among risks. Natural hazards, 67, 701-722.

Sepe, C., Calcaterra, D., Di Martire, D., Fusco, F., Tufano, R., Vitale, E., and Guerriero, L. (2023). Triggering conditions and propagation of the December 2019 Palma Campania landslide: Implications for residual hazard estimation at recurrent landslide sites. Engineering Geology, 322, 107177.

Servizio Geologico d'Italia (2015). Carta Geologica d'Italia alla scala 1:50,000. F. 446-447 "Napoli". ISPRA, Roma. https://www.isprambiente.gov.it/Media/carg/447_NAPOLI/Foglio.html

Seutter, M. (between 1730 and 1760). Map of the City of Naples. Bernard Pavel Moll's Collection, Moravian Museum. https://mapy.mzk.cz/mzk03/001/063/107/2619269140/

Shirmard, H., Farahbakhsh, E., Müller, R. D., and Chandra, R. (2022). A review of machine learning in processing remote sensing data for mineral exploration. Remote Sensing of Environment, 268, 112750.

Sidle, R. C., Ziegler, A. D., Negishi, J. N., Nik, A. R., Siew, R., and Turkelboom, F. (2006). Erosion processes in steep terrain—Truths, myths, and uncertainties related to forest management in Southeast Asia. Forest ecology and management, 224(1-2), 199-225.

Silva, O. L., Bezerra, F. H., Maia, R. P., and Cazarin, C. L. (2017). Karst landforms revealed at various scales using LiDAR and UAV in semi-arid Brazil: Consideration on karstification processes and methodological constraints. Geomorphology, 295, 611-630.

Swets J.A. (1988) - Measuring the accuracy of diagnostic systems. Science, 240(4857), 1285-1293.

Taalab, K., Cheng, T., and Zhang, Y. (2018). Mapping landslide susceptibility and types using Random Forest. Big Earth Data, 2(2), 159-178.

Taheri, K., Gutiérrez, F., Mohseni, H., Raeisi, E., and Taheri, M. (2015). Sinkhole susceptibility mapping using the analytical hierarchy process (AHP) and magnitude–frequency relationships: A case study in Hamadan province, Iran. Geomorphology, 234, 64-79.

Tavoularis, N., Papathanassiou, G., Ganas, A., and Argyrakis, P. (2021). Development of the landslide susceptibility map of Attica region, Greece, based on the method of rock engineering system. Land, 10(2), 148.

Terzaghi, K. (1950). Mechanism of landslides.

Thuiller, W., Georges, D., Gueguen, M., Engler, R., Breiner, F., Lafourcade, B., Patin, R., and Blancheteau, H. (2024). biomod2: Ensemble Platform for Species Distribution Modeling. R package version 4.2-5-2, https://biomodhub.github.io/biomod2/.

Tufano, R., Guerriero, L., Annibali Corona, M., Bausilio, G., Di Martire, D., Nisio, S., and Calcaterra, D. (2022). Anthropogenic sinkholes of the city of Naples, Italy: An update. Natural Hazards, 112(3), 2577-2608.

Turner, A. K., and Schuster, R. L. (1996). Socioeconomic significance of landslides. Landslides: Investigation and Mitigation. Special Report, National Research Council US. Transportation Research Board, 247.

Twidale, C. R. (1987). Sinkholes (Dolines) in lateritised sediments, western sturt plateau, northern territory, Austrália. Geomorphology, 1(1), 33-52.

Varnes, D. J. (1958). Landslide types and processes. Landslides and engineering practice, 24, 20-47.

Varnes, D. J. (1978). Slope movement types and processes. Special report, 176, 11-33.

Varnes, D.J., and IAEG Commission on Landslides (1984). Landslide hazard zonation: a review of principles and practice. UNESCO, Paris, 63.

Vitale, S., and Ciarcia, S. (2013). Tectono-stratigraphic and kinematic evolution of the southern Apennines/Calabria–Peloritani Terrane system (Italy). Tectonophysics, 583, 164-182.

Vitale, S., and Ciarcia, S. (2018). Tectono-stratigraphic setting of the Campania region (southern Italy). Journal of Maps, 14(2), 9-21.

Waltham, A. C., and Fookes, P. G. (2003). Engineering classification of karst ground conditions. Quarterly Journal of Engineering Geology and Hydrogeology, 36(2), 101-118.

Waltham, T., Bell, F. G., Culshaw, M. G., Knez, M., and Slabe, T. (2005). Sinkholes and subsidence: karst and cavernous rocks in engineering and construction (Vol. 382). Berlin: Springer.

Wei, L., Hu, K. H., and Hu, X. D. (2018). Rainfall occurrence and its relation to flood damage in China from 2000 to 2015. Journal of Mountain Science, 15(11), 2492-2504.

Wickham, H. (2016). ggplot2: Elegant Graphics for Data Analysis. Springer-Verlag New York. ISBN 978-3-319-24277-4, https://ggplot2.tidyverse.org.

Wieczorek, G. F. (1996). Landslides: investigation and mitigation. Chapter 4-Landslide triggering mechanisms. Transportation Research Board Special Report, (247).

Wilke, C., Wiernik, B. (2022). ggtext: Improved Text Rendering Support for 'ggplot2'. R package version 0.1.2, <https://CRAN.R-project.org/package=ggtext>.

Williams, P. (2003). Dolines. In Gunn, J. (Ed.), Encyclopedia of caves and karst science, 628-642. Taylor and Francis.

Wohletz, K., Civetta, L., and Orsi, G. (1999). Thermal evolution of the Phlegraean magmatic system. Journal of Volcanology and Geothermal Research, 91(2-4), 381-414.

Wohletz, K., Orsi, G., and De Vita, S. (1995). Eruptive mechanisms of the Neapolitan Yellow Tuff interpreted from stratigraphic, chemical, and granulometric data. Journal of Volcanology and Geothermal Research, 67(4), 263-290.

WP/WLI (International Geotechnical Societies' UNESCO Working Party on World Landslide Inventory). (1993). Multilingual landslide glossary.

Yang, D., Zhao, Y., Armstrong, R., and Robinson, D. (2009). Yukon River streamflow response to seasonal snow cover changes. Hydrological Processes: an International Journal, 23(1), 109-121.

Yao, X., Tham, L. G., and Dai, F. C. (2008). Landslide susceptibility mapping based on support vector machine: a case study on natural slopes of Hong Kong, China. Geomorphology, 101(4), 572-582.

Zhou, G., Yan, H., Chen, K., and Zhang, R. (2016). Spatial analysis for susceptibility of second-time karst sinkholes: A case study of Jili Village in Guangxi, China. Computers and Geosciences, 89, 144-160.

ACKNOWLEDGMENTS

I know I am not good at a lot of things, and expressing my emotions is one of them. These thanks will most likely be short, maybe even a little cold. Please remember that, like everyone else, I'm trying my best.

First of all, I would like to thank my supervisor, Professor Domenico Calcaterra, for helping me grow as a person through his teachings. His professionalism and objective remarks have helped me more than he may ever know. I am also grateful to Professor Diego Di Martire, from whom I have learned, and am still learning, a great deal. I am truly thankful for the opportunity to meet him and be his student. I also want to extend my thanks to the Coordinator of the PhD program, Professor Rosa Di Maio, for her kindness and guidance throughout this journey. Additionally, I am grateful to Professor Luigi Guerriero, Dr. Rita Tufano, and everyone else at the Department. I would also like to thank the Referees for their insightful suggestions.

Thank you, whoever you are. I don't know why you may want to read these lines, but the last of these formal thanks are to you, wherever and whenever you are.

Now, for the more "casual" thanks:

A heartfelt thank you to all of my friends. I'm not always good at staying in touch or keeping close to those who are most dear to me, but you have all stayed by my side, and that means a lot. These years have not been easy on me—or on anyone, to be fair—but I was happy to know that there was always someone I could talk to. I guess we'll have to change the name of the group chat now!

Lastly, and most importantly, I want to thank my family. They are the only reason I am able to be here, writing these acknowledgments. I have never said it aloud, probably never will, and someday I'll maybe regret it, but I do love you all.